

Absolute Quantification in Small Plant Radiotracer Studies

by

Laurie C. Cumberbatch

Graduate Program in Medical Physics
Duke University

Date: _____

Approved:

Calvin Howell, Supervisor

Timothy Turkington, Chair

James Bowsher

Robert Reiman

Chantal D. Reid

Dissertation submitted in partial fulfillment of
the requirements for the degree of Doctor
of Philosophy in the
Graduate Program in Medical Physics
of Duke University

2017

ABSTRACT

Absolute Quantification in Small Plant Radiotracer Studies

by

Laurie C. Cumberbatch

Graduate Program in Medical Physics
Duke University

Date: _____

Approved:

Calvin Howell, Supervisor

Tim Turkington, Chair

James Bowsher

Robert Reiman

Chantal Reid

An abstract of a dissertation submitted in partial
fulfillment of the requirements for the degree
of Doctor of Philosophy in the
Graduate Program in Medical Physics
of Duke University

2017

Copyright by
Laurie C. Cumberbatch
2017

Abstract

The main objective of this dissertation research is to develop measurement and data-analysis tools for improving the quantitative accuracy of radiotracer studies of small plants, e.g., grasses in their early growth stages and tree seedlings. Improved accuracy is needed due to the thin nature of plant organs, e.g., leaves and stem. In addition, the methods developed in this thesis are applied to study the plant-environment interface of barley. Some of the approaches explored have potential to increase the statistical accuracy of counting data using PET imaging techniques. Improving the statistical precision of radionuclide tracking data will add to the analysis options. Another important goal is to measure the absolute photosynthetic rate. The standard approach in plant radiotracer experiments is to perform measurements of the relative distribution of radioactivity in various parts of the plant being studied. A limitation of this approach is that it does not take into account differences in the amount of radioisotope assimilated that are available for transport and allocation to the various sinks, that is, absolute CO₂ uptake and photosynthetic rates are important factors in understanding the holistic physiological responses of plants to external conditions. For example, monitoring the movement of carbon-11 (¹¹C) tagged carbohydrates in a plant requires an estimate of the average photosynthetic rate to determine the actual quantity of carbohydrates in each plant region (e.g. leaf, shoot, and root).

Radiotracing provides a method for real-time measurements of substance absorption, allocation and metabolic consumption and production in living organisms. Application of radioactive labelling in plants enables measurements associated with core physiological processes, e.g., photosynthesis, water uptake and nitrogen absorption and

utilization. Plant uptake of radiotracers allows for tracking spatial and temporal distribution of substances, which enables studies of the plant-environment interface and the mechanisms involved in the allocation of resources (e.g., sugars, nutrients, and water). As such, these techniques are increasingly becoming an important tool for investigating the processes involved in the physiological responses of plants to changes in their local environmental conditions.

This dissertation has two major components: (1) development of experiment techniques for absolute photosynthetic rate measurements in plants using radio-isotope labeling, and (2) application of radioisotope tracing techniques to study the plant-environment interface in barley. The first component is covered in chapters one through three. The second component is presented in chapter four. An introduction into radio-tracing techniques is provided in chapter one. Chapter two describes radio-isotope production, radio-labelled compound preparation and delivery of labels to plant measurements. Chapter three outlines methods that can be employed to measure the absolute photosynthetic rate ($\mu\text{mol}/\text{m}^2/\text{s}$) for a closed-loop system with $[\text{CO}_2]$ monitoring capabilities. Chapter four describes the background and results of our study on changing environmental conditions on a model system, barley seedlings. Chapter 5 will introduce the use of Monte-Carlo modeling for scaling the collected data to adjust the detected coincidence counts for losses due to positron escape from plant tissue. Chapter 6 describes the development of a novel imaging technique using direct positron detection that takes advantage of the high fraction of positrons escaping thin plant tissue.

In this dissertation, we have performed the most extensive measurements of carbohydrate allocation and translocation in a plant species using radio-isotope tracing

techniques. A major practical limitation of studies based on radio-isotope labeling is the number of samples that can be measured in a single project. Our study on barley (*Hordeum distichum*) includes measurements on more than 30 plants. The short-lived radionuclide, ^{11}C , was used to determine the real-time response to metabolite transport in barley. Sugars are photosynthesized and tagged with a positron-emitting radioisotope by flowing carbon dioxide ($^{11}\text{CO}_2$) tagged air over an active leaf. Data analysis of measurements taken in this dissertation indicates that the fraction of carbohydrates allocated to below ground sinks decreased, by $31\% \pm 9\%$ in ambient $[\text{CO}_2]$ and by $37\% \pm 14\%$ in elevated $[\text{CO}_2]$, when the nutrient solution was rapidly changed from the high to the low nutrient condition.

Acknowledgments

I dedicate this section of my dissertation to those many individuals that have invested their valuable time into my growth and development. At my current stage in life, I truly recognize that time is the most valuable resource. It is truly remarkable how much of my journey in becoming a scientist depended on so many people. So it is with complete humility and a humbled spirit that I write these following words.

I would like to first acknowledge the radiotracer research group here at the TUNL facility on Duke University campus. It has been a special honor working with my advisor, Dr. Calvin Howell. His brilliance and dedication to research continues to be a guide on what a true mentor and scientist should resemble. He was always willing to sacrifice his time and provide critical guidance at times most needed. For this and many more reasons, I want to say that I truly thank Dr. Howell and will miss witnessing his enthusiasm and persistence in research on a daily basis. Next, I would like to thank Dr. Chantal Reid, our main collaborator from the Biology Department. Dr. Reid has shown kindness and patience over the years as I began to learn about basic behaviors of plant seedlings and their delicate infrastructure. Her expertise in this area was without question the catalyst to our success in all our research endeavors. I always left our conversations feeling better about myself and my growth in knowledge regarding plant physiology concepts. Lastly, I would like to thank Dr. Alexander Crowell. I was very fortunate to have the opportunity to be Dr. Crowell's office mate, where he has mentored me in many areas of experimental nuclear physics including data acquisition, equipment troubleshooting, and code debugging. Dr. Crowell became a dear friend and someone I admire greatly.

The research conducted in this dissertation would not have been possible without the efforts of the TUNL technical and scientific staff. They were always willing to help when called upon. I want to especially give thanks to Chris Westerfeldt for his role in equipment and material purchases and willingness to instruct on the use of various equipment in the lab. Thanks are also in order for the reliable help of John Dunham. His expertise in the area of hydraulics, plumbing, and machinery was invaluable to my research. I am also extremely grateful to Bret Carlin and his aid in software setup and electronic configuration during development of our radiotracer gas delivery system and associated hardware. I also enjoyed our many talks on new gadgets and apps available in the marketplace. Thanks to Richard O'Quinn for his tireless help with the radioactive gas-target system on the Time-of-Flight (TOF) beam line. Without his help, the project may not have developed as quickly as it did. I would also like to thank the staff at the TUNL administrative office for their help with payroll, timely paperwork submission, and parking pass connections.

I would be remiss if I didn't mention the biggest supporters in my life. My family has always showed their support and encouragement at the most critical stages of my life. My mother, Elva, was a great woman and had a heart for helping others. My mother sacrificed to send me to private tutoring despite being a single mother of three children. It was in tutoring that I developed a love for mathematics, which enabled me to pass the entrance exam into Brooklyn Technical H.S. She passed away a month before my first class at Brooklyn Tech, but her desire for me to excel was etched into my memory. I also want to thank my Dad, Selwyn, who passed away over two years ago. He was always a big advocate for education and challenged me to dream bigger and aim for higher

accomplishments. He instilled in me a strong work ethic and throughout my childhood helped me develop a critical thinking skillset. Many thanks as well to my brother, Colin who was one of my first role models by set the bar high through his pursuits in chemical engineering. My sisters, Martha, Lafern, and Petrona, were always supportive and enthusiastic about my career goals.

And lastly, I extend my greatest thanks to my wonderful wife, Selena, who has been my strongest supporter and encouraged me at my weakest moments in graduate school and during personal crises. She has been very patient and supportive throughout the last stages of my graduate career as well, despite the long hours spent in the research facility on occasion.

This work was supported in part by the U.S. National Science Foundation (NSF), Division of Biological Infrastructure under grant number DBI-0649924, the U.S. NSF under grant number IBN-9985877, the U.S. Department of Energy (DOE), Biological and Environmental Research under grant number DE-SC0005057, and the U.S. DOE, Office of Nuclear Physics under grant number DE-FG02-97ER41033 and contract number DE-AC05-06OR23177.

Contents

Abstract	iv
Acknowledgements	vii
List of Tables	xiii
List of Figures.....	xv
Chapter 1: Introduction	1
1.1 Background	2
1.2 Fundamentals of Radiotracer Experiments	3
1.3 Motivation	5
1.3.1 Absolute Activity from Coincidence Counting	5
1.3.2 Improving Counting Statistics	6
Chapter 2: Radiotracer Production and Gamma Detection	8
2.1 Radioisotope Production.....	9
2.2 Radiotracer Transport System	10
2.3 Gamma Detection.....	12
2.3.1 Coincidence Counting	12
Chapter 3: Measuring Photosynthesis Rate.....	14
3.1 Total Sugar Production in the Leaf.....	15
3.1.1 Estimate of Photosynthesis by CO ₂ Depletion in Closed-loop System.....	17
3.1.2 Estimate of Photosynthesis by CO ₂ Depletion in Closed-loop System while Compensating for Leaf CO ₂ Uptake	19
3.1.3 ¹¹ C Pulse Loading Method	20
3.1.4 Practical Application	21
Chapter 4: Barley Radiotracer Experiment	22

4.1 Background	23
4.2 Experimental Setup	27
4.3 Data Analysis.....	30
4.3.1 Input-Output Model	31
4.4 Results	37
4.4.1 Effects of Atmospheric CO ₂ Concentration.....	37
4.4.2 Effects of Nutrient Treatment	40
4.4.3 Variance in Export Fractions	42
4.4.4 Interpretations of Fractional Allocation using Measured Photosynthetic Rates	46
4.5 Findings and Discussion.....	50
Chapter 5: Small Plant PET Imaging	54
5.1 PET Imaging System.....	55
5.2 Image Reconstruction.....	56
5.3 Positron Range Effect.....	57
5.4 PhytoPET Benchmark Validation	60
5.4.1 Corn Seedling Experiment using ¹¹ C- ¹⁴ C.....	60
5.4.2 Plant Stem Phantom using ¹¹ C-NaOH.....	61
5.5 Monte Carlo Modeling.....	64
5.5.1 Geometry	64
5.5.2 Radioactive Sources	65
5.5.3 Sensitive Detector	66
5.5.4 Geant4 Simulation – Stem Phantom	66
5.5.5 Geant4 Simulation – Corn Leaf	68

Chapter 6: Direct Positron Detection	71
6.1 Silicon Strip Detectors	74
6.1.1 Advantages using Silicon Strip Detection	76
6.1.2 Challenges using Silicon Strip Detection	76
6.2 Monte Carlo Simulations.....	76
6.2.1 Spherical Source Simulation	77
6.2.1.1 Reconstructed Image.....	78
6.2.1.2 Energy Deposited.....	78
6.2.1.3 Scattered Events	80
6.2.1.4 Signal Readout Electronics	81
6.2.1.5 Silicon Signal-to-Noise Estimate.....	81
6.2.2 Radioisotopes Comparisons	83
6.2.3 Planar PET Imaging vs. Direct Positron Detection.....	85
6.3 In Closing	87
Appendix A: Carbon-11 Gas Transfer and Labeling Loop.....	89
Appendix B: Glossary	93
Appendix C: Leaf Cuvette Development	94
Appendix D: Input-Output Model Results.....	96
Appendix E: Photosynthetic Rate Derivations.....	100
Appendix F: Geant4 Simulation Procedures	108
Bibliography	110
Biography	123

List of Tables

Table 1. Common radioisotopes produced at TUNL for plant research.....	10
Table 2. Inorganic crystal scintillators and their gamma-ray detection properties.....	13
Table 3. Summary of data collection activities.	26
Table 4. Effects of atmospheric CO ₂ concentration on carbohydrate allocation in barley.	40
Table 5. Effects of atmospheric CO ₂ concentration on root exudation and respiration. ...	40
Table 6. Effects of abrupt changes in the nutrient availability on belowground allocation, root exudation, and respiration	41
Table 7. Average photosynthetic rates and nutrient breakdown under ambient and elevated CO ₂	48
Table 8. Relative vs. absolute amount of carbohydrates allocated under ambient and Elevated [CO ₂].....	49
Table 9. Common PET radioisotopes produced at TUNL and their mean range in water (from [Che03]).....	59
Table 10. Effects of acrylic positron conversion on PET counting statistics..	70
Table 11. Geant4 simulation recorded events for PET and direct positron detection imaging using identical ROI in ImageJ.....	86
Table 12. Summary of components that make up the labeling loop between TUNL and the Phytotron facilities..	90
Table 13. Barley plant detail summary with experimental parameters for individual plants.....	96
Table 14. Effects of elevated atmospheric CO ₂ concentration on carbon allocation and transport under High and Low nutrient levels for barley.	97
Table 15. Effects of ambient atmospheric CO ₂ concentration on carbon allocation and transport under High and Low nutrient levels for barley.	98
Table 16. Average values of values from Tables 15 and 16 and number of samples in each category.....	99

Table 17. Average values for each category presenting the effects of switching nutrient treatments for both ambient and elevated CO₂.99

Table 18. Photosynthetic rate measurements for ambient atmospheric CO₂ conditions.100

Table 19. Photosynthetic rate measurements for elevated atmospheric CO₂ conditions.....100

List of Figures

Figure 1. Diagram of positron annihilation. The radioactive nucleus decays emitting a positron (e^+) and a neutrino (ν). This figure is taken from [Kis08].	4
Figure 2. Theoretical positron kinetic energy spectra for ^{18}F , ^{11}C , ^{13}N , and ^{15}O (normalized to have equal area under the curves) adapted from [Lev99].	7
Figure 3. Map of the Phytotron and TUNL facility separated by an approximate distance of 100 meters (from [Kis08]).	8
Figure 4. Diagram of the LabVIEW control panel for the carbon-11 tagged air circulation system.	11
Figure 5. Depiction of CO_2 uptake in the area of leaf tissue exposed to surrounding air.	16
Figure 6. Simple diagram of radioactive gas labeling loop with IRGA in line with uptake leaf cuvette and circulation pump.	18
Figure 7. Graph of the $[\text{CO}_2]$ in the closed gas labeling loop as a function of time.	19
Figure 8. Simple diagram of labeling loop connected to a mass flow controller (MFC).	20
Figure 9. A simplified depiction of the carbohydrate pathways within a plant (adapted from [Kis08]).	24
Figure 10. Diagram of the experimental setup used to measure whole plant carbon allocation dynamics, including root exudation and respiration.	27
Figure 11. Example of radiotracer profiles for relative accumulation of ^{11}C -tagged carbohydrates in barley seedling.	33
Figure 12. (a) Example of radiotracer input and output profiles for relative accumulation of ^{11}C -tagged carbohydrates in barley seedling, (b) example of a derived model fit to output data.	35
Figure 13. Plots of the time dependence of the activity in regions D (root exudation-red line) and E (root respiration-blue line), (from [Kis08]).	37
Figure 14. Effect of measurement time of day on the leaf export fraction.	38
Figure 15. Effects of atmospheric CO_2 levels on carbohydrate allocation and transport in barley.	39
Figure 16. Variability in leaf export (A), shoot export (B), and belowground allocation (C) fractions.	44

Figure 17. Variability in root respiration (D) and root exudation (E) export fractions.....	45
Figure 18. Variance in the measured photosynthetic rate for barley grown in either ambient or elevated [CO ₂].	46
Figure 19. Average photosynthetic rate for barley grown in either ambient or elevated [CO ₂]	47
Figure 20. (Left) Photographs of LYSO array and (center) assembly with readout circuits and PSPMT. (Right) Flood image of LYSO:Ce array using a 0.25 mm ³ Na-22 point source. (from [Wei13]).	55
Figure 21. Schematic of general iterative reconstruction algorithm.	57
Figure 22. (Left) Picture of corn plant in hydroponic solution. (Center) Reconstructed image is shown with ¹¹ CO ₂ as radiotracer. (Right) Photo of leaf volume surrounded by plastic converter.	60
Figure 23. (Left) Photograph from radiotracer experiment conducted at TUNL of corn plant in sealed leaf cuvette, (center) 3 mm-thick acrylic positron converter around lower portion of the same corn leaf pictured on the left, and (right) 2D reconstructed image is shown.....	61
Figure 24. (Left) Picture of cross-section of a dicot (squash) stem showing the phloem and xylem (from [Bou06]). (Right) A magnification of the phloem tissue is shown with scaling (from [Buc00]).....	62
Figure 25. Photograph from radiotracer experiment conducted at TUNL of stem phantom positioned a distance 3-cm away from the PhytoPET imaging system. (Right) A 3 mm-thick acrylic positron converter is placed around the stem phantom for comparison purposes.	63
Figure 26. (Left) Screen output from Geant4 simulation of stem and PhytoPET detectors with two-thirds of the phantom surrounded by an (white) acrylic converter and (right) reconstructed image of simulation data.	67
Figure 27. (Left) Midvein cross-section of corn seedling (thickness = 0.4 mm) using 40x magnification. (Center) Screen output from Geant4 simulation of LYSO array and leaf surrounded by plastic shield and (right) reconstructed image of simulation data.....	69
Figure 28. Rendering of proposed detector module consisting of a silicon strip detector coupled to a BGO scintillation detector assembly.	73
Figure 29. Diagram of positron tracking using silicon strip and PET detector coincidence events.....	73
Figure 30. Cross section of a double-sided detector. Image adapted from [Kra01].	74

Figure 31. Stopping power vs. kinetic energy for positrons in silicon (left) and graph of electron range in silicon (right). Figure referenced from [Ber99] and [Spi99], respectively.	75
Figure 32. Geant4 screen output of simple dual detection geometry that includes a BGO detector (white), silicon material (blue), and an ^{11}C point source.	77
Figure 33. Reconstructed image of 0.25 mm ^{11}C point source.	78
Figure 34. The deposited energy from positrons incident on silicon.	79
Figure 35. Simulated angular distribution of transmitted positrons in 200 μm silicon target for ^{11}C theoretical energy spectrum.	80
Figure 36. Block diagram of proposed silicon strip detection system.	81
Figure 37. Reconstructed images for 0.5 mm point source of ^{11}C , ^{13}N , and ^{15}O , respectively.	83
Figure 38. Simulated angular distribution of transmitted positrons in 200 μm silicon target for ^{11}C (left) theoretical energy spectrum and 5 MeV (right) positrons.	84
Figure 39. (Left) Geant4 simulation graphic rendering of PET detector setup and (Right) direct positron dual detection.	85
Figure 40. (Left) Geant4 graphic rendering of leaf model and mid vein. (Right) Reconstructed images of leaf source emitting positrons having kinetic energies of 2 MeV, 5 MeV, and 10 MeV from left to right.	86
Figure 41. Screenshot of the LabVIEW controlled radioactive gas handling system for transfer from the $^{11}\text{CO}_2$ production area located at TUNL to the labeling chamber at the Phytotron.	89

Chapter 1: Introduction

Positron Emission Tomography (PET) imaging and coincidence counting can be used in non-clinical applications for real-time measurements of radiotracer allocation and transport. This dissertation describes the use of PET imaging techniques to measure the distribution of short-lived radioactive tracers in small plants to provide information about the dynamic plant response to changes in their local environment. In our dynamic short-term studies, radiotracers are chosen that decay by positron (e^+) emission. The physics of positron decay is beneficial for imaging and coincidence counting. During positron decay, positrons interact with electrons in their local vicinity and will eventually annihilate when they reach thermal energies. The annihilation interaction produces two anti-collinear gamma rays that can be detected by a pair of detectors on opposite sides of the location of annihilation. Detector measurements are used to project a line that represents the annihilation event line. This line is called a line of response (LOR). The summation of all LORs collected by the detection system provides an estimate of the activity concentration within the field of view (FOV) of the detector arrays.

The thin nature of plant tissue presents challenges in positron emission tomography (PET) imaging in comparison to small animal subjects. Positrons emitted from unstable nuclei travel a finite distance within the material of the sample before annihilating and producing two collinear gamma rays. The range is determined by the initial energy of the emitted positron and the electron density of the surrounding medium [Leh11]. The fraction of positrons escaping from above-ground tissue of a typical seedling tend to be large, e.g., greater than 50% [Ale11]. This large escape fraction poses challenges in the accuracy of determining the radiotracer accumulation and

transport. Positron range can be a significant issue for imaging crop species, e.g., barley and corn, where the majority of above ground structure is composed of thin leaves. A central motivation for this project was to develop methods that mitigate positron range effects in PET and gamma-ray coincidence counting measurements in plant studies. Direct positron detection can improve statistical accuracy when appropriate corrections are applied. Each detector module in the proposed system consists of a double-sided silicon strip in coincidence with a 2D position sensitive inorganic scintillator mounted immediately behind the silicon strip detector. The direction of the strips in the two planes of the silicon detector are orthogonal.

1.1 Background

In this thesis project we used radio-isotope labelled compounds to study the time-dependent response of a model crop species, barley, to abrupt shifts in the nutrient availability under either ambient or elevated atmospheric CO₂ concentrations. We aimed to measure a large sample of plants within our experimental timeframe to further understand the magnitude of biological responses in the barley species. The ¹¹C isotope was used in these studies to tag newly synthesized carbohydrates, and a combination of PET imaging and coincidence gamma-ray counting were used with the pulse loading method to determine time-dependent carbon allocations throughout the entire plant, including leaves, the stem and roots. In addition, the root exudation of freshly made carbohydrates and respiration of CO₂ were measured for some plants. In the pulse loading method, the ¹¹CO₂ gas is injected abruptly into the closed air circulation loop that contains the cuvette where the leaf is in contact with the radioactive gas. This loading

method enables time tracking of the ^{11}C pulse from the time it is absorbed by the leaf and integrated into sugar compounds via photosynthesis.

This study can be useful in the understanding of the mechanisms plants use to regulate resources in response to changes in their local external environment especially with continuous changes in Earth's abiotic environment, e.g., local soil nutrient availability, and gradually increasing atmospheric CO_2 levels. Studying plant responses to nutrient changes could help isolate the mechanism(s) involved in the acclimation to shifts in environmental conditions. The translocation and allocation of carbon, as carbohydrates, identifies the relative demand for newly synthesized carbohydrates in regions throughout the plant for metabolic activities associated with growth or for storage. Varying access to key resources used by plants for growth provide insight on the time constant for these mechanisms. In our experiments, carbon and nitrogen were the resources monitored

1.2 Fundamentals of Radiotracer Experiments

Short-lived positron-emitting isotopes allow for real-time measurements of radiotracer-labeled metabolites in small plants. Positron emission occurs when an unstable proton-rich nucleus achieve stability by converting a proton into a neutron. After conversion, an electron neutrino (ν_e) and positron (e^+) share the energy released from the reaction:



A is the mass number, Z is the atomic number, and N is the number of neutrons. In positron decay the parent nucleus releases a positron and is then referred to as a

daughter atom with a reduction in the atomic number (Z-1) and an increase in the number of neutrons (N+1). The positron energy spectrum is continuous and unique to the nucleus of origination. Once the positron reaches thermal energy, it will annihilate with an electron in the surrounding medium, resulting in the emission of two anti-collinear 511-keV gamma rays, as shown in Fig. 1. In this project, carbon-11 (^{11}C) is the primary radioisotope used in carbohydrate tracking. The ^{11}C is produced using the $^{14}\text{N}(p,\alpha)^{11}\text{C}$ reaction induced with a 10-MeV proton beam using a tandem Van de Graaff accelerator. Coincidence counting of the gamma rays emitted from positron annihilation provides an efficient means of tracking the gross movement of labeled substances between plant organs. In our experiments, scintillation detectors are used to detect the emitted 511-keV gamma rays. The three types of inorganic crystal scintillation detectors were used in our coincidence measurements: bismuth germanium oxide (BGO), lutetium-yttrium oxyorthosilicate (LYSO), and cesium fluoride (CsF).

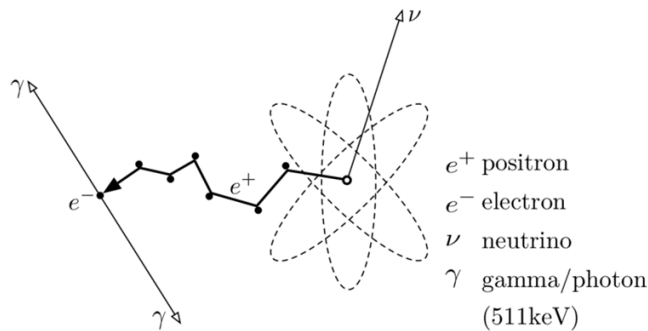


Figure 1. Diagram of positron annihilation. The radioactive nucleus decays emitting a positron (e^+) and a neutrino (ν). This figure is taken from [Kis08].

Detectors are placed on opposite sides of the plant to measure the radiotracer accumulation in various regions: uptake leaf, stem, and root. High resolution images can

be obtained by using pixelated scintillator arrays for PET imaging. Small detector elements can also provide coincidence measurements of annihilation gamma rays.

PET imaging is a noninvasive method for collecting quantitative information about the radiotracer distribution through the plant. We apply PET imaging techniques to measure radiotracer accumulation profiles for plants acclimated to various environmental conditions. Radiotracer accumulation profiles for each plant region are corrected for background radioactivity, relative detection efficiency, and radioactive decay during analysis, and are used in calculating export fractions from each organ during the allotted measurement period.

1.3 Motivation

1.3.1 Absolute Activity from Coincidence Counting

The term activity refers to the number of nuclear transformations in a given period of time. The absorption of ^{14}C as a function of the photosynthetic rate also allows to estimate the total activity in the plant due to leaf uptake of CO_2 gas. Our goal is to directly measure the photosynthetic rate using methods presented in chapter 3 for application to our analysis and interpretation of acquired radiotracer data, presented in chapter 4. To accurately quantifying the absolute activity in a given volume, the physical effects associated with positron decay and annihilation must be taken into consideration [IAE14]. Positron range is the most dominant physical effect that reduces the measured detector counts, leading to inaccurate radioactivity estimations. Other physical effects include natural radioactive backgrounds, the geometric acceptance of the detector, and the detector system counting efficiency.

1.3.2 Improving Counting Statistics

When using coincidence counting to measure radiotracer spatial distributions, one must consider the geometry and efficiency of counting detectors. Detectors may only interact with a fraction of incident gammas based on the solid angle subtended by the detector in viewing the source of the radioactivity [Cha77]. Once geometric factors are compensated for, the major hurdle for measuring the absolute activity is positron range effects in plant tissue.

Positron range has the most significant impact on counting statistics in plant imaging studies. Positrons originating in the leaf and other thin segments of the plant may travel outside the field of view of the detector before annihilating with an electron. This reduces the counts in a given region. In this project, the fraction of counts lost to positron range effects are determined using Monte-Carlo simulations of the source and detector arrangement. Geant4 simulations are used to model the plant geometry in our experiment setups with positrons originating inside the tissue of interest.

The theoretical energy spectra for common PET radioisotopes are shown in Fig. 2. ^{11}C has a relatively low average positron energy of 0.326 MeV. Range effects become more pronounced when using higher energy positron emitters such as ^{13}N and ^{15}O , whose average positron energies are 0.432 and 0.696 MeV, respectively. In our small plant imaging experiments, a 3-mm thick plastic annihilator is placed around the plant stem and leaf to increase the probability of annihilation within the detector FOV.

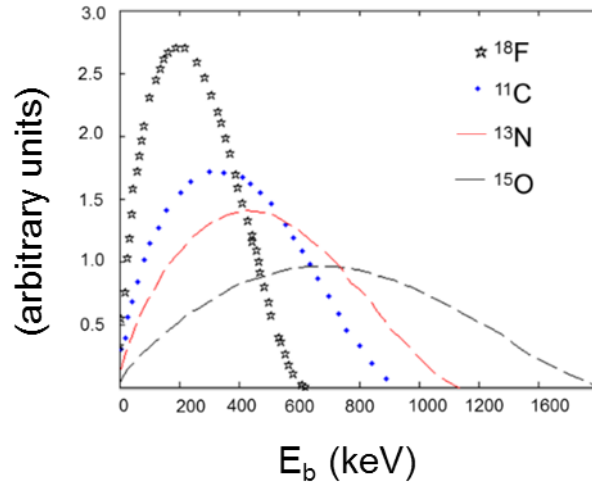


Figure 2. Theoretical positron kinetic energy spectra for ^{18}F , ^{11}C , ^{13}N , and ^{15}O (normalized to have equal area under the curves) adapted from [Lev99].

While reducing the impact of the range problem in plants, the use of plastic annihilators has several adverse effects on the measurements. The drawbacks of using plastic annihilators includes blurring of the reconstructed images, scattering and attenuating annihilation gammas, and interfering with normal plant physiology, e.g., lower air flow to plant tissue that likely alter light quality and gas concentration around the leaf (e.g. CO_2 and water vapor) and may cause temperature fluctuations at the surface of the plant being studied. An alternate solution to using acrylic converters would be to incorporate a Monte-Carlo estimate of the counts lost due to positron range based on the particular plant anatomy. The loss fraction in each plant organ can be used to scale measured counts to provide an absolute quantity of radiotracer accumulation for that particular organ.

Chapter 2: Radiotracer Production and Gamma Detection

The experimental methods used in the production and distribution of common PET radioisotopes for measuring accumulation and allocation in small plants will be described in this chapter. The radioisotope, ^{11}C (twenty-minute half-life), used in this work is produced by a tandem Van de Graaff accelerator operated by the Triangle Universities Nuclear Laboratory (TUNL). The Van de Graaff accelerator facility occupies the basement level of the TUNL building, which is located on the west campus of Duke University. The accelerator laboratory is staffed by research scientists, accelerator technicians, and physics faculty members. Students and other researchers from Duke, UNC-Chapel Hill, and NC State University also conduct research at this facility. The Van de Graaff accelerator has a maximum terminal voltage capability of 10 MV, which can accelerate protons (H^+ ions) to a maximum energy of 20 MeV.

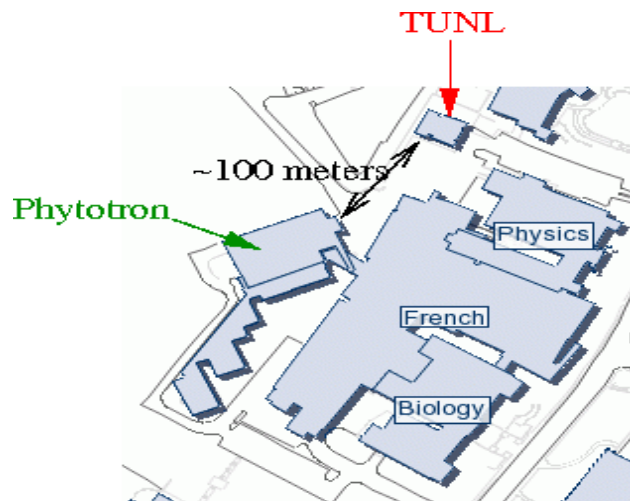


Figure 3. Map of the Phytotron and TUNL facility separated by an approximate distance of 100 meters (from [Kis08]).

Gases tagged with radioisotopes are transported underground via dedicated gas lines from the tandem laboratory to the Phytotron where the plant imaging measurements are performed. The tagged gas is loaded into a custom-designed gas handling system that circulates the gas in a closed loop over a leaf (or leaves) of the plant being studied. The Phytotron is located approximately 100 meters from the tandem laboratory, as shown in Fig. 3. It houses controlled-environment growth chambers that have the capabilities of controlling and monitoring the environment where plants are grown and studied with high precision. A growth chamber allows for the precise control of light intensity, local air temperature, humidity, and atmospheric carbon dioxide (CO₂) concentration.

2.1 Radioisotope Production

Our most commonly used radioisotope, ¹¹C, is produced using the ¹⁴N(p,α)¹¹C reaction by bombarding a gas cell with a 10-MeV proton beam. The gas cell is 3 cm long and pressurized to 6 atm. With high purity (HP; 99.999%) nitrogen-14 (¹⁴N) gas. There are sufficient amounts of oxygen ions in the HP nitrogen gas for the ¹¹C to combust in the beam heated gas to form ¹¹CO₂ and ¹¹CO. The ¹¹CO₂ is mechanically separated from the CO and N₂ gases by passing the mixed gas through a liquid nitrogen (LN) cooled trap; the CO₂ freezes while the other gases are pumped away. The beam entrance window on the gas cell is a 0.25-mil thick Havar foil. A proton beam current of 1.5 microamps (μA) will generate a ¹¹C sample of approximately 20 milliCuries (mCi) radioactivity in thirty minutes of beam on target.

It is also possible to produce ¹³N using the ¹⁶O(p,α)¹³N reaction by bombarding a water target with a 10-MeV proton beam. The water is circulated to prevent the system

from overheating due to the power deposited in the target by the proton beam and to minimize effects of cavitation within the target. In addition to removing heat from the water, the circulating water passes through an alumina-filled sieve to scrub the fluorine ions produced by the $^{18}\text{O}(\text{p},\text{n})^{18}\text{F}$ reaction. A proton beam current of about 1.5 μA on target for fifteen minutes will produce a ^{13}N sample of approximately 20 mCi radioactivity. Other short-lived isotopes that can be produced at the TUNL facility are listed in Table 1.

Table 1. **Common radioisotopes produced at TUNL for plant research.**

Radionuclide	$T_{1/2}$	β^+ E_{max} (MeV)	β^+ E_{mean} (MeV)	Production Reaction	Reaction Q-value (MeV)	Tagged Compound
^{11}C	20.4 min	0.959	0.326	$^{14}\text{N}(\text{p},\alpha)^{11}\text{C}$	-2.92	$^{11}\text{CO}_2$
^{13}N	9.96 min	1.197	0.432	$^{16}\text{O}(\text{p},\alpha)^{13}\text{N}$	-5.22	$^{13}\text{NO}_3$
^{15}O	2.03 min	1.738	0.696	$^{14}\text{N}(\text{d},\text{n})^{15}\text{O}$	5.07	H_2^{15}O
^{18}F	110 min	0.633	0.202	$^{18}\text{O}(\text{p},\text{n})^{18}\text{F}$	-2.44	$\text{H}_2\text{O}+^{18}\text{F}^-$

2.2 Radiotracer Transport System

The radiotracers produced at TUNL are transported to the dedicated controlled-environment chamber at the Phytotron facility. Two separate transport systems were developed for transferring the $^{11}\text{CO}_2$ gas and the $^{13}\text{NO}_3^-$ liquid solution to the labeling experiments in the Phytotron.

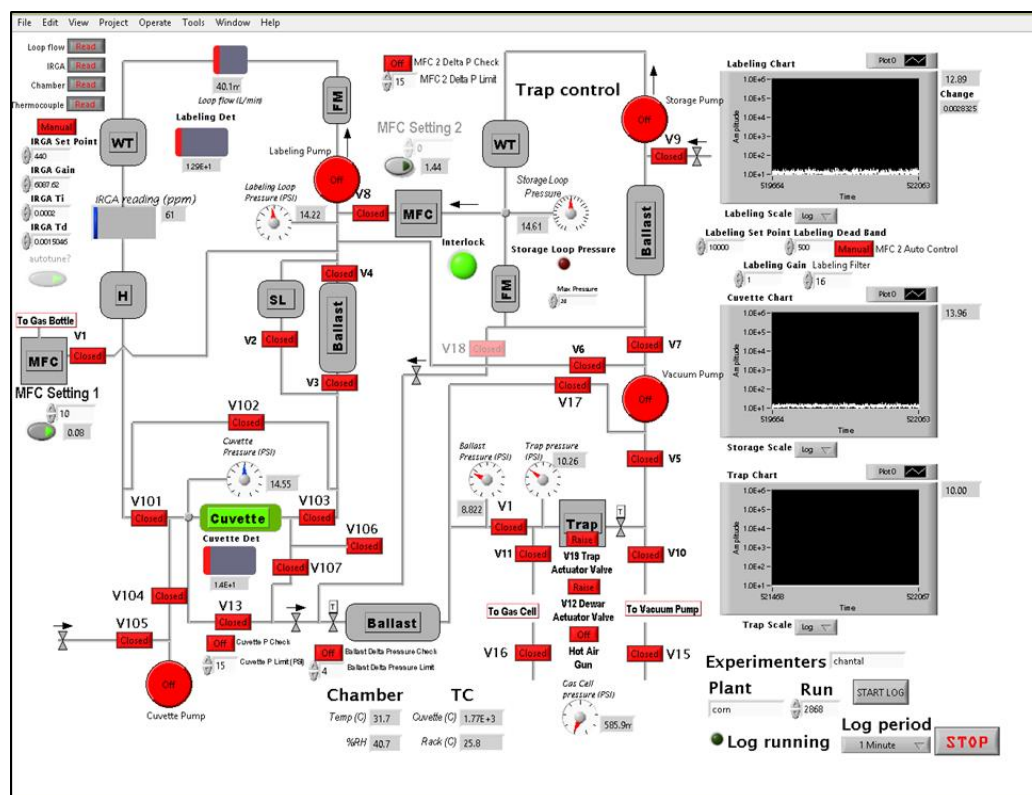


Figure 4. Diagram of the LabVIEW control panel for the carbon-11 tagged air circulation system.

There are two gas loops. The loop on the left is the labeling loop where the plant is being studied. The loop on the right is for storing $^{11}\text{CO}_2$ for use in continuous loading measurements. The symbol key for this diagram is as follows: FM = flow meter, H = humidifier, IRGA = Infrared Gas Analyzer, MFC = mass flow controller, SL = soda-lime trap, TC = thermal couple, Trap = LN cooled trap, V# = valve, and WT = water trap.

Once the radiotracer is generated, the liquid or gas pump compound is immediately transported to the labeling system in the Phytotron. Once transferred to the Phytotron, the $^{11}\text{CO}_2$ is isolated from the other gasses in the mixture by passing the gas through a liquid nitrogen (LN) cooled trap at 77 K. The CO_2 freezes at 195 K (at atmospheric pressure), while other components (CO and N_2) remain in the gas phase at LN temperature and atmospheric pressure. The freezing temperature of CO at atmospheric

pressure is 68K, which is below the temperature of the LN bath. The gas labeling system is controlled with LabVIEW. A diagram of the control panel is shown in Fig. 4.

A pneumatic tube transport system was installed to transport radioisotope tagged liquids from the tandem lab to the Phytotron. A system of aluminum conduits connect the target room in the tandem lab where the radiotracers are produced to the plant labeling area in the Phytotron. A blower pushes the sealed container holding the aqueous of the radioisotope solution through a custom-designed underground conduit system.

2.3 Gamma Detection

2.3.1 Coincidence Counting

Prior to adopting PET imaging techniques for data collection, coincidence counting was the primary technique used in carbon tracking measurements. Carbon-11 radioactively decays by positron emission. The emitted positron can interact with electrons in the surrounding medium to produce two collinear gamma rays each having energy of 0.511 MeV. Since the gamma rays travel in opposite directions along the same line, gamma detectors can be utilized for coincidence tracking. Coincidence detection allows for the distribution of radiotracer within the plant to be measured as a function of time.

Scintillator crystal detectors are optically coupled to a photomultiplier tube (PMT). The gamma rays from positron annihilation may interact in the detector crystal by exciting atoms and molecules. As the atoms and molecules de-excite, photons are emitted that may hit the photocathode on the PMT and result in electrons being emitted, multiplied by the cascade down the dynode chain and collected on the PMT anode. There are various types of scintillator crystals having specific intrinsic properties that

must be considered when designing or implementing a gamma-coincidence detection system or PET imager. The important specifications include the energy resolution, time response, cost/volume, and detection efficiency/volume. Properties of standard inorganic crystal scintillators are shown in Table 2. For our experiments, square BGO (2.75" x 2.75" x 1" thick) detectors were used for coincidence counting measurements.

Table 2. Inorganic crystal scintillators and their gamma-ray detection properties.

Inorganic Crystal	Effective Atomic Number (Z)	Density (g/cm ³)	Decay Constant (ns)	Emission Intensity [NaI(Tl) = 100]	Emission Wavelength (nm)
NaI(Tl)	51	3.67	250	100	410
BGO	73	7.13	300	15	480
CsF	49	4.64	4	5	390
Prelude@420	65	7.10	41	75	420
GSO	58	6.71	60	30	430

Cylindrical cesium fluoride (CsF) detectors (1" diameter x 1" thick) were used for monitoring the radiation levels in the labeling loop as a single detector counter. Despite the low light output, the short decay time (4 ns) of CsF detectors make them well suited for use in high-rate counting rate applications. Prelude detectors were coupled together and measured 3.0" x 1.0" x 1.0". These detectors were also used for their high-rate counting capabilities due to their relatively low decay time (41 ns). Prelude detectors were placed around the uptake leaf where the initial count rate would be highest.

Chapter 3: Methods to Estimate the Photosynthetic Rate

Terrestrial plants rely on the photosynthetic process to absorb CO₂ from air surrounding the leaf and water from the soil. Plants use solar energy to split water molecules (H₂O) and convert carbon dioxide (CO₂) gas into simple and complex carbon compounds, for either immediate use or as a stored source of energy. In this chapter, techniques will be discussed for determining the total photosynthetic rate per leaf area, thereby providing an estimate of the absolute number of carbon molecules synthesized into ¹¹C-tagged carbohydrates. A general chemical process of photosynthesis for producing glucose is summarized below:



This simplified reaction actually consists of more than 50 intermediate steps, and these can be classified as either light or biochemical reactions [Tai02]. The light reactions refer to the incorporation of sunlight energy into chemical energy, i.e., photon absorption by leaf pigments and electron transport from the splitting of water to form NADPH (nicotinamide adenine dinucleotide phosphate-oxidase) and ATP (adenosine triphosphate), two common chemical potential energy molecules. Both molecules fuel the biochemical reactions to convert absorbed carbon dioxide into carbohydrates, mainly glucose and fructose. Recently fixed glucose is either stored in leaf tissue mostly as starch (linked glucose chain) or loaded in the phloem vascular bundle as sucrose (a glucose-fructose unit) for transport to regions of the plant in need of carbohydrates for their metabolic activities. Because CO₂ is a primary substrate for the photosynthetic process, the current and projected increase in atmospheric CO₂ concentration should benefit plant growth. However, feedback between sugar production and sugar export out

of the leaf has mitigated photosynthesis [Sti99; Lea09] requiring better methods for understanding the sugar transport out of the leaf to other regions of the plant.

The transport of carbohydrates from the leaf to other plant tissues occurs in a highly specialized group of vascular tissue called the phloem. The phloem vascular bundle consists of interconnected sieve tube elements that use hydrostatic pressure to induce mass flow of sugar molecules throughout the plant. The export of carbohydrates from a source leaf and its transport to other organs is controlled by the demand for carbohydrates by these sinks.

3.1 Total Sugar Production in the Leaf

One goal of this dissertation is to develop methods for estimating the total quantity of carbohydrates produced during photosynthesis using the $^{11}\text{CO}_2$ labeling loop as a closed system. Such estimation provides useful information following radiotracer measurements for data analysis and interpretation of results, and mimics CO_2 gas exchange methods commonly used for photosynthesis. Historical ways of estimating the photosynthetic rate include (1) measuring beta emission from ^{14}C decay directly from the harvested plants, (2a) measuring the CO_2 depletion rate within the closed-loop system using infrared gas analysis, or if a constant CO_2 is needed in the loop (2b) using CO_2 injection for a null-balance approach. The last method (3) include the use of a positron emitter such as $^{11}\text{CO}_2$ and scintillation detection to monitor radioactivity changes in the closed gas loop system [Hun03]. We propose to compare methods (2) and (3) for measuring the photosynthetic rates in our experiments.

Determining the photosynthetic rate is important for providing additional insight on the dynamics of carbohydrate transport from source to sink tissues. Knowledge of

measured photosynthetic rates concomitant with transport and allocation ensure that conclusions drawn based on changes in fractional changes in allocation patterns actually reflect the total sugar content allocated to a particular plant region.

The uptake of atmospheric CO₂ inside the leaf is regulated by the opening and closing of stomata. In its simplest form, the uptake of CO₂ gas into the leaf is proportional to the concentration gradient between air and the site of carboxylation inside the leaf with a flow rate given by:

$$J = D * (\rho_2 - \rho_1) \quad (3.2)$$

D is the effective leaf stomatal conductance, ρ_1 and ρ_2 are the CO₂ gas densities on the inside of the leaf and outside of the stomata, respectively. By monitoring the concentration of CO₂ in the closed-loop system and evaluate the change in CO₂ as a function of time, we are able to measure the flow rate, J . It follows that the photosynthetic rate is proportional to the CO₂ uptake corrected for the effective leaf area labeled (Fig. 5). In the following sections, experimental methods to measure the uptake rate of CO₂ for photosynthesis will be presented.

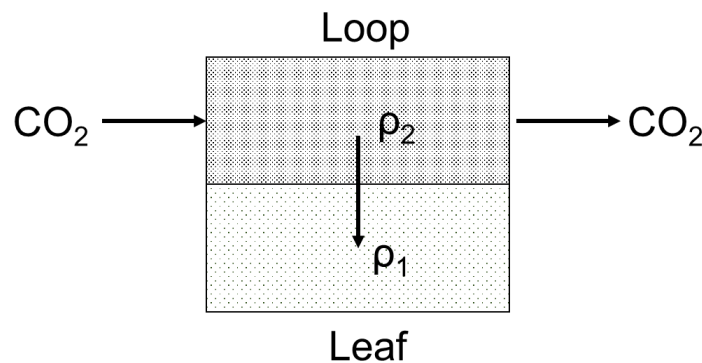


Figure 5. Depiction of CO₂ uptake in the area of leaf tissue exposed to surrounding air.

3.1.1 Estimation of Photosynthetic Rates using CO₂ Depletion in Closed-Loop System

The CO₂ depletion method consists of continuous monitoring of carbon dioxide concentration ([CO₂]) within the closed labeling-loop using an infrared gas analyzer (IRGA). The [CO₂] is determined by comparing the transmittance of infrared radiation through the gas in a reference control volume to that of the labeling loop sample volume. CO₂ absorbs infra-red radiation in specific IR wavebands [Cle78]. As the concentration of CO₂ decreases in the loop volume, the amplitude of the signal from the infra-red detector increases. Because the labeling loop is a closed system, plant photosynthetic processes will decrease the loop's CO₂ concentration with time when in daylight. This enables the photosynthetic rate to be determined by monitoring the CO₂ concentration in the loop with an IRGA (Fig. 6). A downside of this method is that the photosynthetic rate is directly affected by the [CO₂] in the closed loop system and thus a decreasing [CO₂] will result in a gradual decline in the photosynthetic rate. Therefore, this measurement technique must be improved upon by keeping the [CO₂] in the closed-loop system constant.

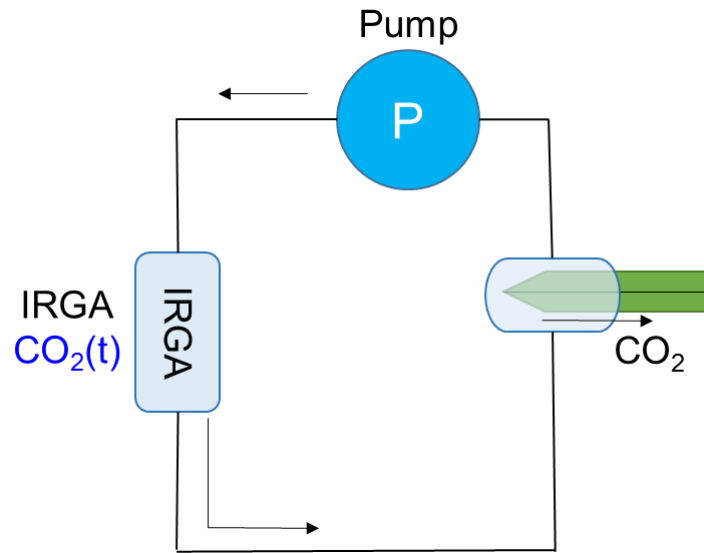


Figure 6. Simple diagram of radioactive gas labeling loop with IRGA in line with uptake leaf cuvette and circulation pump.

Using this approach, the photosynthetic rate in $\mu\text{mol m}^{-2} \text{s}^{-1}$ (P_s) is given by:

$$P_s = \frac{Pressure_{loop} * Volume_{loop}}{Leaf Area * R * Temperature_{cuvette}} * \frac{d[IRGA]}{dt} \quad (3.3)$$

R is the gas constant which equals $8.206 \times 10^{-5} \text{ m}^3 \text{ atm K}^{-1} \text{ mol}^{-1}$. $d[IRGA]/dt$ is the slope of the depletion rate of $[\text{CO}_2]$ in the closed labeling loop as a function of time, as visualized in the graph in Fig. 7. The complete derivation can be found in Appendix E.

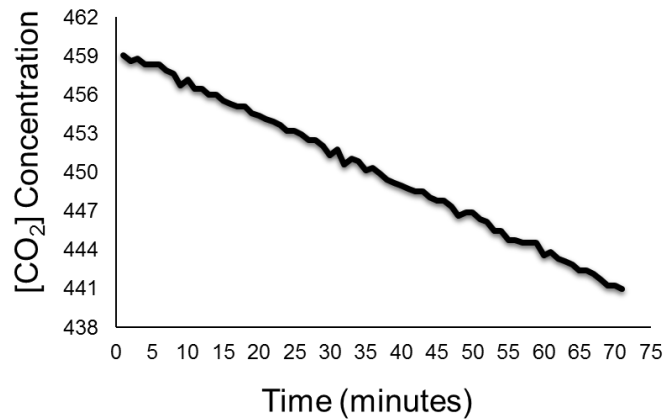


Figure 7. Graph of the [CO₂] in the closed gas labeling loop as a function of time.

3.1.2 Estimation of Photosynthetic Rate using CO₂ Depletion in Closed-loop System while Compensating for Leaf CO₂ Uptake

The null balance approach to estimate photosynthesis relies on monitoring the CO₂ concentration in the loop to maintain the [CO₂] at a constant level by compensating for the leaf CO₂ uptake. The CO₂ injection is regulated by a mass flow controller (MFC) as depicted in Fig. 8. Once the system reaches a steady state, the photosynthetic rate is directly proportional to the MFC rate adjusted for the CO₂ concentration of the added air.

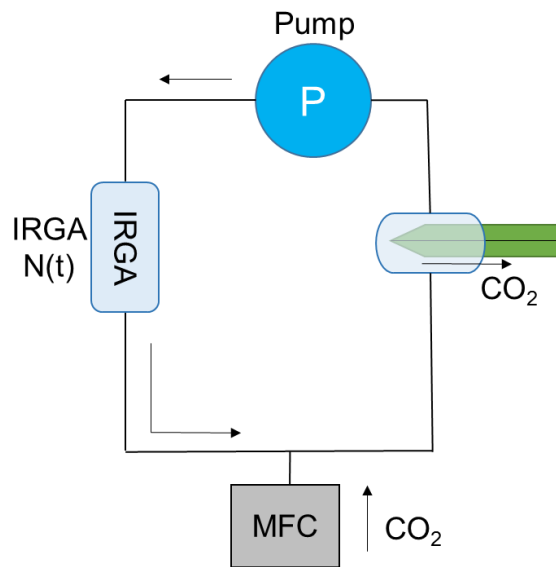


Figure 8. Simple diagram of labeling loop connected to a mass flow controller (MFC).

Using this steady-state approach, the rate of photosynthesis in $\mu\text{mol}/\text{m}^2/\text{s}$ (P_s) is calculated using a modified version of Equation 3.3 to correct for CO_2 injection and becomes:

$$P_s = \frac{c * Pressure_{loop}}{Leaf\ Area * R * Temperature_{cuvette}} * [MFC(t)] \quad (3.4)$$

$MFC(t)$ is the MFC flow rate in cm^3/min , and c is the $[\text{CO}_2]$ gas concentration factor of injected CO_2 . A typical value for c is 0.01 for the use of a CO_2 to air gas mixture ratio of 1%.

3.1.3 ^{11}C Pulse-Loading Method

The ^{11}C pulse-loading method was developed as an alternate technique for determining the absolute the photosynthetic rate. This method is based on monitoring the reduction in the radioactive pulse circulating in the closed-loop system. The reduction in the activity of $^{11}\text{CO}_2$ gas in the close loop is due to either plant absorption or

radioactive decay. Given that the radioactive decay of the ^{11}C isotope is a known constant, the photosynthetic rate can be determined in $\mu\text{mol}/\text{m}^2/\text{s}$ by:

$$Ps = J(t) * \frac{n_{CO_2}}{n_{C_{11}}} \quad (3.5)$$

$J(t)$ represents the leaf uptake of gas molecules over a given leaf area per unit time, and $n_{CO_2}/n_{C_{11}}$ is the ratio of molar concentrations of $^{12}\text{CO}_2$ to $^{11}\text{CO}_2$. The complete derivation can be found in Appendix E.

3.1.4 Practical Application

In an ideal experiment, it is preferable to monitor the reduction in $[\text{CO}_2]$ using the IRGA while replenishing CO_2 gas into the closed loop system with the MFC. This allows for accurate photosynthetic rate calculations.

$$Ps = \frac{c * Pressure_{loop}}{Leaf Area * R * T_{cuvette}} * [MFC(t)] + \frac{d[IRGA]}{dt} * \frac{Volume * Pressure_{loop}}{Leaf Area * R * T_{cuvette}} \quad (3.6)$$

In this dissertation, the photosynthetic rate was calculated using equation 3.6 and then applied to the fractional allocation results for further interpretation. The results of the photosynthetic rate measurements are presented in Chapter 4, section 4.4.4.

Chapter 4: Barley Radiotracer Experiment

The radioisotope production system and coincidence counting techniques discussed in chapter 2 were used to perform a series of experimental studies with barley (*Hordeum distichum*) as our test species. This study was designed to measure the macroscopic response of barley to changes in local environmental conditions through the dynamic translocation and allocation of carbon (carbohydrates). Nutrient availability in natural soil systems vary locally, where nitrogen is the most important and abundant inorganic nutrient necessary for plant growth and productivity [Wan16; Dau10]. The importance of nitrogen arises due to it being the major component of amino acids [Kuz13], where the critical leaf concentration is 15-40 mg g⁻¹ DM (dry mass) [Whi10], an order of magnitude greater than other important macronutrients, excluding potassium (K). Nitrogen in the soil is mostly in the form of nitrate (NO₃⁻), which does not bind readily to soil particles because of its negative charge. Chemical weathering and nutrient leaching also contribute to the limited supply of nutrients in the soil [Kuz13]. The inhomogeneity of nutrients in the soil [Eas13], requires the plant root system to search for new sources of nutrients. The motivation for this dissertation was to gain an understanding of the short-term response of barley to nutrient stress under the current (ambient) [CO₂] condition and in a future projected [CO₂] environment (elevated). Radiotracer measurements can potentially provide insight on the temporal response to shifts in nutrient conditions, if any.

Plants cannot move freely to avoid local environmental stressors such as limited water supply, low nutrient soil conditions, and light intensity [Lee10]. In order to cope with frequent changes in their environment, plants must regulate growth and

development accordingly [Sch06]. Two main resources that plants regulate are carbon and nitrogen [Dra11]. For this thesis project, we start with monitoring one resource (carbon) and managing another (nitrogen).

In addition to being the primary food source of the planet, plants play a key role in regulating the Earth's atmospheric CO₂ levels by absorption of carbon as biomass [Cur86]. Recent studies have shown that an increase in CO₂ availability leads to increased photosynthetic rates, where a larger portion of newly-synthesized carbohydrates can be allocated as root exudate to enhance microbial activity [Mad13]. Plants live in close association with soil microbes and have developed the ability to share carbon resources with microbes in exchange for nutrients from the soil [Ber12; Mus16]. The overall complexity of the root-soil system is still not fully understood and further studies in this area could prove beneficial [Hei15]. Our radiotracer measurements were designed to contribute to answering two key questions:

#1: What effect does carbon and soil nutrient availability have on carbohydrate allocation in barley?

#2: Does the short-term change in nutrient availability affect sugar allocation to below ground sinks, including root respiration and root exudation?

4.1 Background

The radiotracer ¹¹CO₂ was used to measure the effects of short-term changes in nutrient conditions on sugar allocation in barley. Barley was chosen as our species of interest due to its simple structure, fast growth cycle, and its use as a model system in early translocation studies [Tho91]. The ¹¹C-tagged carbohydrates synthesized in the leaf of barley allow for non-invasive, real-time measurements of the relative allocation of

carbohydrates in the various organs, e.g., the leaf, stem, and root. After uptake of the radiotracer in the leaf, the newly synthesized carbohydrates can either remain as stored carbohydrate or exported to other regions of the plant to provide energy and materials for growth or other metabolic functions [Tho07]. The exported carbohydrates are loaded into the phloem where they can be transported via bulk flow to either aboveground or belowground sinks.

Carbohydrates allocated below ground can be used for root structural growth, respired as CO₂ gas during maintenance processes (e.g. repair, ion uptake) or secreted to the local root environment (rhizosphere) as root exudate activities [Dra11]. The simple distribution model in Fig. 9 depicts the allocation options of recently fixed-carbon products. By changing the nutrient conditions in a hydroponic solution, we aim to compare the real-time response of barley to sudden changes in nitrogen availability for plants grown under two atmospheric CO₂ conditions. The effects of elevated atmospheric CO₂ concentration on plant physiology processes is still not well understood [Fre04]. Even though the forecasted elevated atmospheric CO₂ is a long-term factor, the current increase of 3 ppm yr⁻¹ in the last two years is unprecedented [NOAA] and current atmospheric levels are 43% greater than pre-industrial concentrations, and an understanding of the future consequences of a relatively high atmospheric [CO₂] becomes critical for forecasting crop yield through modelling and for mitigation planning.

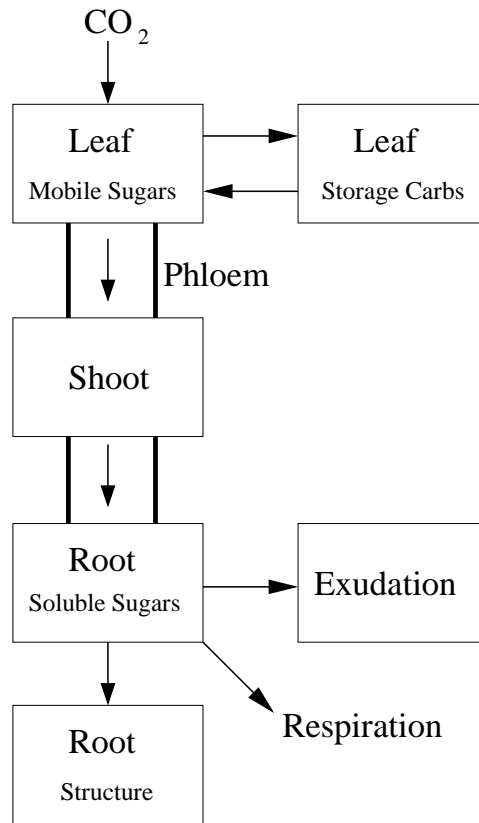


Figure 9. A simplified depiction of the carbohydrate pathways within a plant (adapted from [Kis08]).

Plant structure and physiological functions can be segmented into morphological subunits, e.g., leaves, stems, and roots. The subunits (Fig. 9) are connected through a network of tubular vascular bundles (phloem and xylem) that provide a continuous feedback mechanism enabling resource allocation and control between the subunits [Lal03].

My dissertation work builds on a team of researchers where collectively we have performed the most extensive ^{13}C tracking measurements in terms of the size of the plant sampling pool and the number of quantities measured. Measurements were performed on 31 different barley plants over a period of about 10 years, where half (15)

of those plants were measured for this dissertation project. The data collection campaigns are summarized in Table 3. As part of this dissertation, new analyses were performed on all data as one experimental set, regardless of the researcher that performed the initial measurements. Current measurements (i.e. during 2009) were combined with previous work to build upon our examination of below ground processes in barley in response to changes in nutrient conditions.

The allocation of ^{14}C -tagged carbohydrates was measured in the leaf, stem and below ground. Our measurements distinguished the below ground pool into three components: root allocation, exudation and respiration. All plants were grown and measured in hydroponic solution. Two environmental parameters were varied in this study: (1) measurements were performed for two concentrations of atmospheric CO_2 , ambient (~350 ppm) and elevated (~700 ppm), and (2) for two nutrient availabilities, high (1/2 strength of the Hoagland solution [Hoa50] and low (1/16 strength Hoagland's solution). Hoagland solution is a hydroponic nutrient mixture composed of nutrients essential for plant growth at optimal concentration for all macro and micro-nutrients for crop species.

Table 3. Summary of data collection activities.

Period	Number of Plants	Researcher	Runs
2007	6	M. Kiser	1099 - 1135
2008	10	A.S. Crowell	1299 - 1335
2009	15	L. Cumberbatch	1481 - 1527

4.2 Experimental Setup

The central goal of this study is to provide new insights on the mechanisms in plants involved in regulating resources in response to changes in external environmental conditions. Current investigations focus on the two most important elements in plant health and growth, carbon and nitrogen. New labeling experiments can be designed to decipher if the physiological response is a result of active signaling by radio-chemical tracer.

In our controlled lab setting we are able to vary the concentration of atmospheric carbon dioxide concentration ($[CO_2]$), nutrient availability, light intensity, and humidity. The $^{11}CO_2$ -tagged gas is pumped from the gas cell in the tandem lab through a liquid nitrogen cooled trap; the unwanted gases (mostly nitrogen and carbon monoxide) are pumped through the trap and exhausted up the high-speed ventilation system in the tandem lab.

BGO detectors (2.75" x 2.75" x 1") were used to monitor radiotracer accumulation in specific regions of the plants. To ensure positron annihilation close to the point of origin and within the FOV of the detectors, a 3-mm thick plastic shield was placed near the plant surface. A diagram of the experimental setup is shown in Fig. 10.

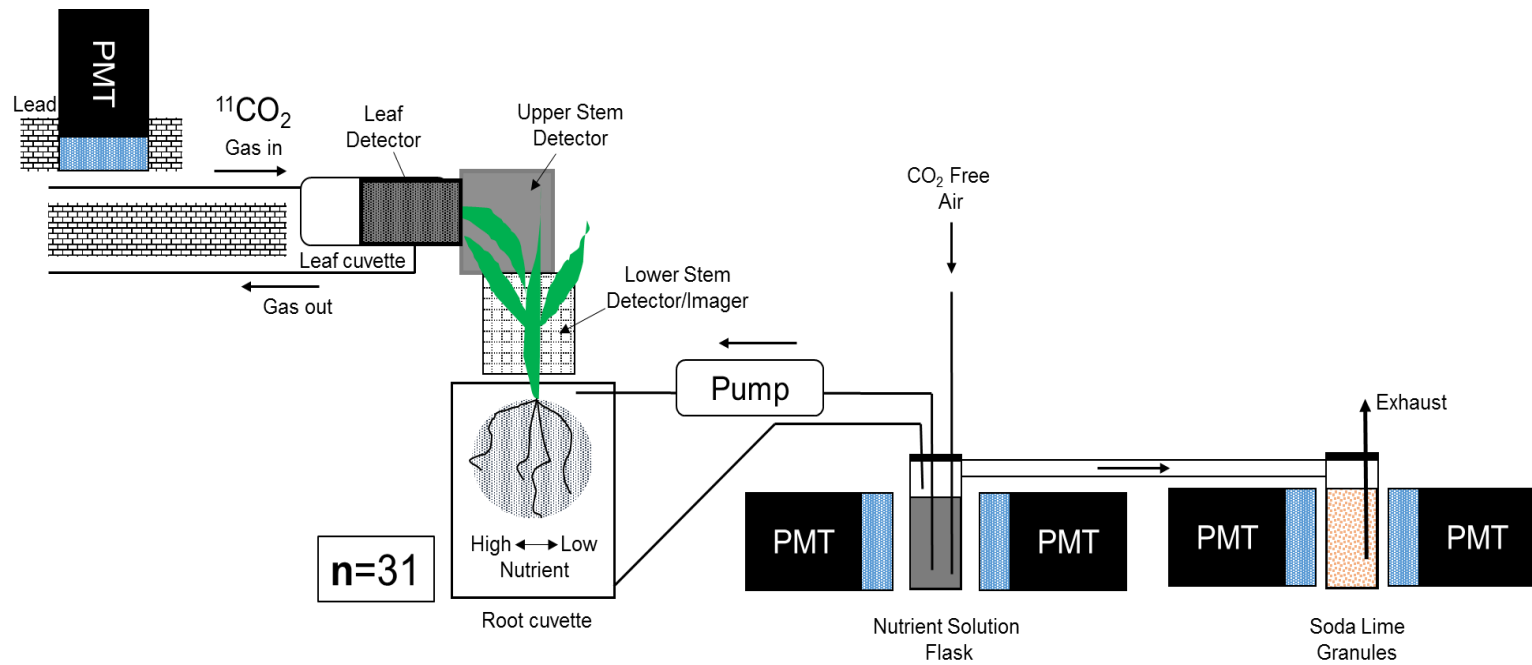


Figure 10. Diagram of the experimental setup used to measure whole plant carbon allocation dynamics, including root exudation and respiration. This figure was taken from [Kis08]. The system was designed for tracking carbon-11 in grasses and other small plants.

Accumulation of ^{11}C in a given region was measured by detecting gamma rays emitted following positron annihilation. In the most recent set of measurements (2009 only) the co-linear gamma rays were detected in coincidence using bismuth germanium oxide (BGO) detectors in the FOV of all parts of the plant except the uptake leaf. To handle the high gamma-ray flux emitted from the leaf, we used detectors with Prelude@420 ($\text{Lu}_{1.8}\text{Y}_2\text{SiO}_5:\text{Ce}$) crystals made by Saint-Gobain, Inc. The Prelude crystal (decay constant = 41 ns) is about 7 times faster than BGO (decay constant = 300 ns). For each experiment, several detectors were used to track the flow of carbohydrates inside the plant. The relative efficiency of each detector pair for 511 keV gamma rays was determined to allow comparisons among regions.

Barley plants were grown hydroponically with two nutrient concentration conditions (High = $\frac{1}{2}$ strength "Hoagland" and Low = $\frac{1}{16}$ strength "Hoagland"). In addition, because the response of the plants to nutrient availability might depend on the atmospheric CO_2 concentration, a batch of plants under each nutrient condition was grown with both ambient [CO_2] level (350 ppm) and elevated [CO_2] (700 ppm). The measurements on each plant were carried out at the same [CO_2] level at which the plant was grown. We tested each plant for real-time responses by abruptly changing in the nutrient concentrations by switching between the high to low nutrients and vice versa. The root exudate is determined by continuously circulating the hydroponic solution of each plant cuvette in a closed loop. The flowing water rinses off the carbohydrates that are loosely lying on the root surface or in the vicinity of the root, rhizosphere, and passes the solution in front of a gamma-ray detector. The $^{11}\text{CO}_2$ gas respired by the roots is separated from the liquid by bubbling nitrogen gas through the reservoir used to

measure the activity in the root solution due to exudation, as shown in the bottom left of Fig. 10. The nitrogen gas is filtered through a soda-lime trap and exhausted. The soda-lime trap absorbs the CO₂ gas in the granules and is monitored using a CsF detector.

Two sets of measurements of the sugar transport and allocations were made on each plant. The first was made under the nutrient condition for which the plant was grown. For the second measurement, the nutrient solution was switched to the alternate condition. The second set of measurements started about 30 minutes after the first measurement ended. Measurements were performed on 31 barley plants in the morning and afternoon under the same conditions of temperature, humidity and light intensity. All plants were less than 21 days old at the time of the measurements; the age is taken to be the time since germination. The duration of each measurement was approximately three hours. Data analysis methods and results will be discussed in the next two sections.

4.3 Data Analysis

Modeling the physiological processes in plants can be used to identify cause-and-effect patterns in measurements of the type of feedback system driving the given response. Analyzed data are required to validate model predictions and to determine the values of model parameters. Models are essential for obtaining reliable interpretations of the behaviors of the feedback systems in plants that regulate resource allocation and utilization. Recent studies suggest that feedback systems in plants are driven by both active (chemical-signaling) [Din12] and passive (pressure, water availability, and temperature) mechanisms [Sle10]. Our real-time data for the photosynthesis rate and translocation and allocation of newly synthesized carbohydrates in barley plants can be

interpreted using a purely statistical approach that makes no assumptions about the biological process [Min03]. Results from a statistical analysis method can be used to create a model that adheres to the assumed physiology of the process being studied. This model is described in more detail in the next section.

4.3.1 Input-Output Model

The input-output (transfer function) model is a common statistical tool used for radiotracer profile analysis. This model enables the evaluation and comparison of measured radiotracer profiles. Radiotracer profiles are the graphical presentation of the radiotracer accumulation as a function of time in a specific plant organ as shown in Fig. 11 (left). In the transfer function model, there are no assumptions about the mechanisms involved in the substance transport processes. Measured data are the primary source for deriving interpretations of radiotracer flow via the transfer function.

The transfer function provides a mathematical representation of the transport and allocation process, and also describes the change in shape between the input and resulting output tracer profile of a particular measurement [Min03]. Fig. 11(A) depicts how measurement of the amount of radiotracer in region A and the total radiotracer in regions B and C can provide information about the fraction of the labeled substance exported from region A [Kis08]. In these activity plots $t = 0$ is when the loop is loaded with the $^{11}\text{CO}_2$ tagged air.

Processes that are of interest include sugar synthesis during photosynthesis, phloem loading and transport in the leaf, stem and root tissue. Also, root exudation and respiration are important for understanding the whole-plant priorities involved in its response to a change in the environment. The discrete time binning (one minute wide

bins) of our data allow us to apply a linear difference equation to model the radiotracer accumulation and transport within the plant. A first order linear difference equation is used to model the amount of radiotracer in a given region at time bin k , as shown by equation 3.1. This model has three free parameters (a_1 , b_j and j) that are adjusted to fit the data, y and u . The j parameter is a characteristic delay time for transport between the two regions being studied, e.g., A and (B+C).

$$y_k = -a_1 y_{k-1} + b_j u_{k-j} \quad (4.1)$$

Input-output analysis of a measurement yields the fraction of radiotracer exported from a particular region, commonly referred to as the system (region) gain [Min80]. This was applied to our data to determine the total radiotracer accumulated in each plant organ. The variables y_k , k , u_k and j , are the output tracer accumulation, time step, input tracer accumulation, and characteristic time delay for each organ, respectively.

$$\text{Gain} = \frac{b_j}{1+a_1} \quad (4.2)$$

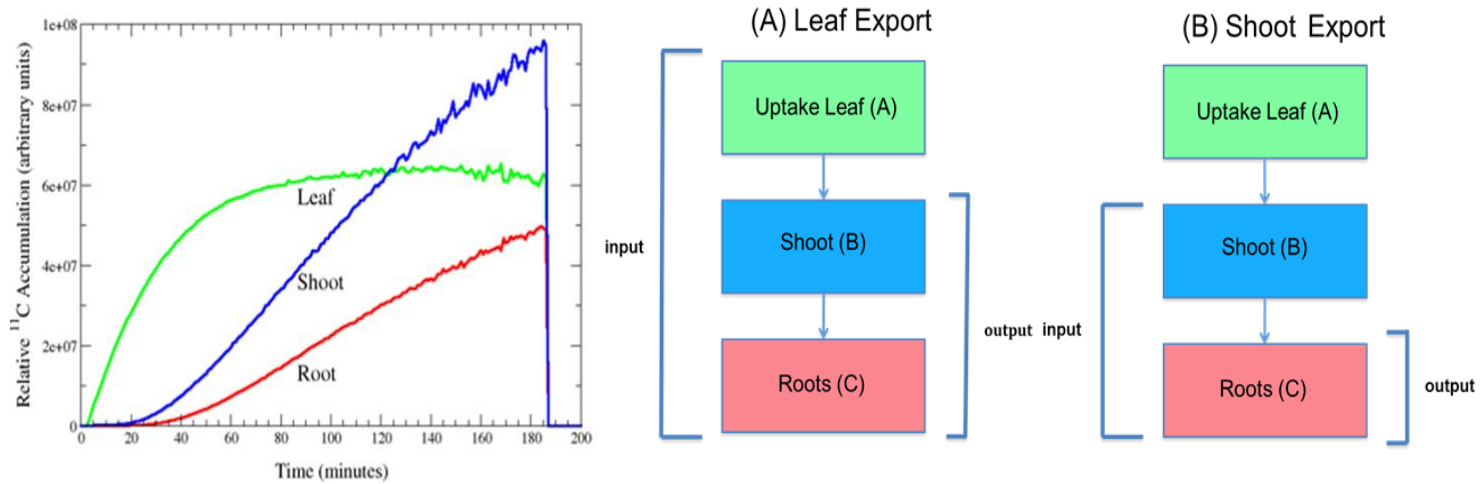


Figure 11. Example of radiotracer profiles for relative accumulation of ^{11}C -tagged carbohydrates in barley seedling. (Left panel) The ^{11}C activity data are plotted as a function time. These data are corrected for background, relative detection efficiency and half-life. (Right panel) Measurement regions used in input-output analysis. (A) Diagram A depicts parameters necessary for investigating the transport of radiotracers from the photosynthetic region of the leaf. (B) Parameters defined for investigating radiotracer flow from the shoot to the roots.

The system gain is computed using equation 4.2. The gain is defined as the amount of radiotracer exported from a given region. As stated above, the parameters a_1 and b_j are varied to find the best fit to the data. Fig. 12(b) provides an example of a derived model fit to output data. The value of the delay parameter j depends on the physical attributes of the plant and the regions through which the substance is transported. The values of j used in our analysis of the barley data ranged from about 15 to 100. An example of the input and output profiles as well as the fit to the data are shown in Fig.12.

An iterative data fitting procedure was used. The iteration started by setting the value of j to the best guess based on experience with fitting input-output data. Then a chi-square minimization fit was performed on the data with the function given in equation 4.1 using a_1 and b_j as the free parameters in the search. Next the value of j was stepped and another chi-square minimization fit was performed. This process was repeated until the smallest value of chi-square was obtained. The statistical uncertainty in the gain was computed as follows:

$$\Delta G^2 = \left(\frac{\partial G}{\partial a_1}\right)^2 \Delta a_1^2 + \left(\frac{\partial G}{\partial b_j}\right)^2 \Delta b_j^2 \quad (4.3)$$

In all cases the statistical uncertainty in the gain for each set of measurements was substantially less than 1% and was neglected in the propagation of the uncertainty. The error bars reported in the tables and shown in the figures in this section are the standard errors, which are computed using the variance from the mean value of the quantities

obtained for each data set.

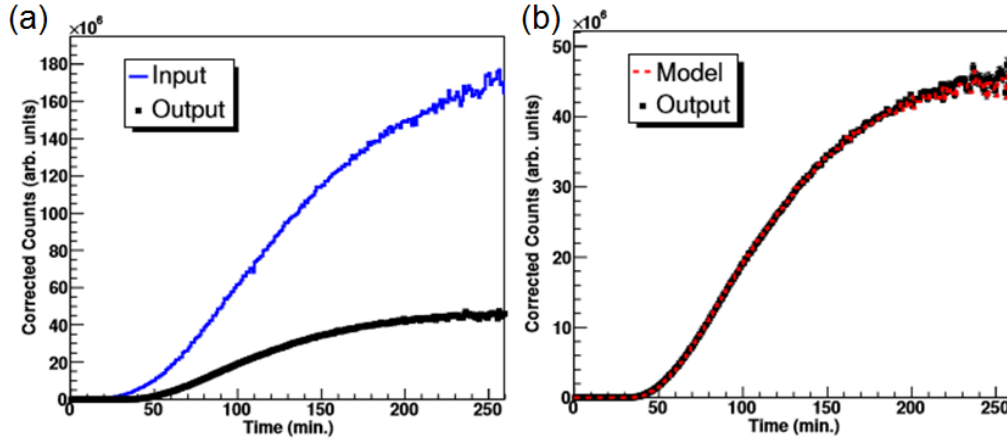


Figure 12. (a) Example of radiotracer input and output profiles for relative accumulation of ^{11}C -tagged carbohydrates in barley seedling, (b) example of a derived model fit to output data.

The following relationships were used to compute the quantities reported in this section. The leaf export is given by:

$$LE = G_{LE} = \frac{b_j}{1+a_1} \quad (4.4)$$

In this equation the G_{LE} is the gain for export from the leaf into the remainder of the plant, i.e., $(A) \rightarrow (B+C)$ as shown in Fig. 11(a). The shoot export is given by

$$SE = G_{SE} = \frac{b_j}{1+a_1} \quad (4.5)$$

In this equation the G_{SE} is the gain for export from the shoot into the root, i.e., $(B+C) \rightarrow (C)$ as shown in Fig. 11(b). The below ground sugar allocation is computed as

$$BG = LE * SE \quad (4.6)$$

To compute the root exudation and respiration two additional regions are considered, region D is the activity for the soluble carbohydrates and region E is the CO_2 expelled

from the hydroponic liquid and absorbed in the soda-lime trap. Plots of the time dependence of the activity in regions D and E are shown in Fig. 13.

The root exudation and respiration are computed as follows:

$$RE = G_{RE} = \frac{b_j}{1+a_1} \quad (4.7)$$

$$RR = G_{RR} = \frac{b_j}{1+a_1} \quad (4.8)$$

In this equation, the G_{RE} and G_{RR} are the gains for export from the root into the hydroponic solution of soluble carbohydrates and CO_2 gas, respectively. The RE and RR gains are obtained by fitting the data for the following regions, (C)→(D) and (C)→(E), respectively.

The standard errors (STEs) were computed as follows:

$$STE = \frac{\sqrt{\frac{\sum(x_i - x_{avg})^2}{(n-1)}}}{\sqrt{n}} = \frac{S.D.}{\sqrt{n}} \quad (4.9)$$

The x_i is the gain for a particular measurements, x_{avg} is the mean gain for each treatment condition (e.g., nutrient level, $[CO_2]$, time of day), n is the number of measurements, $S.D.$ is the standard deviation. The standard error may be interpreted as the biological variation of the responses of individual plants in the batch. We use the 95% confidence interval as the standard for interpreting whether a measurement indicates a significant effect. For sample sizes less than 10, the threshold for an effect is 2.5 STEs, and for larger sample sizes the effect threshold is 2.0 STEs.

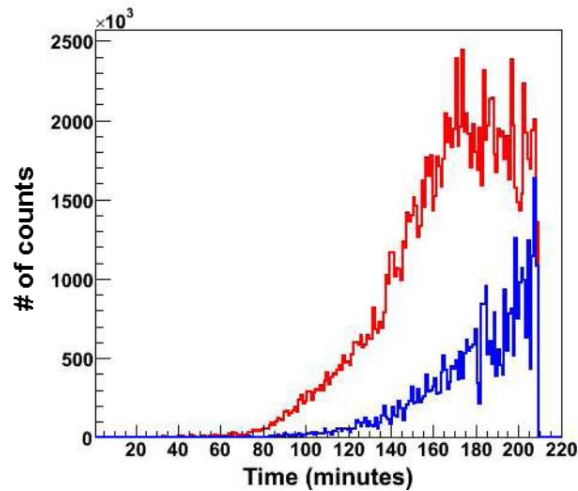


Figure 13. Plots of the time dependence of the activity in regions D (root exudation-red line) and E (root respiration-blue line), (from [Kis08]).

4.4 Results

4.4.1 Effects of Atmospheric CO₂ Concentration

Our data indicate that the fraction of ¹¹C-tagged carbohydrates exported from the barley leaf is significantly affected by the time of day when averaged over the atmospheric CO₂ concentration and nutrient availability settings used in this study. The Barley plants measured in the AM exported (57 ± 3)% of recently fixed carbon from the leaf, while those measured in the PM exported (48 ± 3)% as shown in Fig. 14. The difference between the morning and afternoon leaf export is 9.0% ± 4.2%, which is a difference of 2.1 standard errors (STEs). Such diurnal reduction in export has previously been observed in soybean leaves [Ker85] but contrast with cotton [Hen86].

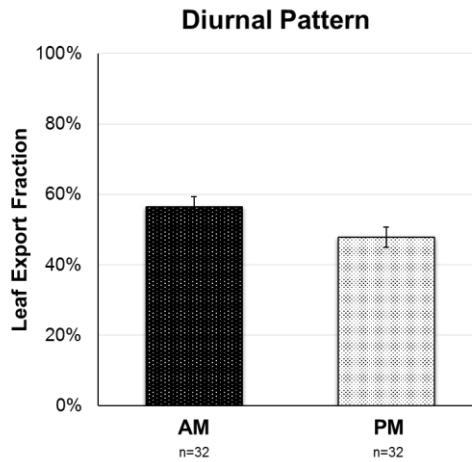


Figure 14. Effect of measurement time of day on the leaf export fraction. The values shown are the means \pm the standard error of the mean; the number of measurements averaged is $n = 32$ for both AM and PM.

The data indicate that atmospheric CO_2 concentration significantly altered the fraction of recently synthesized carbohydrates that are exported from the leaf and the shoot in barley, as shown in Table 4; Fig. 15. The difference in the carbohydrates exported from the leaf under elevated and ambient $[\text{CO}_2]$ is 2.4 STEs, $\Delta\text{LE} = 10\% \pm 4.2\%$. The results are similar for shoot export, $\Delta\text{SE} = 14\% \pm 5.8\%$, which is 2.4 STEs. These data were averaged over the two nutrient availability levels used in this study, i.e., high and low.

The data indicate that the carbohydrate fraction exported from the shoot and allocated belowground is influenced by the atmospheric CO_2 levels ($[\text{CO}_2]$) as depicted in Fig. 15. The below ground allocation of the newly fixed carbohydrates was about 4 STEs larger for ambient $[\text{CO}_2]$ than elevated levels, i.e., $\Delta\text{BG} = 16\% \pm 4.1\%$. These data are also averaged over both nutrient conditions.

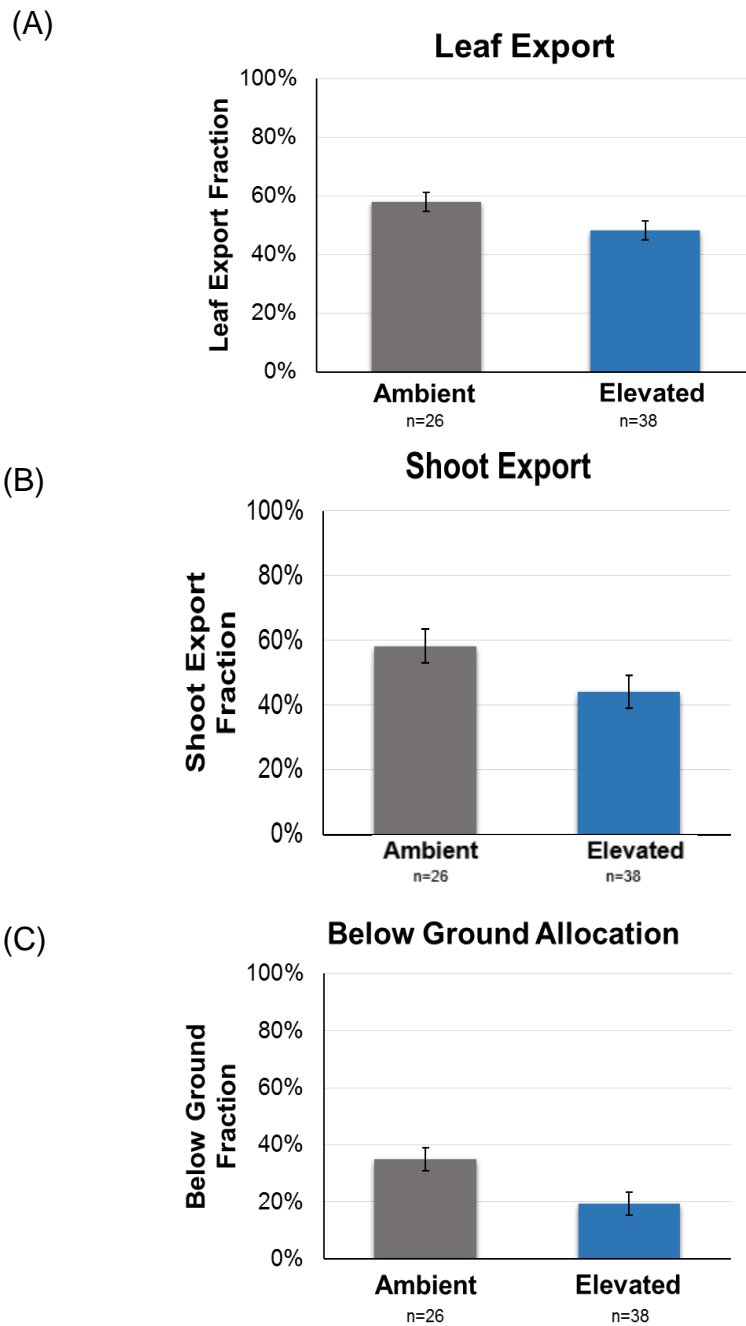


Figure 15. Effects of atmospheric CO₂ levels on carbohydrate allocation and transport in barley. The quantities plotted are the percent of the substance exported from each region. These data are averaged over both nutrient levels used in this study. The values shown are the mean \pm the standard error of the mean.

Table 4. Effects of atmospheric CO₂ concentration on carbohydrate allocation in barley.

	Barley Ambient CO₂	Barley Elevated CO₂
Leaf Export Fraction	0.58 ± 0.03 (n = 26/13)	0.48 ± 0.03 (n = 38/19)
Shoot Export Fraction	0.58 ± 0.05 (n = 26/13)	0.44 ± 0.03 (n = 38/19)
Belowground Fraction	0.35 ± 0.04 (n = 26/13)	0.19 ± 0.01 (n = 38/19)

The values are the fraction of the substance exported from each region. These data are averaged over both nutrient levels used in this study. The values presented are the mean ± the standard error of the mean. The number of measurements and number of different plants used are given in the parenthesis below the mean values, i.e., (n = # measurements/ # of different plants).

In our experiments, CO₂ concentration played no significant role in the relative portion of carbon released from the root as either exudate or respiration, as listed in Table 5.

Table 5. Effects of atmospheric CO₂ concentration on root exudation and respiration.

	Barley Ambient CO₂	Barley Elevated CO₂
Percent Root Exudation	1.98 ± 0.20 (n = 26/13)	2.03 ± 0.31 (n = 38/19)
Percent Root Respiration	1.21 ± 0.15 (n = 26/13)	0.99 ± 0.26 (n = 38/19)

Values shown are the mean ± the standard error of the mean. The number of measurements and number of different plants used are given in the parenthesis below the mean values, i.e., (n = # measurements/ # of different plants).

4.4.2 Effects of Nutrient Treatment

Short-term changes in nutrient availability had a significant effect on below ground allocation of carbohydrates. For barley grown in ambient [CO₂], plants grown in high nutrient solution (1/2 strength Hoagland's) and switched to the low nutrient level

(1/16 strength Hoagland's) resulted in a $\Delta BG = (31 \pm 9)\%$ difference, 3.4 STEs, in the below ground allocation. For the elevated $[CO_2]$ condition, the plants grown in high nutrient solution and switched to the low nutrient concentration resulted in $\Delta BG = (37 \pm 14)\%$ difference in the below ground allocation, which is 2.6 STEs. Switching the nutrient solution from low to high had no significant effect on the magnitude of change in carbohydrates allocated belowground regardless of the $[CO_2]$ levels.

Root exudation in barley did not significantly change when switching the nutrient solution in any direction for either $[CO_2]$ condition, as shown in Table 6. We found a significant difference in the root respiration due to abruptly changing the nutrient availability from the high to low level for plants grown and measured in the ambient $[CO_2]$ condition, $\Delta RR = (52 \pm 14)\%$, which is 5.8 STEs. No significant effect was observed for nutrient changes in any of the other conditions, as shown in Table 6.

Table 6. Effects of abrupt changes in the nutrient availability on belowground allocation, root exudation, and respiration

	Barley Ambient CO_2		Barley Elevated CO_2	
	L → H	H → L	L → H	H → L
% Change in Belowground	0.004 ± 0.24 (n = 8/8)	-0.31 ± 0.09 (n = 7/7)	0.07 ± 0.17 (n = 8/8)	-0.37 ± 0.14 (n = 4/4)
% Change in Exudation	0.08 ± 0.29 (n = 8/8)	0.04 ± 0.19 (n = 7/7)	0.27 ± 0.20 (n = 8/8)	-0.13 ± 0.13 (n = 4/4)
% Change in Respiration	0.81 ± 0.39 (n = 8/8)	-0.52 ± 0.09 (n = 7/7)	-0.20 ± 0.17 (n = 8/8)	-0.41 ± 0.22 (n = 4/4)

The values shown are the mean \pm the standard error of the mean. The number of measurements and number of different plants used are given in the parenthesis below the mean values, i.e., (n = # measurements/ # of different plants).

The fraction of newly synthesized carbohydrates allocated belowground was greater in the higher concentration nutrient solution for both atmospheric CO₂ concentration levels, as shown in Table 6. Switching H→L for both elevated and ambient [CO₂] decreases the below ground allocation, and switching L→H induces no significant change in carbohydrates allocated belowground.

4.4.3 Variance in Export Fractions

The variability of the responses of plants within a species to sudden fluctuations in external environmental conditions could provide insight about how a species might survive short periods in limiting conditions. For instance, under conditions when some plants survive while others do not. A goal of this work is to examine the variations in the responses of barley plants during their exponential growth phase when grown in drastically different atmospheric [CO₂]. This study explores the issue through the perspective of allocation of newly synthesized carbohydrates. In this approach, the variance in the distribution of the sugar allocations is interpreted as being due to the biological variation of individual plants. This analysis includes distributions measured under ambient and elevated [CO₂] conditions for leaf export, shoot export, below ground allocation, root exudation and root respiration.

Histograms of the measured export and allocation distributions are plotted in Figures 16 and 17. The leaf export distributions for ambient and elevated [CO₂] seem to have opposing trends. The mean value of leaf export under ambient [CO₂] measurements display a peak at 72%, while elevated [CO₂] measurements display a peak value at 43%. However, both atmospheric conditions measure export values

ranging from about 40% to 85%. An interesting feature is that both [CO₂] conditions produce low probabilities for leaf export percentages around 60%.

The distributions for the shoot export are similar to the leaf export histogram, except that both environmental [CO₂] conditions approach a large number of replants at 72%. The shoot export range is approximately 30% to 85%.

Histograms for the distributions for below ground allocations are plotted for the two [CO₂] conditions in Fig. 16. The dispersion in the below ground allocations is substantially larger for the ambient [CO₂] condition than for elevated [CO₂]. On average, a larger fraction of the newly fixed carbohydrates is allocated to underground sinks in the ambient [CO₂] condition compared to the elevated [CO₂].

The distributions for root exudation and respiration are plotted in Fig. 17. Two notable features of the distributions both quantities are: (1) for ambient [CO₂], the distributions are highly localized with values less than about 5%, (2) for elevated [CO₂], the distributions have a cluster of values less than 2% and then a scatter of points up to about 8%.

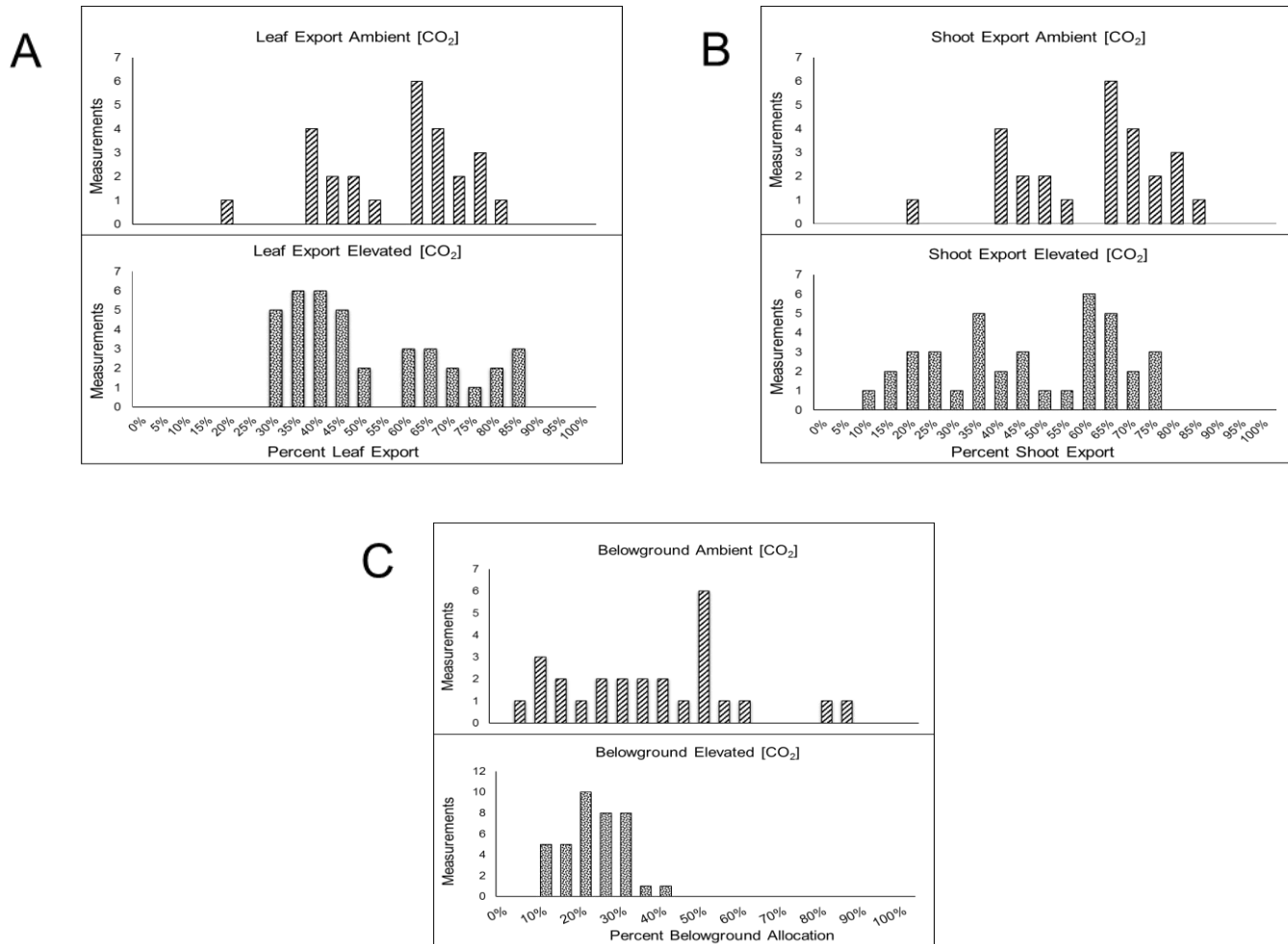


Figure 16. Variability in leaf export (A), shoot export (B), and belowground allocation (C) fractions.

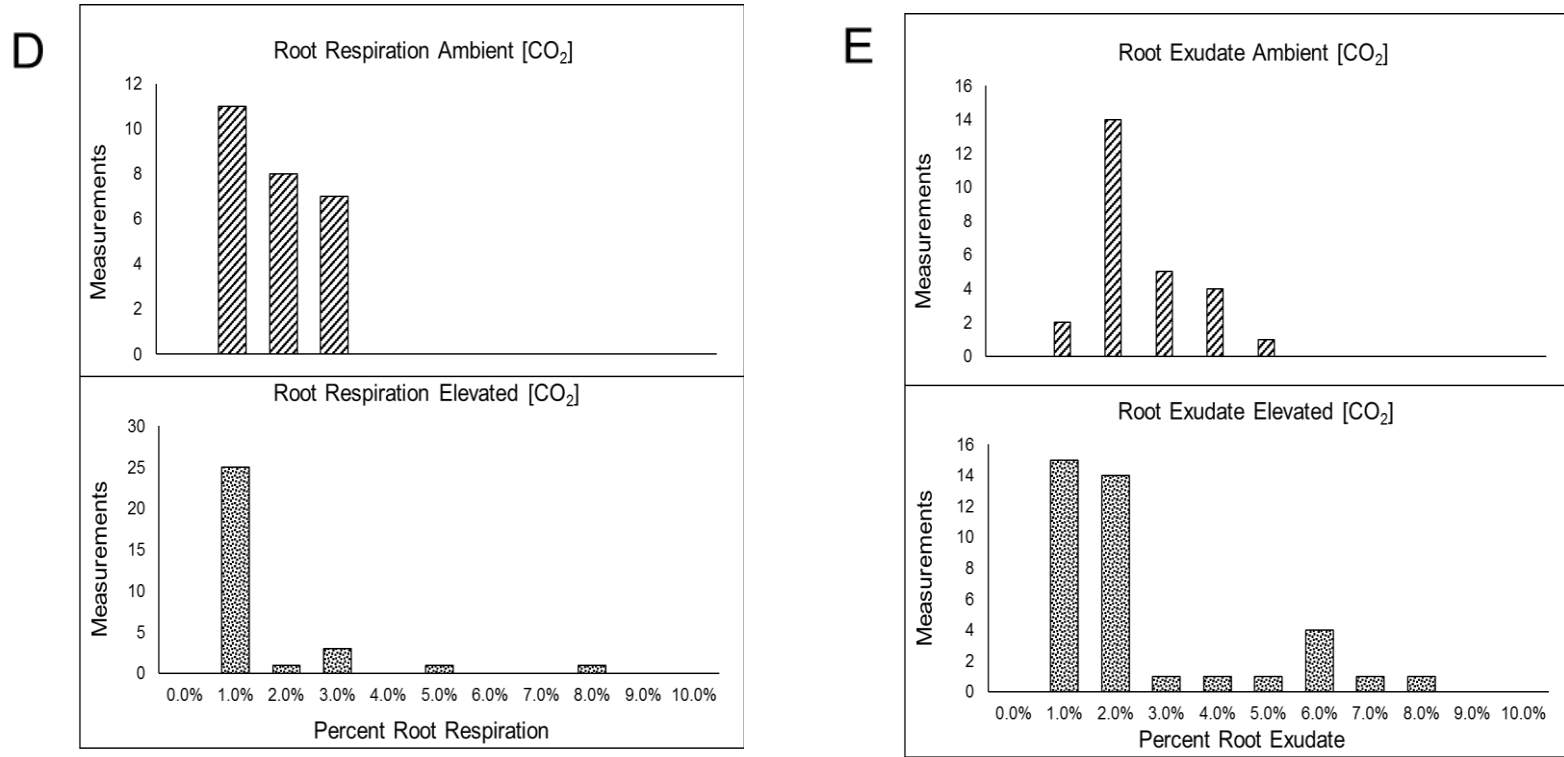


Figure 17. Variability in root respiration (D) and root exudation (E) export fractions.

4.4.4 Interpretations of Fractional Allocation using Measured Photosynthetic Rates

Measurements of the reduction in $[\text{CO}_2]$ in the closed-loop system using the IRGA and MFC provided a direct calculation of photosynthetic rate (Ps) in barley. Dispersion in the distribution of the Ps is interpreted as being due to biological variation of individual plants within the batch. Histograms of the measured Ps distributions are plotted in Fig. 18. The Ps distributions for the ambient condition range between 2 and 30 $\mu\text{mol}/\text{m}^2/\text{s}$. This result is in contrast to the Ps distribution for the elevated $[\text{CO}_2]$ condition, where the majority of Ps measurements were greater than 30 $\mu\text{mol}/\text{m}^2/\text{s}$ up to a maximum of approximately 70 $\mu\text{mol}/\text{m}^2/\text{s}$. There were a few cases of low Ps measurements for the elevated $[\text{CO}_2]$ condition that may be attributed to the biological variability in the barley species.

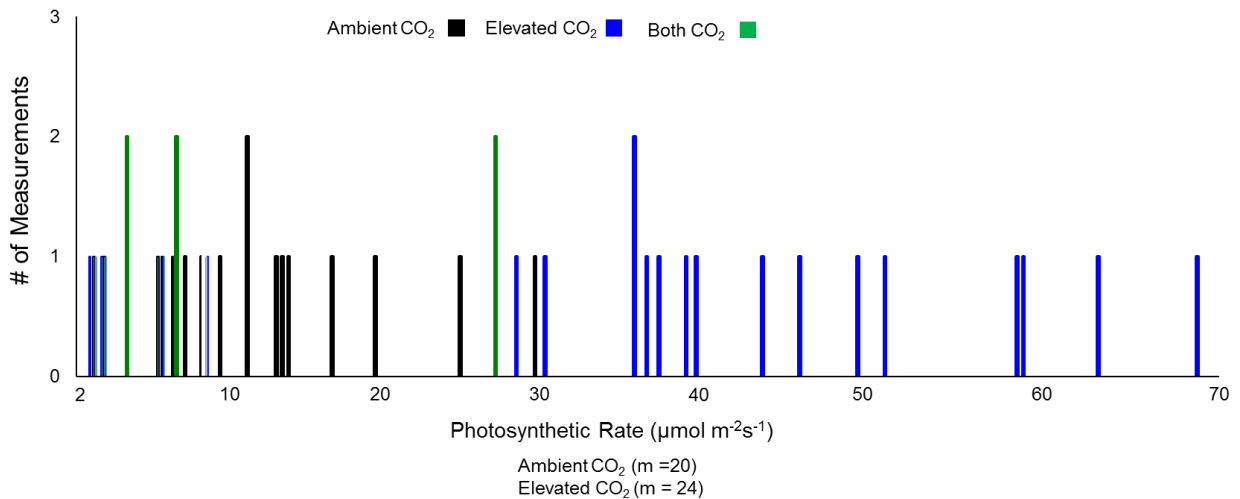


Figure 18. Variance in the measured photosynthetic rate for barley grown in either ambient or elevated $[\text{CO}_2]$.

The data indicate that photosynthetic rate is influenced strongly by atmospheric CO₂ levels, as shown in Fig. 19. The average Ps under ambient and elevated [CO₂] were measured to be $7.45 \pm 0.97 \mu\text{mol}/\text{m}^2/\text{s}$ and $23.41 \pm 3.54 \mu\text{mol}/\text{m}^2/\text{s}$, respectively. The measured photosynthetic rate was approximately 4 STEs larger for elevated [CO₂] than ambient levels, i.e., $\Delta\text{Ps} \approx 16 \pm 4.3\%$. These data are also averaged over both nutrient conditions.

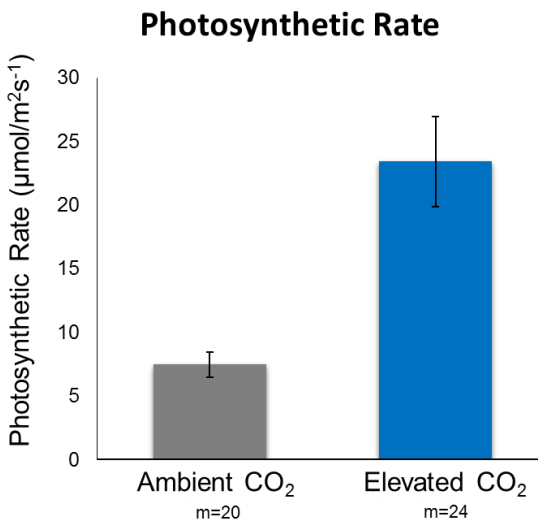


Figure 19. Average photosynthetic rate for barley grown in either ambient or elevated [CO₂].

Photosynthetic rate (Ps) measurements were also used to compare barley grown in either the low or high nutrient condition. Results indicate that Ps is not impacted by the nutrient solution concentration used in this experiment for either of the atmospheric [CO₂] conditions, as listed in Table 7.

Table 7. Average photosynthetic rates and nutrient breakdown under ambient and elevated [CO₂].

Analysis	Ambient CO₂	Elevated CO₂
Average Ps	7.45 ± 0.97 (m = 20)	23.41 ± 3.54 (m = 24)
Low Nutrient Ps	6.42 ± 1.04 (m = 11)	22.30 ± 5.39 (m = 13)
High Nutrient Ps	8.72 ± 1.73 (m = 9)	24.74 ± 5.29 (m = 11)
Analysis	Ambient CO₂	Elevated CO₂
Average Ps	7.45 ± 0.97 (m = 20)	23.41 ± 3.54 (m = 24)
Low Nutrient Ps	6.42 ± 1.04 (m = 11)	22.30 ± 5.39 (m = 13)
High Nutrient Ps	8.72 ± 1.73 (m = 9)	24.74 ± 5.29 (m = 11)

The partitioning results for newly-fixed carbohydrates were presented in a previous section (4.4.1). Calculated photosynthetic rates can provide additional information regarding the absolute quantity of carbohydrates (in terms of $\mu\text{mol}/\text{m}^2/\text{s}$) allocated to various regions of barley. Using the average Ps values given in Table 7, comparisons can be made for each region regarding the absolute Ps allocated. With this information, the ambient [CO₂] and elevated [CO₂] conditions can be compared for further insight on the impact of atmospheric [CO₂] levels on carbohydrate partitioning.

Values in Table 8, are used to calculate the difference in absolute carbon translocated or exported, based on the photosynthetic rate, under elevated and ambient [CO₂] is 4 STEs, i.e., ΔPs leaf allocation $\approx 9 \pm 2.0$. The results are similar for belowground carbohydrate allocation, i.e., ΔPs below ground allocation $\approx 2.5 \pm 0.91$,

which is 2.7 STEs. These data were averaged over the two nutrient availability levels used in this study, i.e., high and low nutrient.

Table 8. Relative vs. absolute amount of carbohydrates allocated under ambient and elevated [CO₂].

Analysis	Relative Allocation under Ambient [CO₂]	Allocation of Photosynthetic rate (μmol/m²/s) under Ambient [CO₂]	Relative Allocation under Elevated [CO₂]	Allocation of Photosynthetic rate (μmol/m²/s) under Elevated [CO₂]
Leaf Allocation	0.42 ± 0.03 (m = 26)	3.13 ± 0.44 (m=20)	0.52 ± 0.03 (m= 38)	12.11 ± 1.98 (m=24)
Below Ground Allocation	0.35 ± 0.04 (m = 26)	2.52 ± 0.44 (m=20)	0.19 ± 0.01 (m = 38)	4.97 ± 0.80 (m=24)
Root Exudation	0.020 ± 0.002 (m = 26)	0.050 ± 0.008 (m=20)	0.020 ± 0.003 (m = 26)	0.101 ± 0.018 (m=24)

4.5 Findings and Discussion

This chapter provided a description of the experiment used to study the effects of elevated [CO₂] and nutrient availability on the allocation of carbohydrates in barley plants during their exponential growth phase. The implied hypothesis, based on previous studies [Dij13], is that plants under low nutrient conditions would (1) allocate a greater fraction of carbohydrates to below ground structures for either root growth for soil foraging, or (2) increase the fraction of root exudate due to the symbiotic relationship between the root microbes and the plant [Dak02]. The results and findings from this study are summarized below.

- We have performed the most extensive measurements of ¹¹C tracking in a plant species in terms of the number of plants in the sample pool and the variety of quantities measured. Measurements were performed on 31 plants over about a 10-year period. The study was conducted on barley plants in the exponential growth phase.
- We found a significant diurnal pattern in the leaf export of newly fixed carbohydrates. A larger fraction of carbohydrates is exported from the leaf in the morning than afternoon.
- Sensitivity tests to atmospheric CO₂ concentration:
 - A significant difference was observed in the leaf export for plants grown and measured at ambient atmospheric CO₂ concentrations ([CO₂] = 350 ppm) versus the measurements at the elevated [CO₂] level (700 ppm).
 - A significantly larger fraction of the newly synthesized carbohydrates is allocated to below ground sinks under ambient [CO₂] relative to the

elevated [CO₂] condition. Barley plants grown in the ambient [CO₂] condition tend to export a larger fraction of its newly synthesized carbohydrates than those grown at the elevated [CO₂] level.

- We found no sensitivity in the root exudation or respiration to the [CO₂] level.
- Sensitivity tests to nutrient availability
 - For both ambient and elevated [CO₂] levels, we found a significant decrease in the below ground allocation of carbohydrates when switching from high to low nutrient availability.
 - A significant decrease in root respiration was observed when switching from high to low nutrient availability under the ambient [CO₂] condition.
 - There was no observed sensitivity to the abrupt change of switching from the low to high concentration under either the ambient or elevated [CO₂].
 - No sensitivity to abrupt changes in the nutrient level was observed in the measured root exudation under both [CO₂] conditions.
- Distributions of plant responses in terms of sugar export fractions
 - In this work we measured the distribution of five quantities under the two [CO₂] levels. The quantities include: leaf export, shoot export, below ground allocation, root exudation and root respiration.
 - The distributions for leaf export measured at both [CO₂] seem to have low probabilities at approximately 60% export. In both cases, the export value ranged from about 40% to 85%.

- The variance in the distribution of the below ground sugar allocation is substantially less for elevated [CO₂] than for ambient [CO₂].

Analysis of measured data indicate that independent of the [CO₂] level, this species of barley has the tendency to allocate less carbohydrates below ground in response to a sudden decrease in the nutrient availability. This finding is contrary to expectations and suggests that the immediate priority of the plants requires holding carbohydrates in the above ground organs. Another interesting feature of the response to this controlled environment change is that the variance in the distribution of responses is very small compared to the dispersion in the responses to other environment changes.

The leaf-root subsystem demonstrates a nitrogen-carbon “currency” for resource (nitrogen) and carbohydrate exchange. Leaf organs may not give up carbohydrates for free, especially if resources are limited. They must maintain a sugar reserve to allow for plant survival [Reg09]. The decrease in the carbohydrate pool in the roots observed when switching from high to low nutrient concentrations could indicate a rapid signaling response associated with leaf and stem development [Wan16]. Also, this response might reflect that the barley leaf does not relinquish carbohydrates if resources are limited.

Also, our results do not support the hypothesis that a larger fraction of carbohydrates will be released in the hydroponic solution by the root under low nutrient availability [Dij13]. Nitrogen fixing of certain bacteria can form a lucrative plant-microbe symbiosis. Therefore, the expected response would be for an increase in carbohydrate allocation to the root during low nutrient conditions [Lem13] for root growth or root exudation. Root growth will allow the plant to search for nutrient pockets in the soil

[Dak02], while the release of soluble carbohydrates would increase soil microbe activity for increased nutrient uptake. Acquired data also revealed that on average the root exudation was insensitive to changes of about a factor of 10 in the nutrient availability. The lack of response in the average root exudation observed when switching between nutrient solutions could indicate an absence of microbes in the hydroponic solution.

Another effect observed was that there was a significant decrease in root respiration when switching from high to low nutrient availability in the ambient [CO₂] condition. This result is consistent with the observed decrease in the allocation of carbohydrates below ground when switching from high to low nutrient condition. That is, the instantaneous rate of metabolic processes in the root, which is the source of the respired CO₂, is likely directly related to the amount of fresh carbohydrates in the root. The results under the elevated [CO₂] condition are consistent with these findings but with a larger variance in the distribution of responses.

Despite the lower fraction of carbohydrates allocated to below ground structures under the ambient (0.35) vs. elevated (0.19) [CO₂] condition, on average, a larger absolute amount of carbohydrates were allocated to below ground sinks in the elevated [CO₂] condition due to the photosynthetic rate being 2.5 times larger. This value was averaged over both nutrient availabilities. This also indicates that the photosynthetic rate is not nitrogen limited using the nutrient concentrations in this study.

Chapter 5: Small Plant PET Imaging

Positron emission tomography (PET) imaging is a nuclear medicine technique suitable for *in vivo* quantitative measurements of functional processes within an organism. Since this thesis focuses on plant physiological function, we are primarily concerned with plant response to changes in their local environment. PET imaging allows us to quantify the distribution of radiotracer within plant tissue on a finer scale compared to conventional coincidence counting which uses whole detector blocks, as described in chapter 2. Limited angle PET imaging uses segmented scintillating crystals, such as BGO and LYSO, arranged parallel to the faces of opposite detector array(s).

The detection process is similar to coincidence counting, since gamma rays incident on opposite detectors are stored as a valid registered event. Photons generated by annihilation via positron-electron interactions can interact in opposite detectors along the line of origin. For PET imaging, more details of each event are recorded, including the time stamp, energy deposited, and the location of the interaction within the segmented crystal. This data can be used for event discrimination and image reconstruction purposes. The following section describes the PET system specifically designed for plant imaging featuring a modular nature of the standalone detector modules. The modules can be arranged in a geometry conducive to measuring radiotracer accumulation to accommodate for the size and shape of a particular plant species.

5.1 PET Imaging System

In this project, we implemented a custom PET imaging system developed by Thomas Jefferson National Accelerator Facility (Jefferson Lab), composed of individual standalone detector modules. Compact detector modules allow for flexible arrangement around plants being studied. Detector modules were assembled with segmented LYSO scintillating crystals coupled to position sensitive photomultiplier tubes, as shown in Fig. 20.

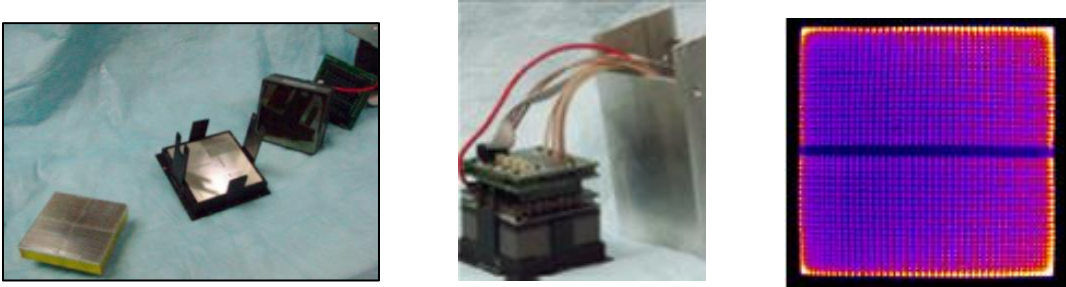


Figure 20. (Left) Photographs of LYSO array and (center) assembly with readout circuits and PSPMT. (Right) Flood image of LYSO:Ce array using a 0.25 mm^3 Na-22 point source. (from [Wei13]).

Individual components of the detector module are presented in Fig. 20(Left). Each scintillator array is 10 mm thick with 48×48 elements of LYSO:Ce with 1 mm pitch [Wei11]. Signal digitalizing occurs using Anger logic readout [Zha07] via a resistor matrix circuit board that implements a 16-channel analog to digital converter. The estimated FWHM of the imaging system was measured to be approximately 3 mm using a maximum likelihood expectation maximum (MLEM) reconstruction algorithm, a voxel size of 0.5 mm^3 and a 0.6 mm FWHM Gaussian smoothing filter [Wei13]. The low resolution of 3 mm is mostly due to positron range effects

5.2 Image Reconstruction

A coincidence event between pairs of detectors form a line of response (LOR) that connects the center of the two voxels and enables the integration of activity along that line. Limited angle PET image reconstruction is used to recover measured radiotracer distribution. An iterative algorithm, ML-EM, is used for more accurate reconstruction of the acquired data,

$$f_j^{new} = \frac{f_j^{old}}{\sum_i a_{ij}} \sum_j a_{ij} \frac{p_i}{\sum_j a_{ij} f_j^{old}} \quad (5.1)$$

where f_j^{new} is the next estimate of voxel j based on the preceding estimate f_j^{old} . The measured projections, p_i , are compared to the forward projection of the initial guess through division. The ratio of the projections is used to update the initial guess. This process repeats until the image estimate approaches the maximum likelihood solution [Ale06]. A flow chart that illustrates the general mechanism of the iterative algorithm is depicted in Fig. 21. Since our data are collected in list-mode format, measured p_i values are implicitly 1 for each line of response (LOR). The iterative algorithm allows for sequential updates to image voxel values through a series of predetermined steps designed to converge estimated voxel densities towards the true radioactivity density concentration.

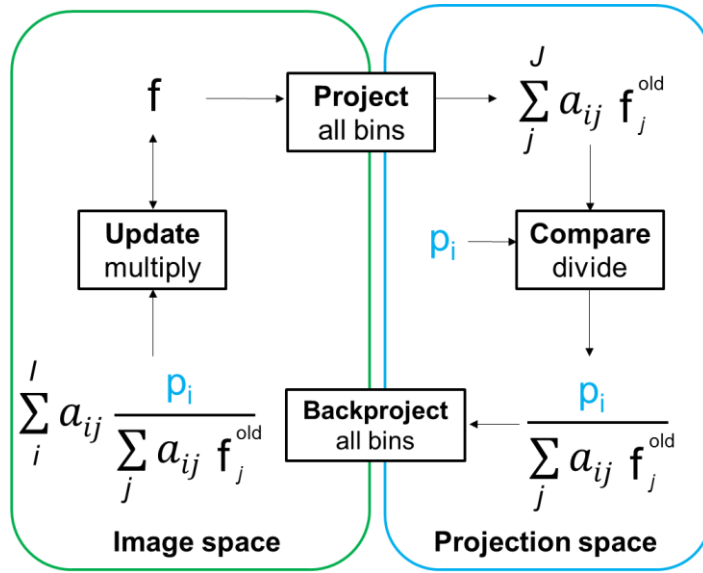


Figure 21. Schematic of general iterative reconstruction algorithm.

5.3 Positron Range Effect

The limiting factor to improvements in the spatial resolution of high resolution PET imaging systems is due mostly to positron range. However, in plant imaging, positron range limits quantitative accuracy due to count loss in thin structures of the plant. This effect leads to errors in radiotracer concentration estimation due to the unknown fraction of positrons escaping plant tissue before annihilation. In order to annihilate with a nearby electron, positrons must reach thermal energy, through a series of electronic collisions. Depending on the initial energy of the positron, a finite distance is traveled prior to the annihilation event producing photon pairs at a location outside the actual location of nuclear decay. Therefore, positron range leads to mispositioning of the LOR and leads to image degradation. Factors that influence positron range include initial positron energy and density of the surrounding material. Positrons emitted during radioactive decay can have energies ranging from zero to an arbitrary end-point energy,

which is determined by the Q-value associated with the decay [Che03]. Positron collisional energy loss through a given material can be determined using the Bethe-Bloch formula [Leo94] stated in equation 5.2. Energy loss is proportional to the density (ρ) and atomic number (Z) of the attenuating medium and inversely proportional to the velocity (β) of the incident positron.

$$-\frac{dE}{dx} = 2\pi N_a r_e^2 m_e c^2 \rho \frac{Z}{A} \frac{1}{\beta} \left[\ln \frac{\tau^2(\tau + 2)}{2\left(\frac{I}{m_e c^2}\right)^2} + F(\tau) - \delta - 2\frac{C}{Z} \right] \quad (5.2)$$

The variables for equation 5.2 are listed as follows:

- N_a = Avogadro's number
- r_e = classical electron radius
- m_e = electron mass
- c = speed of light in vacuum
- ρ = density of absorbing material
- Z = atomic number of absorbing material
- β = v/c of the incident positron
- τ = kinetic energy of the positron in units $m_e c^2$
- I = mean excitation potential of the material
- δ = density correction
- $F(\tau) = 2\ln 2 - \frac{\beta^2}{12} \left(23 + \frac{14}{(\tau+2)} + \frac{10}{(\tau+2)^2} + \frac{4}{(\tau-2)^3} \right)$
- C = shell correction
- $2\pi N_a r_e^2 m_e c^2 = 0.1535 \text{ MeV cm}^2/\text{g}$

According to equation 5.2, positron range is longest in materials with low density (ρ) and atomic number (Z). In small plant imaging, positron range is a formidable issue due to the thin nature of plant tissue and the relatively high average energy of positrons typically used in PET studies, as shown in Table 9.

Table 9. Common PET radioisotopes produced at TUNL and their mean range in water (from [Che03]).

Radioisotope	$t_{1/2}$ (min)	E_{mean} (MeV)	Mean Range in Water (mm)
^{11}C	20.4	0.326	1.1
^{13}N	9.96	0.432	1.5
^{18}F	109.8	0.202	0.6
^{15}O	2.03	0.696	2.5

For plants grown in a hydroponic solution, positrons emitted from ^{11}C tagged carbohydrates in the root cuvette water have a larger probability of annihilating within the FOV of the root detector. Water surrounding the roots limits the positron range to a few mm. This is not true for positrons emitted from leaf tissue surrounded by air. To mitigate the effect on positron range in these areas, plastic shielding can be used to convert positrons emitted from thin tissue. The deleterious effects of positron range on image quality is evident in Fig. 22 (center image).

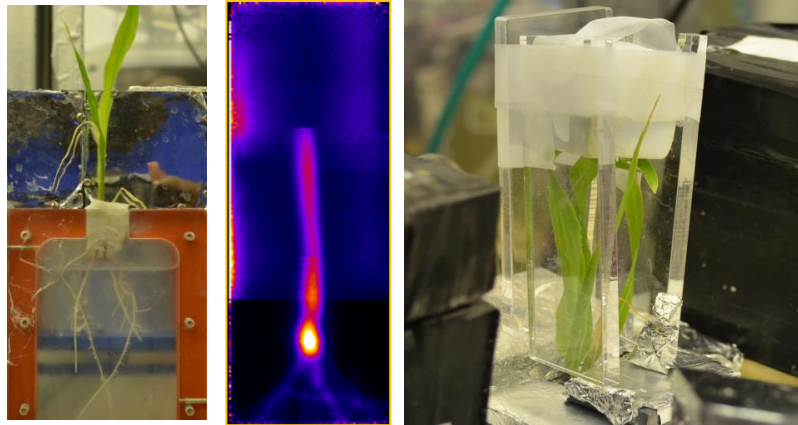


Figure 22. (Left) Picture of corn plant in hydroponic solution. (Center) Reconstructed image is shown with $^{11}\text{CO}_2$ as radiotracer. (Right) Photo of leaf volume surrounded by plastic converter.

5.4 PhytoPET Benchmark Validation

We performed benchmark studies data to confirm the effects of positron range for comparison with results from Geant4 simulations. Benchmark studies are used to compare experimental and simulated results since simulations implement imperfect models of a physical phenomenon. Experimental data can therefore validate the degree to which the simulation correctly models the real world system [Gre04].

5.4.1 Corn Seedling Experiment using $^{11}\text{CO}_2$

Our initial study involved the use of corn seedlings, approximately two weeks old, grown hydroponically in ambient atmospheric CO_2 conditions. The tracer, $^{11}\text{CO}_2$, produced at the Van de Graaff accelerator laboratory, was used to radiolabel recently synthesized carbohydrates in the corn leaf. The PhytoPET imaging system, discussed in section 5.1, allowed for limited angle PET imaging to estimate the spatial distribution of ^{11}C -tagged carbohydrates *in vivo*. This system allowed us to measure the effects of positron range on counting statistics in various segments of the plant. $^{11}\text{CO}_2$ gas was

introduced to a single leaf sealed inside a leaf cuvette, as depicted in Fig. 23 (left and center). PhytoPET detectors were positioned appropriately for planar imaging of radiotracer transport and accumulation inside a corn leaf, with blade thickness of 0.1 mm and midvein diameter of 0.4 mm.

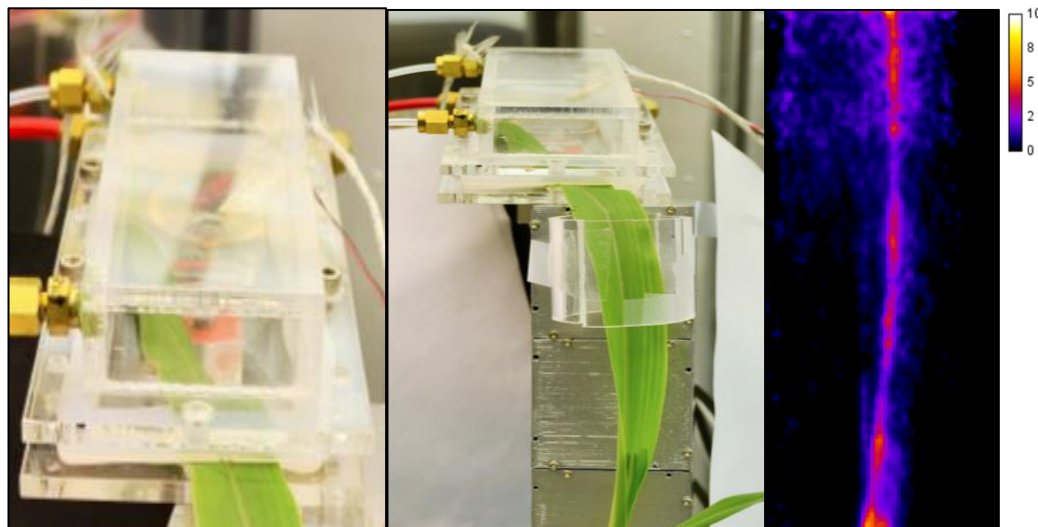


Figure 23. (Left) Photograph from radiotracer experiment conducted at TUNL of corn plant in sealed leaf cuvette, (center) 3 mm-thick acrylic positron converter around lower portion of the same corn leaf pictured on the left, and (right) 2D reconstructed image is shown.

Measured data indicate that using a plastic positron converter around the corn leaf increases the detection efficiency and led to higher counts for acrylic shielded (18,733) versus non-shielded (5,541) areas of the leaf using regions of interest (ROIs) with equal dimensions. The ImageJ image processing software was used to analyze the reconstructed image.

5.4.2 Plant Stem Phantom using $^{11}\text{C-NaOH}$

A plastic phantom was designed to model a typical corn-seedling stem. The majority of sugar transport occurs near the outer wall of the plant as shown in Fig. 24.

The phloem tissue bundle is responsible for the dissemination of the carbon-11 tagged carbohydrates throughout the plant. Positrons emitted from the stem would encounter less than 0.3 mm of plant tissue, significantly less than the average thickness, 1.1 mm, necessary for annihilation of ^{11}C positrons [Cal09].

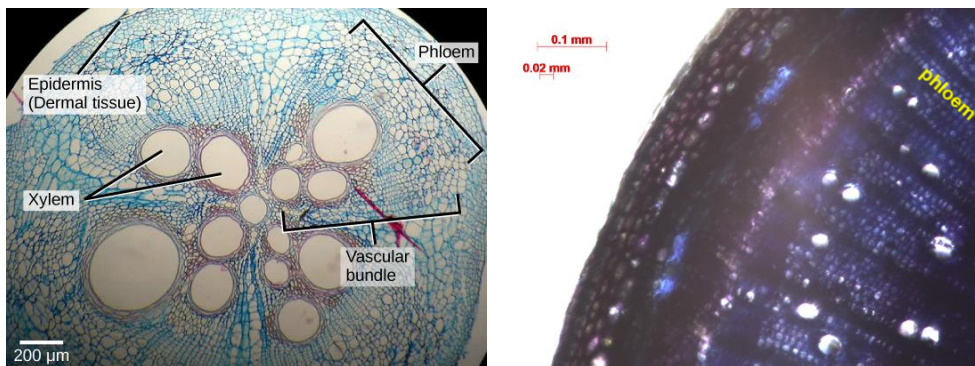


Figure 24. (Left) Picture of cross-section of a dicot (squash) stem showing the phloem and xylem (from [Bou06]). (Right) A magnification of the phloem tissue is shown with scaling (from [Buc00]).

A plant stem phantom was developed to study the impact of phloem location on positron range and counting statistics in small plant imaging. A sodium hydroxide (NaOH) aqueous solution was used to trap circulating $^{11}\text{CO}_2$ gas [Yoo13] produced using the Van de Graaff accelerator. The phantom, shown in Fig. 25, was constructed using a phenolic rod, representing the plant pith (density = 1.32 g/cm^3), inserted in the center of a plant-derived straw. The pith, or sometimes referred to as medulla, is composed of cells that store and transport nutrients throughout the plant. A plant-derived straw (0.1 mm thick) is used to represent the cell wall and to encase the ^{11}C liquid solution surrounding the phenolic rod. The outer diameters of the phenolic rod and plant-based straw are 3.0 mm and 5.0 mm, respectively. The total volume enclosed inside the

phantom is approximately 2.4 mL. The PhytoPET imaging system measured radiotracer activity in the phantom.

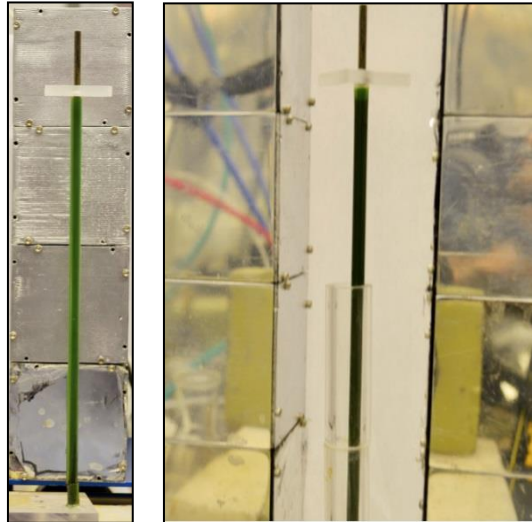


Figure 25. Photograph from radiotracer experiment conducted at TUNL of stem phantom positioned a distance 3-cm away from the PhytoPET imaging system. (Right) A 3 mm-thick acrylic positron converter is placed around the stem phantom for comparison purposes.

Two separate measurements were taken with the stem phantom, (1) without a plastic converter and (2) with a 3-mm thick acrylic positron converter covering only two-thirds of the plant phantom. The measurement without plastic confirmed that our procedures allowed for uniform distribution of radioactive solution within the phantom. Measured data show that using a plastic positron converter around the stem phantom increased the detection efficiency and led to higher counts for acrylic shielded (842) versus the non-shielded (532) volume. The ImageJ image processing software was used to analyze the reconstructed images.

5.5 Monte Carlo Modeling

Monte Carlo simulations, using Geant4 version 9.6, were performed for comparison purposes with benchmark data. Monte Carlo simulations are numerical calculations based on random variable sampling of probability density functions [And91]. These simulations allow us to create a computerized model of a theoretical or real system and perform studies not easily measurable experimentally. In this study, the Geant4 simulation toolkit is used to model carbon-11 tagged sugar uptake in a corn plant's leaf and stem. The PhytoPET detector modules are also modeled as LYSO crystal volumes with the same dimensions. Geant4 libraries contain the physics processes for radioactive decay and particle interaction probabilities [Ago03] and attempts to accurately describe the physics of particle interaction as it traverses through a given material. For PET simulations, positron trajectories and annihilation, Compton scattering, and photoelectric effect are important interactions that can be accessed from Geant4 libraries.

5.5.1 Geometry

The geometry function of Geant4 defines the physical attributes of objects used in the simulation. Once the geometry is defined, emitted particles can be tracked throughout the volume in the simulation space. The use of logical volumes allows the user to describe the shape, name, size and material composition of an object.

An example of how to define an LYSO detector volume is given below:

```
G4Material* LYSO = G4Material::GetMaterial("LYSO");  
  
G4Box* detector1 = new G4Box("detector1", 2.4*cm, 2.4*cm, 0.50*inch);  
  
G4LogicalVolume* detector1Logical = new  
G4LogicalVolume(detector1,LYSO,"detector1Logical");  
  
G4RotationMatrix *rm2 = new G4RotationMatrix;  
rm2->rotate(90*deg, G4ThreeVector(0,1,0));
```

Executable procedures for the Linux environment can be found in Appendix E.

5.5.2 Radioactive Sources

The positron source is defined in our Geant4 simulation using the G4GeneralParticleSource (GPS) library included in the Geant4 toolkit. GPS allows the user to explicitly specify spectral, spatial, and angular distribution of the primary source particles [GPS]. The simulation models positron interactions along its path starting from the source of emission to the various interaction volume(s). A random direction is assigned to each positron within the given source volume. The energy of each simulated positron is randomly assigned based on theoretical energy distributions for a particular radioisotope. GPS can generate positrons of a specific decay source (i.e. ¹¹C, ¹³N) using their characteristic energy spectra. Mono-energetic positron sources are also used for image quality comparison purposes.

Below is an example of a GPS script for a 0.5 mm point-like source:

```
/gps/pos/type Volume
/gps/pos/shape Sphere
/gps/particle e+
/gps/pos/centre 0.0 0.0 0.0 cm
/gps/pos/radius 0.025 cm
/gps/ang/type iso
/gps/ene/type Mono
/gps/energy 1000 keV
```

5.5.3 Sensitive Detector

Volumes that provide tracking information are classified as sensitive detectors in Geant4 simulations. Positron interactions are recorded in list-mode format for subsequent image reconstruction purposes. Relevant information stored for sensitive detectors include energy deposited, volume of where the interaction occurred, and interaction coordinates within that volume. An example of a typical output for a sensitive volume is shown below:

Step#	X(mm)	Y(mm)	Z(mm)	KinE(MeV)	dE(MeV)	StepLeng	TrackLeng	NextVolume	ProcName
8	-20	79.9	-51.3	0	0.0633	0.739	102	lyso4	phot

5.5.4 Geant4 Simulation – Stem Phantom

Monte Carlo simulations were designed to (1) measure detector sensitivity with the use of plastic converters around plant tissue and (2) estimate positron escape fractions for a given plant anatomy. In Geant4, the stem is modeled as a homogenous

material consisting of water. ^{11}C activity is uniformly distributed throughout the inner volume of the stem designated as the phloem where actual carbohydrate transport occurs. The phloem is a 2.0 mm-thick tube of water surrounding a 3 mm-thick pith in the stem. The wall of the stem are modeled as a 0.1 mm thick material composed of water. The total length of the stem is 18.5 centimeter (cm).

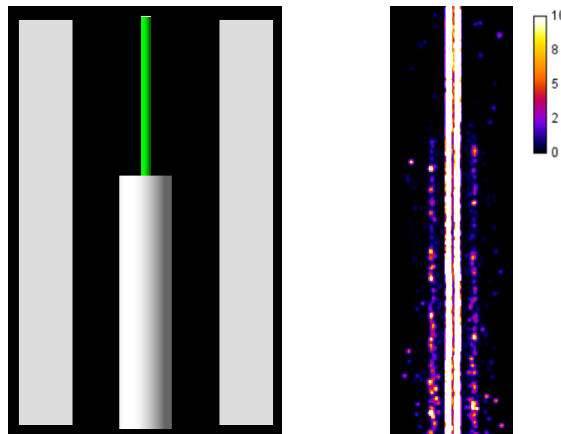


Figure 26. (Left) Screen output from Geant4 simulation of stem and PhytoPET detectors with two-thirds of the phantom surrounded by an (white) acrylic converter and (right) reconstructed image of simulation data.

LYSO detectors are stacked in a 1 x 4 configuration on opposite sides of the stem phantom with a face-to-face detector distance of 6 cm, as shown in Fig. 26 (left). A 3 mm-thick acrylic tube is used in the simulation for comparison with a “gloveless” plant stem. Gloving the stem increases the detection efficiency within the field of view (FOV) of the detectors [Ale11]. The use of plastic positron converters poses a problem in plant imaging since acrylic can effect normal plant physiological functions by interfering with the plant’s natural environment. Plastic shielding can increase temperature gradients, reduce air flow, and affect light transmission [Wei12]. The gloving technique is also difficult to implement for certain types of plant geometry.

100,000 positrons are simulated in this study. Measured data reveals that using a plastic positron converter around the stem increases the detection efficiency and leads to higher counts for acrylic shielded (821) versus the non-shielded (555) volume, as shown in Fig. 26 (right). The simulated versus experimental escape fractions are 39.4% and 36.8%, respectively.

5.5.5 Geant4 Simulation – Corn Leaf

Another Geant4 simulation was designed to simulate a plant leaf emitting positrons during carbon-11 decay. Studies performed at TUNL typically involve plants ages within the range of 2 to 6 weeks; albeit younger plants are known to have thin leaves (less than 0.2 mm) [Wei12]. Therefore in our simulation, a thin leaf was modeled as depicted in Fig. 27. The midvein (midrib) is a 0.5 mm diameter tube consisting of water. The phloem tissue is modeled as a 0.4 mm diameter tube embedded in the leaf midvein. 100,000 positrons are emitted from the leaf where 75% is allocated to the phloem in the midvein. The other 25% is distributed within the remaining leaf volume. Fractional allocation is determined using previous experimental data.

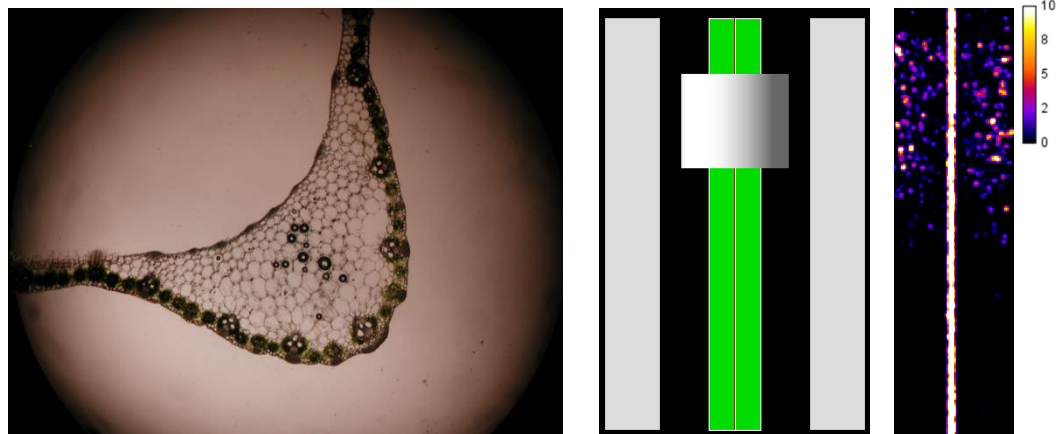


Figure 27. (Left) Midvein cross-section of corn seedling (thickness = 0.4 mm) using 40x magnification. (Center) Screen output from Geant4 simulation of LYSO array and leaf surrounded by plastic shield and (right) reconstructed image of simulation data.

Monte Carlo simulations indicate that the use of acrylic plastic around the stem slightly improved detected counts (%diff \approx 30%) as shown in Table 10. In contrast, plastic shielding significantly increased the detected counts from the leaf region by a factor of two. Modeling the positron escape fraction from a particular plant species based on tissue structure and anatomy can be useful for scaling the measured counts by a predetermined efficiency factor as shown in Equation 5.3.

$$\text{Adjusted Counts} = \text{Measured Counts} \div \epsilon_{MC} \quad (5.3)$$

Estimating positron escape efficiency from a Monte Carlo simulation can help improve statistical accuracy in plant radiotracer studies. Simulations of plant experiments can help estimate the fraction of positrons escaping the FOV of the detector pair for a given plant organ (i.e. leaf, stem, or root) with prior knowledge of plant tissue structure. Anatomical imaging will therefore be necessary for accurate comparisons. Current methods for noninvasive imaging of plant anatomy include optical projection tomography and micro-CT [Paj13]. For example, using the data in Table 10, measurements made on

an “ungloved” leaf with similar dimensions can be scaled by an efficiency value (ϵ_{MC}) of approximately 0.296. The updated value approaches a better estimate of the radiotracer accumulation and transport for that particular plant organ.

Table 10. Effects of acrylic positron conversion on PET counting statistics.

Plant Organ	Plastic Converter	Experimental Counts	Simulated Counts
Leaf	No	5,541	4,535
Leaf	Yes	18,733	13,917
% Difference		238.1%	206.8%
Stem Phantom	No	532	555
Stem Phantom	Yes	842	821
% Difference		58.3%	47.9%

Despite the benefits of the Monte Carlo approach, this method does have a few disadvantages including the need for anatomical imaging of the plant subject: (1) transmission imaging of plant subjects may consume total available experimental time leading to lower plant PET imaging samples, (2) potential damage to plant anatomy can occur due to excessive handling, and (3) there can be changes to plant anatomy at the time of radiotracer measurement versus anatomical imaging. The third disadvantage may be overcome by estimating the average growth for a species by imaging a sample of a particular species a given period of time.

The disadvantages of the previous methods for overcoming positron range effects, (1) plastic annihilation converters and (2) efficiency adjustments using a Monte Carlo approach, suggests a need for a new strategy in performing small plant radiotracer imaging studies. The next chapter introduces direct imaging of positrons escaping from plant tissue.

Chapter 6: Direct Positron Detection

The use of PET imaging in plant functional studies comes with some limitations, such as positron escape from shallow tissue [Wu11]. Positron range effects therefore present a challenge in quantifying radioactivity in specific plant volumes. The previous chapter introduced a method of achieving absolute quantification for accurate activity estimates by incorporating a Monte Carlo approach to account for positron escape fractions based on plant anatomy modeling. The disadvantages to this approach are (1) damage caused by excessive handling of the plant subject during tissue cross-sectional imaging and (2) inaccurate estimates arising from simulation modeling. A new technique is proposed in this section for detecting emitted positrons that escape from plant tissue for improved statistical analysis.

There have been previous attempts at functional imaging in plant biology studies using beta-positive particle imagers. One study reported a sensitivity increase between one to two orders of magnitude for direct positron imaging compared to traditional PET imaging [Sto09]. Another research group developed an imaging system for simultaneous measurements of positrons and annihilation gamma rays using a combination of scintillators optically coupled to a common photomultiplier tube [Wu11]. The drawback to both systems is the necessity for the detector(s) to be in very close proximity to the plant leaf, which may disturb leaf function and impact the study. The system proposed in this thesis overcomes this dilemma.

Direct positron detection is possible via a proposed configuration of detectors that can image a positron source without the need for annihilation photons. The proposed configuration consists of two separate types of detectors. The first is a double-

sided silicon strip detector (DSSD) positioned closer to the imaging subject. The second detector is a scintillating detector placed behind the DSSD. The scintillating detector allows for partial or complete absorption of the final positron energy. Both detectors must have 2D position resolution capabilities for image reconstruction purposes. The use of segmented silicon strip detectors in medical imaging and basic nuclear physics research has increased over the past few years due to their high spatial resolution capabilities [Par06].

This chapter provides a framework for deploying silicon strip detectors in small plant imaging studies. The use of conventional imaging techniques such as PET in plant radiotracer imaging has some limitations on plant leaf imaging. For example, a corn leaf blade tissue can have an average thickness between 0.1 and 0.5 mm. Positrons emitted from carbon-11 nuclei may require approximately between 1 to 4 mm of plastic material before reaching thermal energy and annihilating [Wei12]. Unfortunately, the use of plastic annihilation material can affect physiological responses in plants and may prove difficult to implement for whole plant imaging. We propose to develop a system that directly measures positron decay, thereby taking advantage of the finite range of positron travel. The design of positron position-sensitive detectors has become feasible due to the recent improvements in silicon strip detector technology.

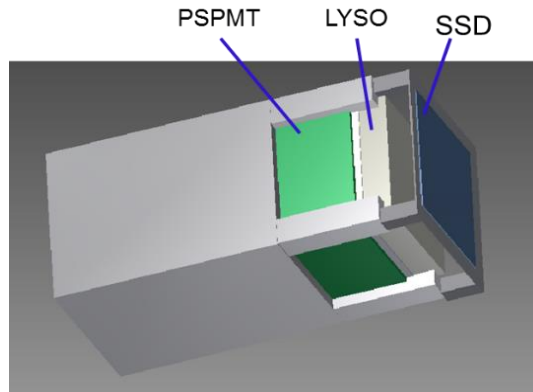


Figure 28. Rendering of proposed detector module consisting of a silicon strip detector coupled to a BGO scintillation detector assembly.

A potential assembly design for the dual detection system is shown in Fig. 28. Beta particles moving through the silicon strip will deposit a small fraction of energy prior to escaping. Emerging positrons are free to interact with a scintillation detector placed directly behind the DSSD. As depicted in Fig. 29, positron interaction in both detector provide hit coordinates useful for image reconstruction purposes.

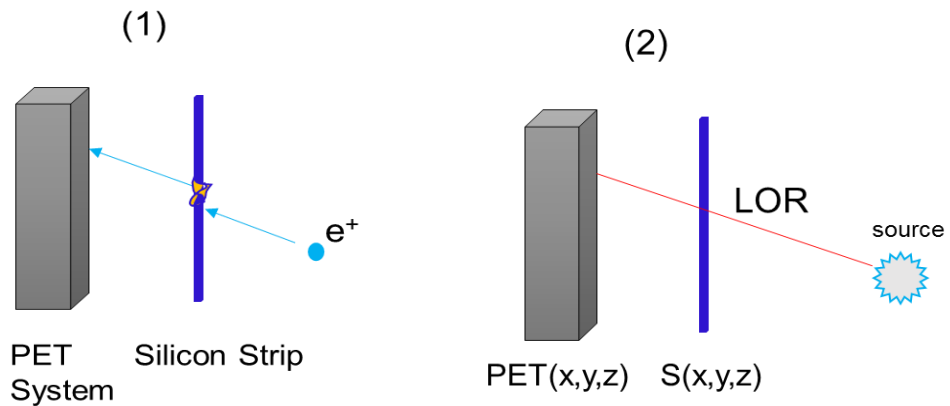


Figure 29. Diagram of positron tracking using silicon strip and PET detector coincidence events.

6.1 Silicon Strip Detectors

The relatively low density of silicon (2.33 g/cm^3) and thin nature of silicon strips, 100-300 microns (μm), allow positrons to pass through its volume while depositing energy and generating hit position data. Silicon detectors are basically solid state ionization chambers that takes advantage of the electronic structure of a semi-conductor [Leo94]. The silicon electron energy band structure can be modified by adding impurities such as boron and phosphor to form a diode. Applying an external potential, as shown in Fig. 30, forms a junction where traversing positrons can interact and induce a signal. As positrons travel through silicon, they produce electron-hole pairs through ionization. The number of electron-hole pairs produced depends on the charge and energy loss in the material and the signal generated is proportional to the amount of energy deposited.

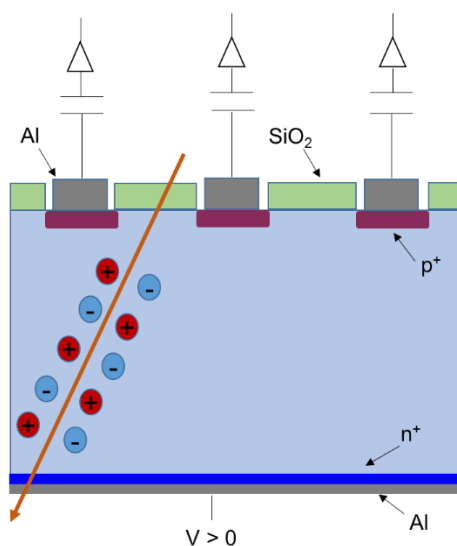


Figure 30. Cross section of a double-sided detector. Image adapted from [Kra01].

For positrons in the energy range of interest (100 keV to 1 MeV), the stopping power approached the minimum for ionizing particles ($\sim 1.9 \text{ MeV cm}^2/\text{g}$) as shown in Fig. 31. In this region, the detector signal is proportional to the amount of energy loss in silicon (dE/dx).

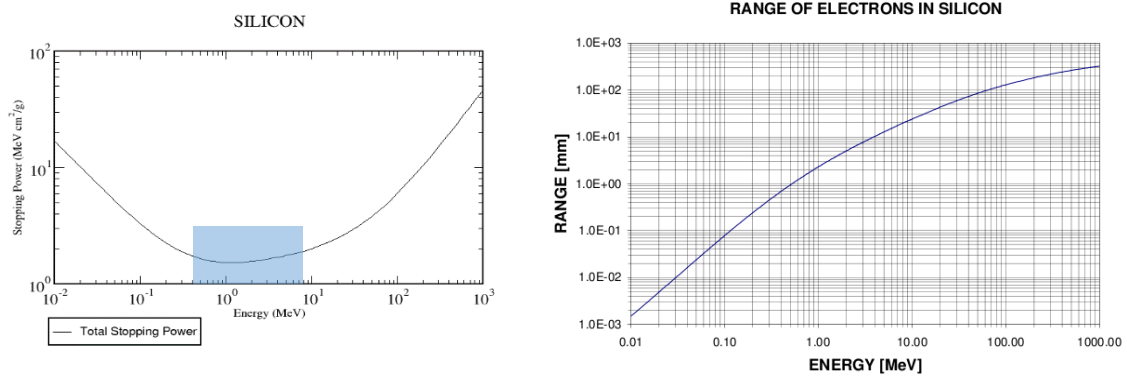


Figure 31. Stopping power vs. kinetic energy for positrons in silicon (left) and graph of electron range in silicon (right). Figure referenced from [Ber99] and [Spi99], respectively.

Silicon strips can provide high precision tracking information. In order to obtain position data, equally spaced and parallel p implants are made within the n-type bulk silicon material as shown. P-type and n-type strips can be placed on opposite side of the bulk silicon. This results in a double-sided detector that can provide two dimensional position information. N-type silicon is formed by using a donor atom such as phosphor to dope the crystal. Since phosphor has five valence electrons, silicon's four valence electrons form a hexagonal crystal leaving an electron to sit close to the conduction band. P-type silicon is formed using acceptor atoms such as boron, which has three valence electrons. An electron from silicon's valence shell is caught by boron and forms a hexagonal structure leaving a hole due to the missing electron. The strip position that provides a signal determines the location of ionizing particle interaction. Detector spatial

resolution depends heavily on the spacing (pitch) between strips with typical values between 10 μm - 1 mm. Signals are readout by electronics on the edge of the silicon detector to keep the tracking volume free for particle interactions.

6.1.1 Advantages using Silicon Strip Detection

The advantages of silicon strip detectors over traditional scintillating detectors are numerous [Mon05]:

- Low noise at room temperature due to moderate energy band gap (1.12 eV).
- High spatial resolution capabilities ($\sim 10 \mu\text{m}$ to 1 mm).
- High energy resolution (energy needed to create electron-hole pair is 3.6 eV).
- Fast signal processing— less than 30 ns to collect entire signal
- Flexibility of detector design

6.1.2 Challenges using Silicon Strip Detection

Implementing DSSD for tracking of positrons can be a concern due to the relatively low positron energy of our most common radioisotopes ($< 2 \text{ MeV}$). For thin detector layers, a relatively smaller production of charge is created as compared to thicker silicon detectors. In the presence of electronic noise, the signal may be masked. Silicon detectors also have fast response times (ns) during signal generation [Kno89]. Careful selection of read-out electronics is necessary for optimal processing of the raw data.

6.2 Monte Carlo Simulations

A Geant4 Monte Carlo simulation was used to determine the feasibility of performing imaging studies with direct positron detection. The theoretical energy

spectrum for positrons emitted from carbon-11 (^{11}C) nuclei were simulated using both spherical and cylinder-shaped sources. In the simulation, positron trajectories are modeled as random walks that can estimate the positron's mean path length, scattering angle, and energy loss through silicon. In this Geant4 simulation, individual positron trajectories are randomized based on the statistical interaction probabilities in silicon.

6.2.1 Spherical Source Simulation

We modeled a 0.25-mm diameter spherical source composed of water emitting 100,000 positrons. Positrons were emitted isotropically as shown in Fig. 32. As mentioned earlier, BGO and DSSD detector pairs are used for positron detection. The blue square in Fig. 32 is a 200 μm (thick) DSSD. The white square is a BGO detector (48 mm x 48 mm x 1 inch) placed a distance of one inch behind the DSSD (48 mm x 48 mm x 200 μm) on the side opposite to the positron source. The DSSD is positioned a distance of 1 cm away from the spherical source.

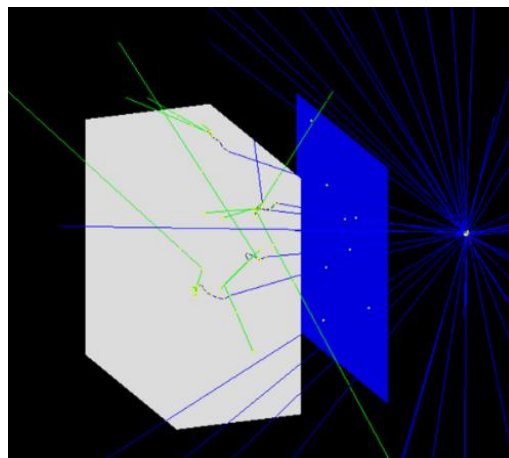


Figure 32. Geant4 screen output of simple dual detection geometry that includes a BGO detector (white), silicon material (blue), and an ^{11}C point source.

6.2.1.1 Reconstructed Image

A ^{11}C point-like source, having 0.25-mm diameter, was used to test the feasibility of dual positron detection by directly measuring the spatial resolution of the system in terms of full-width at half maximum (FWHM). FWHM is defined as the resolving power of a detection system for two distinct objects as the distance between the two objects decrease. As indicated in Fig. 33, spatial resolution was measured to be approximately $\text{FWHM} \approx 4 \text{ mm}$, with image degradation mainly due to positron multiple scattering in silicon.

The relatively low average positron energy (326 keV) for ^{11}C is responsible for larger deflection angles as compared to radioisotopes with higher average energies. Scattering in silicon results in changing the trajectory of the positron as it exits the material. Scattered positrons produce blur in reconstructed images, as shown in Fig. 33(left), and broadening of spatial resolution profiles due to incorrect positioning of positron interaction points in the BGO detector.

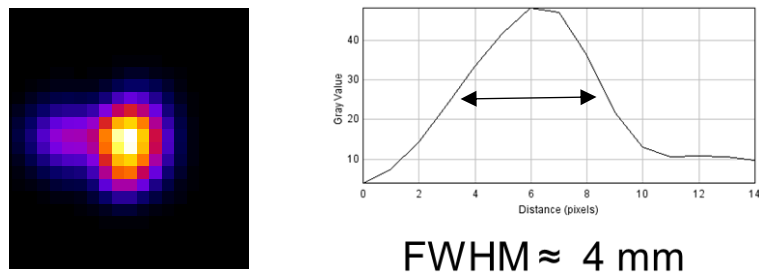


Figure 33. Reconstructed image of 0.25 mm ^{11}C point source. A line profile through the center of the reconstructed image measures a FWHM of approximately 4 mm.

6.2.1.2 Energy Deposited

Geant4 simulation results indicate that positrons deposit a small fraction of their energy in either detector ($< 100 \text{ keV}$). Positrons interacting in silicon primarily lose most

of their energy through ionization and excitation with orbital electrons, resulting in multiple low-angle scattering events [Ayd05]. The number of electron-hole pairs created in silicon can be estimated using equation 6.1,

$$\text{No. of pairs} = \frac{\frac{dE}{dx} * d}{I_0} \quad (6.1)$$

$\frac{dE}{dx}$ is the mean positron energy loss in silicon (4.43 MeV/cm), d is the thickness of the detector ($d = 200 \mu\text{m}$), and I_0 is the mean ionization energy for silicon (3.62 eV).

Positrons incident on silicon can create approximately 24,475 electron-hole pairs. A signal is generated once the electron and holes drift towards the electrodes. The signal from each silicon strip is fed into the electron circuit discussed in section 6.2.1.5 to provide two-dimensional detector hit positions for use in image reconstruction.

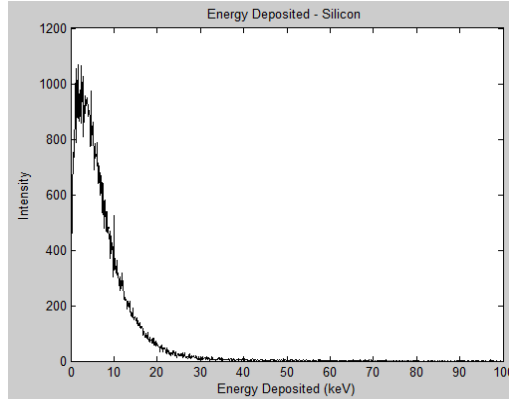


Figure 34. The deposited energy from positrons incident on silicon.

The mean energy loss for a positron emitted from a ^{11}C nucleus in silicon is approximately 44 KeV, however, the most probable energy loss for an incident positrons in silicon is usually less than 70% of the mean energy loss rate [Eid04], as shown in Fig. 34.

6.2.1.3 Scattered Events

The spatial resolution for this particular system consisting of a scintillator detector and a DSSD is limited by positron multiple scattering, as shown in Fig. 35. Low energy positrons (< 3 MeV) tend to change trajectories in silicon by undergoing multiple scattering.

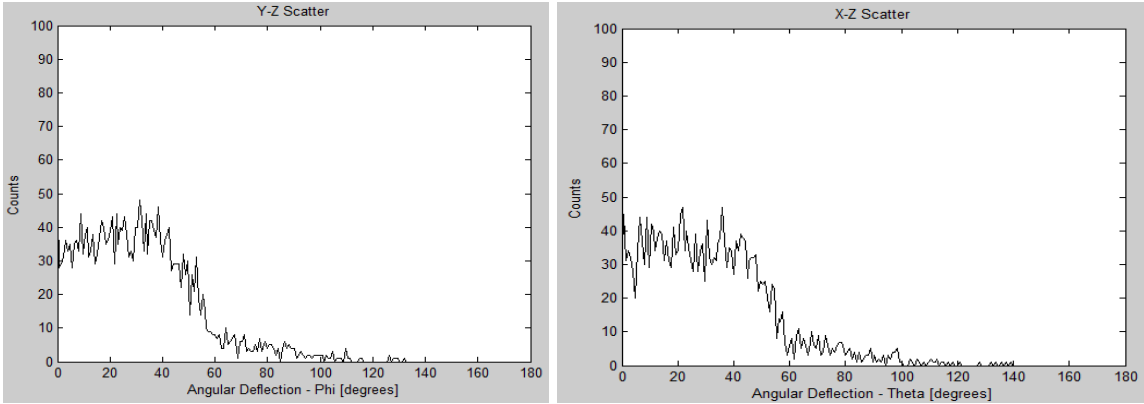


Figure 35. Simulated angular distribution of transmitted positrons in 200 μm silicon target for ^{11}C theoretical energy spectrum.

Positrons traversing silicon are deflected by small angular scatters as depicted in Fig. 35. The polar scattering angle for a positron incident on a given material can be determined using equation 6.2 [Ayd05],

$$\sin \theta = \frac{\Delta E}{E} \quad (6.2)$$

Positrons emitted from ^{11}C nuclei with an average energy of 326 KeV will have an expected deflection of 8 degrees. The scatter distribution for our simulation reflects the possible positron energy range for ^{11}C which is between zero and 960 keV.

6.2.1.4 Signal Readout Electronics

The readout electronics for silicon strip detectors must account for the small signal produced in the detector while also minimizing effects from noise sources such as detector capacitance and leakage current as discussed in section 6.2.1.5. The electronics must be capable of providing an adequate signal amplification while rejecting noise.

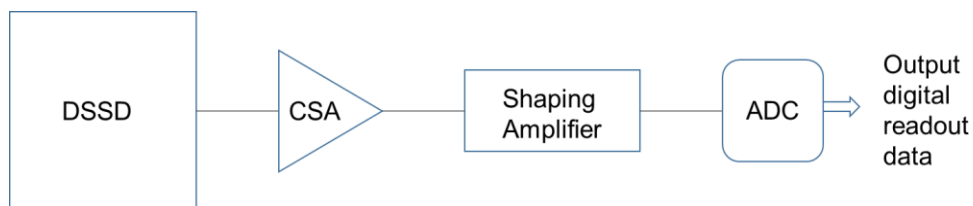


Figure 36. Block diagram of proposed silicon strip detection system.

Each silicon strip can be connected to a charge sensitive amplifier (CSA) that produces a voltage proportional to the positron energy deposition. A pulse shaper is subsequently incorporated to reject noise frequencies not corresponding with the signal frequency range [Ger01]. An analog-to-digital converter (ADC) can convert pulse data into a digital amplitude format (Fig. 36).

6.2.1.5 Silicon Signal-to-Noise Estimates

Calculating the expected noise from a typical DSSD will enable signal-to-noise (SNR) estimates. Components of noise in a solid-state detector-amplifier system are detector capacitance, leakage current, the quality of the CSA, and pulse shaping/filtering electronics. Noise is defined in terms of Equivalent Noise Charge (ENC) which is the root mean square of noise given in number of electrons as shown in equation 6.3 [Ber93]:

$$ENC^2 = e^2 * (A_1 q I_L \tau + \frac{A_2 C_{total}^2}{\tau}) \quad (6.3)$$

General components of system noise in a detector-amplifier system are total capacitance which includes detector and input capacitance (C_{tot}), characteristic shaping time of the pre-amplifier (τ), and leakage current (I_L) in the detector. The charge of an electron is captured in the variable q . Variables A_1 and A_2 are coefficients related to the pulse shaping electronics [Ger98] and are approximately equal to one for this application [Spi98]. This simulation is modeled to reflect a custom DSSD recently developed for nuclear physics applications which reports a strip capacitance of 30 pico-farads (pF) [Can]. Leakage current is another source of system noise and is defined as unwanted electron-hole pairs that are thermally generated [Spi99] and is reported for the same detector as 12 nano-amperes (nA). This measured for the custom DSSD previously mentioned was reported when a bias voltage of 60 was applied [Can].

In calculating the potential SNR, we use the average number of electrons generated per positron interaction (24,475 e^-), estimated in section 6.2.1.2, as the signal collected. We propose using a multiplex preamplifier capable of processing 128 channels for signal readout. The use of the preamplifier with the proposed DSSD will

produce a total estimated noise due to of approximately 1750 electrons. From this estimate of the system noise, the calculated SNR is fourteen.

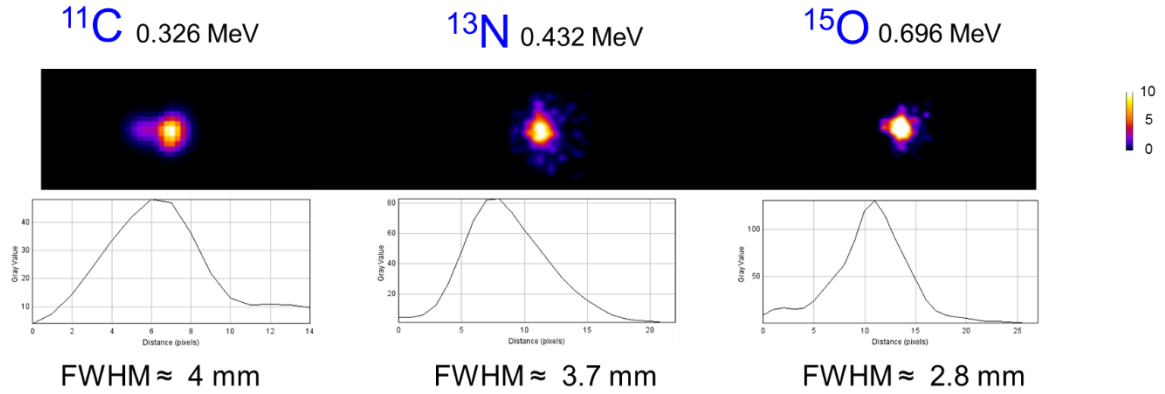


Figure 37. Reconstructed images for 0.5 mm point source of ^{11}C , ^{13}N , and ^{15}O , respectively.

6.2.2 Radioisotopes Comparisons

Simulations of the proposed imaging system were performed for three of the common radioisotopes used in small plant radiotracer studies. Reconstructed images of detector data indicate an improvement in spatial resolution for images generated using higher average positron energy as shown in Fig. 37.

As positron energies approach 5-10 MeV, the spatial resolution of this system approaches that of conventional PET imaging. Improvement in spatial resolution is largely due to a lower fraction of large angular scattering in silicon as the average energy increases. This effect is depicted in Fig. 38, where the 5 MeV positron has a near zero scattering angle above 50 degrees.

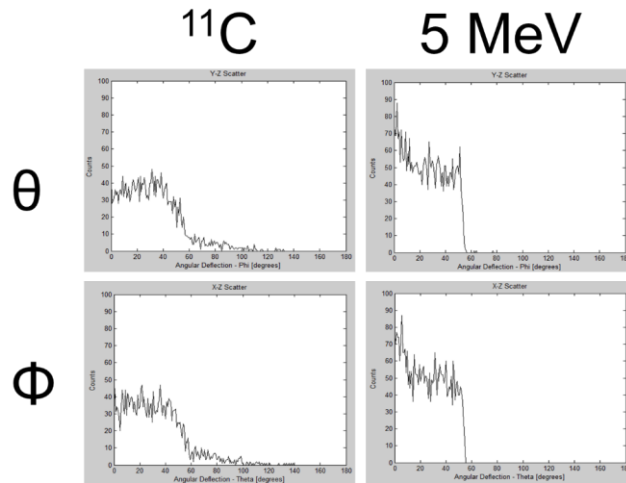


Figure 38. Simulated angular distribution of transmitted positrons in 200 μm silicon target for ^{11}C (left) theoretical energy spectrum and 5 MeV (right) positrons.

Dual positron detection is optimal for beta-emitting radioisotopes having higher average energies such as potassium-38 (1.214 MeV) and copper-62 (1.314 MeV). Maximum positron energy for potassium-38 (^{38}K) is reported as 2.68 MeV with a half-life of 7.6 minutes. Copper-62 (^{62}Cu) has a maximum positron energy of 2.92 MeV with a half-life of 9.74 minutes. Copper (Cu) is a micronutrient needed in small quantities in plants for photosynthesis, lignin synthesis, respiration, and plays a key role in carbohydrate metabolism. Potassium (K) plays a key role in plants by activating enzymes involved in plant growth and the production of adenosine triphosphate (ATP) [Tai02]. This system would be suitable for measuring root uptake of both ^{62}Cu and ^{38}K .

6.2.3 Planar PET Imaging vs. Direct Positron Detection

A second Geant4 simulation was performed to compare counting statistics between PET planar and direct positron detection. The geometry of an average barley leaf was used as the positron source. 100,000 positrons will be emitted isotropically within the volume of the leaf midvein, as depicted in Fig. 39.

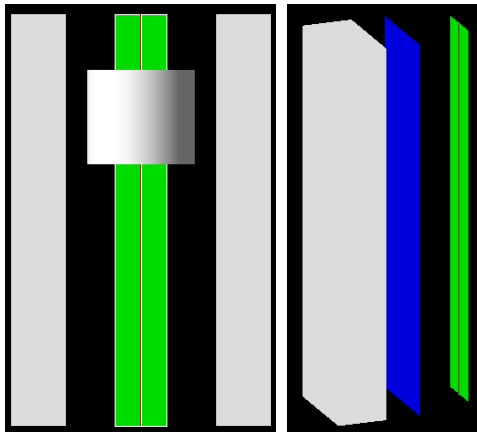


Figure 39. (Left) Geant4 simulation graphic rendering of PET detector setup and (Right) direct positron dual detection.

In this simulation, the leaf is modeled as a thin layer of water equivalent tissue of 0.1 mm thickness. The leaf midvein is composed of water having a 0.4 mm diameter. The source diameter is 0.2 mm diameter. Simulated data indicate that the modeled silicon detector assembly has an approximate factor of 3 improvement in positron detection efficiency, as listed in Table 11. Measured counts for the PET system generated 2,582 recorded events. There were 8,854 events using dual positron detection.

Reconstructed images are shown in Fig. 40. Spatial resolution improves as the average positron energy increases from 2 MeV to 10 MeV.

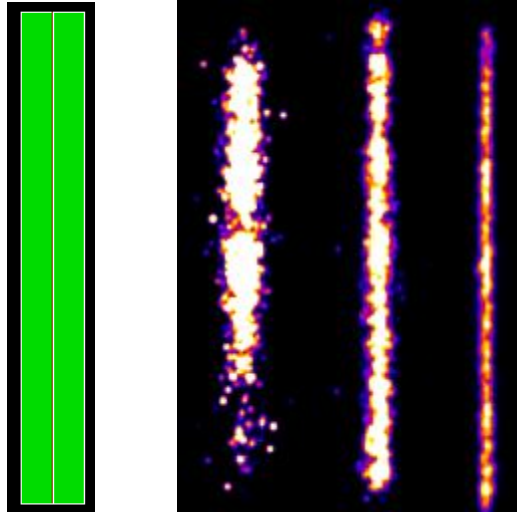


Figure 40. (Left) Geant4 graphic rendering of leaf model and mid vein. (Right) Reconstructed images of leaf source emitting positrons having kinetic energies of 2 MeV, 5 MeV, and 10 MeV from left to right.

Positron range effects result in measured activity not reflecting the actual activity concentrations. Since positrons emitted from common PET radioisotopes can travel up to a few millimeters in water before annihilation, it would be useful to take advantage of this phenomenon. It was recently reported that an escape fraction of ~70% is evident for positrons originating from within a 300 μm tobacco plant leaf when using ^{11}C [Ale11]. Our measurements are in agreement with a 68.2% escape fraction for this particular leaf geometry.

Table 11. Geant4 simulation recorded events for PET and direct positron detection imaging using identical ROI in ImageJ.

Plant Organ	No. of Incident Positrons	Planar PET Imaging (max)	Direct Positron Detection (2 MeV)
Leaf	100,000	2,582	8,854

6.3 In Closing

Absolute quantification of carbohydrate partitioning can be achieved in plant radiotracer studies and is necessary for accurate interpretation of measured data. These type of studies can be important for understanding plant response to changes in the environment (e.g. atmospheric CO₂ concentration and soil nutrient content) towards forecasting crop yield.

The radiotracer system developed at TUNL was utilized in an investigation to measure barley response to sudden changes in root nutrient availability under both ambient and elevated atmospheric CO₂ conditions. More specifically, the spatial distribution of recently tagged carbohydrates was monitored using a custom PET imaging system that allowed for *in vivo* measurements on barley. ¹¹CO₂ gas was produced using the Van de Graaff accelerator at the TUNL facility and transported to the measurement site using a radioactive gas transfer system. This work contains the largest reported set of plant subjects (n = 31) in a plant radiotracer study. We observed a significant effect of atmospheric CO₂ concentration on carbohydrate allocation in barley. At elevated CO₂ barley allocated more recently fixed sugar aboveground. Changes in atmospheric CO₂ levels did not have a significant effect on root exudation or respiration. We observed a rapid (i.e., within 3 hours) response from barley during short-term changes in root nutrient availability. Switching from high to low nutrient solution, in both ambient and elevated atmospheric CO₂ conditions, resulted in an average decrease in the amount of carbon allocated to below ground sinks. The observed response could be partly due to the plant leaf not willing to give up resources, in this case carbohydrates, without the promise of getting nutrients back in return. Plants grown in low nutrient

solution, when switched to high nutrient, expressed no response to their new environment in the short period of our study. It is possible that the plant mechanism acclimated to the low nutrient conditions and the mechanism involved in adjusting to new conditions responds at a much longer interval than we are able to measure.

Appendix A: Carbon-11 Gas Transfer and Labeling Loop

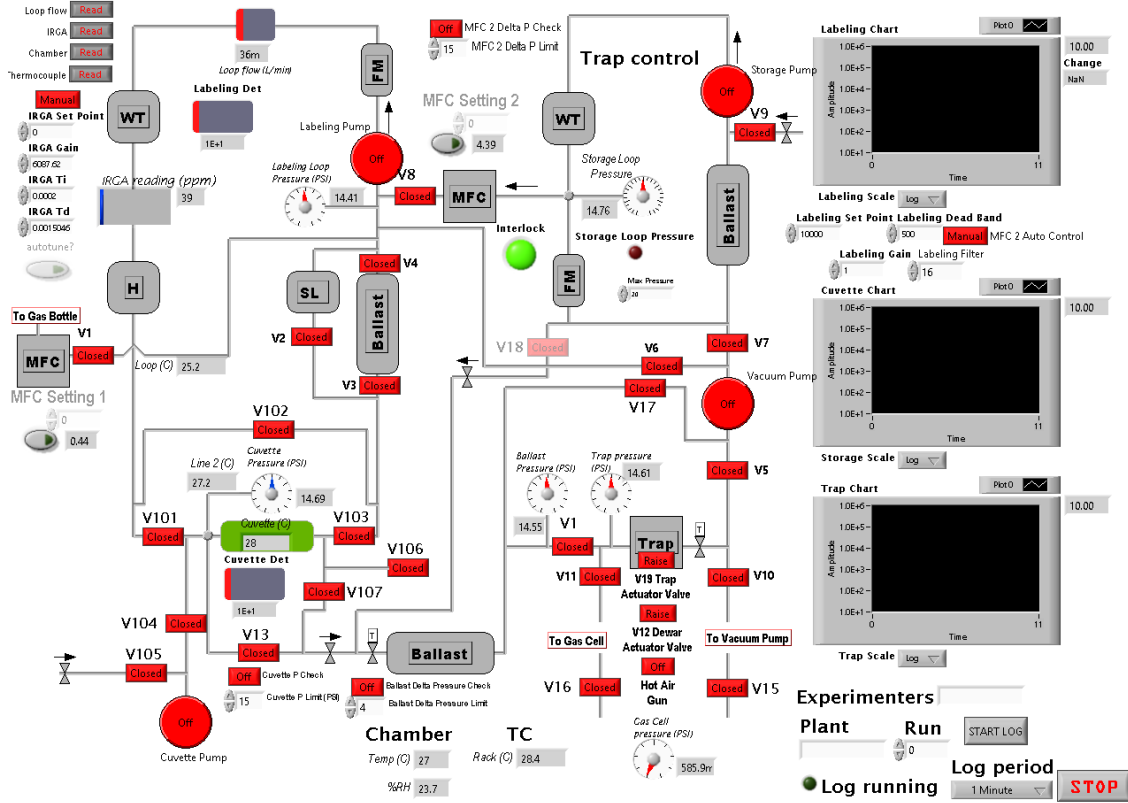


Figure 41. Screenshot of the LabVIEW controlled radioactive gas handling system for transfer from the $^{11}\text{CO}_2$ production area located at TUNL to the labeling chamber at the Phytotron.

A summary of components that make up the labeling system are listed in Table 12 along with a short description of each component and known volume.

Table 12. Summary of components that make up the labeling loop between TUNL and the Phytotron facilities.

Labeling Loop Component	Volume (cm³)	Description
Main Labeling Loop	34.5	A closed loop system for radioactive ¹¹ CO ₂ circulation through a plant leaf cuvette.
Continuous Loading Loop	1020	A storage volume for ¹¹ CO ₂ that provides replenishment of gas for constant activity capabilities.
CO ₂ Trap	10.4	A liquid nitrogen-cooled cryogenic trap for isolation of carbon dioxide.
Ballast Tank	1020	Volume designated as a pressure buffer and air mixture.
Line Sampling Volume	21.7	Plastic cylinder used to sample radioactive flow.
Drying Flask	130	Flask used to remove water molecules. Contains magnesium perchlorate.
Humidifier/Condenser	29.0	Used to maintain the relative humidity in the labeling loop.
Leaf Cuvette	180	Labeled leaf is sealed in air tight volume with dimensions of 15 cm x 5 cm x 2.4 cm
Infrared Gas Analyzer	11.9	Monitors CO ₂ concentration as a function of one minute intervals.

The total loop volume is 1790 cm³ (± 5%), of which ΔV = 21.7 cm³ is sampled by the line detector. This is a sampling fraction of 0.93% (from [Kis08]).

Operating Procedures

Bringing to Bypass

From Startup

- Initially all valves should be closed
- 1. Open v3, v4, and v102
- 2. Turn On LABELING PUMP

After Leaf is Sealed in Cuvette

1. Open v104, v104, and v106
2. Turn On CUVETTE PUMP

Loading the Liquid Nitrogen Trap

Trap Evacuation

1. Open Trap Throttle Valve (Manually)
2. Verify the TUNL Vacuum PUMP is on in Target Room 4
3. Open v10, v11, and v15
4. Let TRAP PRESSURE lower to approximately one-half psi
5. Raise v12 DEWAR ACTUATOR VALVE

C-11 Loading

1. Close TRAP THROTTLE valve then Open one-quarter turn (Manually)
2. Verify the TUNL Vacuum PUMP is on in Target Room 4
3. Fill DEWAR with Liquid Nitrogen
4. Open v16
5. Observe the trap's radioactivity via the TRAP CHART, wait for steady-state
6. Close v11, v10, v16, and v15

7. Fully Open Trap Throttle (Manually)

Loading the Labeling Loop

Warming the LN Trap

1. Lower the Dewar and Raise the Trap
2. Turn on Hot Air Gun for 2 minutes

Loading the Loop

1. Open v5 and v6
2. Turn on VACUUM PUMP
3. Let TRAP PRESSURE decrease to approximately 0.200 psi
4. Burp air into trap to aid its evacuation
 - (a) Turn Off VACUUM PUMP
 - (b) Briefly Open v1 and Close
 - (c) Turn On VACUUM PUMP
 - (d) Repeat sequence a-c once more when TRAP PRESSURE falls below 0.200 psi
5. Once the loop is loaded. Close v5, v6, and Turn Off the VACUUM PUMP

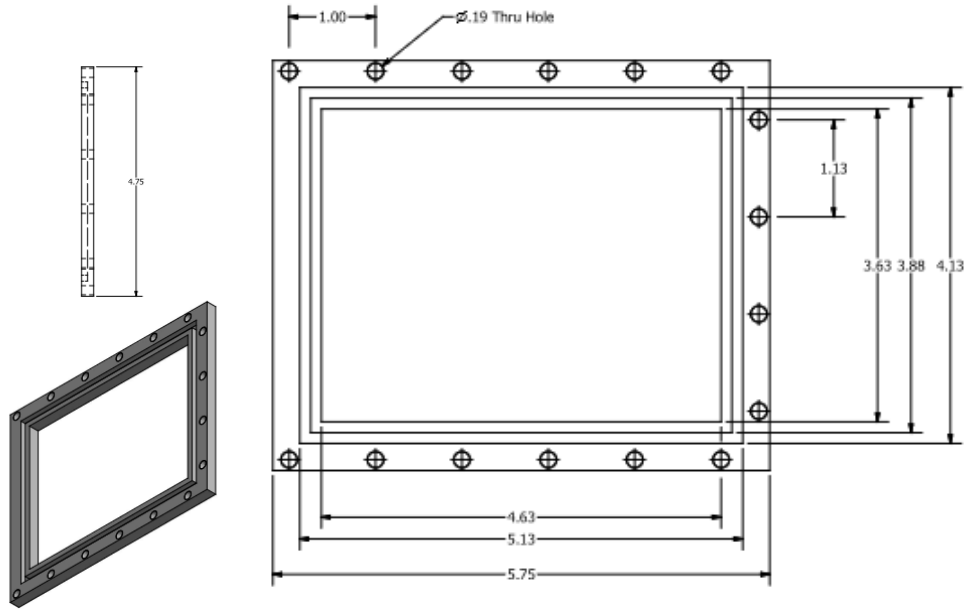
Cuvette Isotope Injection

1. Turn Off CUVETTE PUMP
2. Close v104 and v106
3. Open V101 and v103, Close v102

Appendix B: Glossary

- **coincidence:** measurement of two events occurring in two separate detectors within a given time interval.
- **cuvette:** a square plastic case designed to seal a plant leaf during plant labeling experiments using C-11 tagged carbon dioxide.
- **exudation:** the release of soluble organic compounds from plant root tissue into the rhizosphere.
- **metabolite:** essential organic compounds synthesized by plants for use in growth and development.
- **phloem:** plant vascular tissue that transports carbohydrates and other metabolites to source organs.
- **photosynthates:** any compound that is a by-product of photosynthesis.
- **respiration:** breakdown of carbohydrates into a useable energy source in a cell.
- **rhizosphere:** the immediate region of soil surrounding root tissue.
- **short-lived:** radioisotopes whose half-lives are less than two days.
- **sink:** a plant organ that cannot produce its own carbohydrate needs.
- **source:** an organ that exports carbohydrates beyond its own need to various sinks.

Appendix C: Leaf Cuvette Development



Leaf absorption of carbon-11 tagged carbon dioxide ($^{11}\text{CO}_2$) occurs in a sealed cuvette. The cuvette allows the radiotracer gas to be absorbed in a known plant leaf area while the rest of the plant is exposed to non-radioactive air. Typically, the cuvette would seal a single blade or leaf around a predetermined cross-section of the leaf including the midvein. The seals on our cuvettes are designed to be achieved with low pressure exerted on the plant tissue to minimize disturbance of the fluid conducting vessels. Field testing of prototype cuvettes designed for different types of plants, e.g., grasses and seedlings, were carried out to optimize the seal. Through empirical methods, we have developed a gasket material that meets the seal requirements of the planned research program. The cuvette gasket is made of Ecoflex® gel, a very soft and “stretchy” silicon product [Eco]. The liquid mold is poured into the cuvette groove and

hardens when it cools. Once casting is completed, the soft gel helps seal the leaf cuvette from the external air while also not damaging the plant anatomy.

Appendix D: Input-Output Model Results

Table 13. Barley plant detail summary with experimental parameters for individual plants.

Plant No.	Run #	Nutrient Availability Order	Atmospheric [CO ₂]
4	1481/1482	High/Low	Elevated
5	1483/1484	High/Low	Elevated
6	1485/1486	Low/High	Elevated
7	1489/1490	Low/High	Elevated
8	1491/1492	High/Low	Elevated
10	1498/1499	Low/High	<i>Ambient</i>
11	1500/1501	Low/High	<i>Ambient</i>
14	1506/1507	Low/High	<i>Ambient</i>
15	1508/1509	Low/High	<i>Ambient</i>
16	1521/1522	Low/High	<i>Ambient</i>
17	1523/1524	Low/High	<i>Ambient</i>
18	1525/1527	Low/High	<i>Ambient</i>
19	1528/1530	High/Low	<i>Ambient</i>
20	1531/1532	High/Low	<i>Ambient</i>
21	1533/1534	Low/Low	<i>Ambient</i>

Table 14. Effects of elevated atmospheric CO₂ concentration on carbon allocation and transport under High and Low nutrient levels for barley.

ELEVATED CO₂						
Plant No.	Leaf Export		Shoot Export		Below Ground Allocation	
	Low Nutrient	High Nutrient	Low Nutrient	High Nutrient	Low Nutrient	High Nutrient
4	0.66	0.84	0.11	0.34	0.07	0.16
5	0.75	0.80	0.09	0.29	0.07	0.23
6*	0.61	0.67	0.20	0.24	0.12	0.16
7*	0.81	0.75	0.15	0.24	0.12	0.18
8	0.31	0.31	0.24	0.18	0.07	0.06

**Indicates that the Low Nutrient data were taken in the morning and High Nutrient in the afternoon.*

The belowground fraction is the product of the leaf export fraction and shoot export fraction. Values shown are the computed values calculated from the input-output model.

Table 15. Effects of ambient atmospheric CO₂ concentration on carbon allocation and transport under High and Low nutrient levels for barley.

Ambient CO ₂						
Plant No.	Leaf Export		Shoot Export		Below Ground Allocation	
	Low Nutrient	High Nutrient	Low Nutrient	High Nutrient	Low Nutrient	High Nutrient
10*	0.61	0.42	0.30	0.35	0.19	0.07
11*	0.72	0.49	0.06	0.21	0.04	0.10
14*	0.70	0.73	0.62	0.31	0.44	0.23
15*	0.77	0.79	0.64	0.47	0.49	0.37
16*	0.65	0.68	0.18	0.22	0.47	0.46
17*	0.50	0.66	0.16	0.68	0.34	0.47
18*	0.39	0.35	0.21	0.22	0.08	0.08
19	0.60	0.82	0.96	0.99	0.60	0.81
20	0.61	0.79	0.88	0.96	0.54	0.76
21**	0.18	0.40	0.70	0.66	0.13	0.27

*Indicates that the Low Nutrient data were taken in the morning and High Nutrient in the afternoon.

Indicates that the Low Nutrient data were taken in the morning and **also Low Nutrient in the afternoon.

The belowground fraction is the product of the leaf export fraction and shoot export fraction. Values shown are the computed values calculated from the input-output model.

Table 16. Average values of values from Tables 15 and 16 and number of samples in each category.

Analysis	Elevated [CO ₂]	Ambient [CO ₂]	Elevated [CO ₂]	Ambient [CO ₂]
	High	High	Low	Low
Leaf Export	0.50 ± 0.04 (n = 19)	0.62 ± 0.05 (n = 12)	0.46 ± 0.04 (n = 19)	0.55 ± 0.04 (n = 14)
Shoot Export	0.44 ± 0.04 (n = 19)	0.56 ± 0.08 (n = 12)	0.44 ± 0.05 (n = 19)	0.60 ± 0.07 (n = 14)
Below Ground Allocation	0.20 ± 0.02 (n = 19)	0.37 ± 0.07 (n = 12)	0.18 ± 0.02 (n = 19)	0.33 ± 0.05 (n = 14)
Exudation	0.019 ± 0.003 (n = 19)	0.019 ± 0.003 (n = 12)	0.022 ± 0.005 (n = 19)	0.021 ± 0.003 (n = 14)
Respiration	0.012 ± 0.005 (n = 17)	0.016 ± 0.002 (n = 12)	0.008 ± 0.002 (n = 14)	0.009 ± 0.002 (n = 14)

Table 8. Average values for each category presenting the effects of switching nutrient treatments for both ambient and elevated CO₂.

Analysis	Elevated [CO ₂]	Ambient [CO ₂]	Elevated [CO ₂]	Ambient [CO ₂]
	H to L	H to L	L to H	L to H
% Diff in Below Ground Allocation	-0.37 ± 0.14 (n = 7)	-0.31 ± 0.09 (n = 4)	0.07 ± 0.17 (n = 8)	0.004 ± 0.24 (n = 8)
% Diff in Exudate	-0.13 ± 0.13 (n = 7)	0.04 ± 0.19 (n = 4)	0.27 ± 0.20 (n = 8)	0.08 ± 0.29 (n = 8)
% Diff in Respiration	-0.41 ± 0.22 (n = 6)	-0.52 ± 0.09 (n = 4)	-0.20 ± 0.17 (n = 6)	0.81 ± 0.39 (n = 8)

Table 9. Photosynthetic rate measurements for ambient atmospheric CO₂ conditions.

Ambient CO ₂ Plant No.	Photosynthetic Rate	
	Low Nutrient	High Nutrient
10*	4.35	6.74
11*	3.15	-
14*	10.13	8.11
15*	3.31	-
16*	10.14	22.19
17*	12.18	8.81
18*	2.72	-
19	2.88	5.44
20	-	7.12
21**	5.88	16.37

*Indicates that the Low Nutrient data were taken in the morning and High Nutrient in the afternoon.

Indicates that the Low Nutrient data were taken in the morning and **also Low Nutrient in the afternoon.

Table 10. Photosynthetic rate measurements for elevated atmospheric CO₂ conditions.

ELEVATED CO ₂ Plant No.	Photosynthetic Rate	
	Low Nutrient	High Nutrient
4	2.54	5.55
5	3.29	4.31
6*	6.06	6.11
7*	6.79	-

*Indicates that the Low Nutrient data were taken in the morning and High Nutrient in the afternoon.

Appendix E: Photosynthetic Rate Derivations

A. IRGA Method – No Loop Leak

Using an IRGA is one way of determining the amount of carbon absorption by the area of leaf exposed to gas in the labeling loop.

$$P_S = \frac{d\rho}{dt} * \frac{V_{loop}}{A_{leaf}} \quad (E.1)$$

Density (ρ) in our case is the total number of carbon dioxide molecules in the total volume of the closed loop system.

$$\rho = \frac{n_c(\text{mol of } CO_2)}{V_{loop}} \quad (E.2)$$

Since the concentration of CO_2 in air can be related as $c = n_c/n_{air}$,

$$\rho = \frac{c * n_{air}}{V_{loop}} \quad (E.3)$$

The molar concentration of air (n_{air}) can be determined by using the ideal gas law and measuring pressure and temperature in the loop.

$$\rho = \frac{c}{V_{loop}} * \frac{P * V_{loop}}{RT} \quad (E.4)$$

With density defined more precisely, we can differentiate and simplify the photosynthetic rate equation for use in experimental applications.

$$P_S = \frac{d}{dt} \left[\frac{c(t)}{V_{loop}} * \frac{P * V_{loop}}{RT} \right] * \frac{V_{loop}}{A_{leaf}} \quad (E.5)$$

If there are no leaks in the labeling loop, pressure remains constant over time.

Leaving only the concentration term, $c(t)$ for differentiation.

$$P_S = \frac{P * V_{loop}}{A_{leaf} RT} * \frac{d[IRGA]}{dt} \quad (E.6)$$

The IRGA measurements directly provide the concentration of CO₂ molecules in the loop.

B. IRGA Method – With Known Loop Leak

A gas leak in the closed loop system would cause pressure to change as a function of time. Cancellation of the pressure term would not be allowed in this case.

$$P_S = \frac{d}{dt} \left[\frac{c(t)}{V_{loop}} * \frac{P(t) * V_{loop}}{RT} \right] * \frac{V_{loop}}{A_{leaf}} \quad (E.7)$$

$$P_S = \frac{d}{dt} \left[\frac{c(t) * P(t)}{RT} \right] * \frac{V_{loop}}{A_{leaf}} \quad (E.8)$$

Since the leak in the system occurs locally, we would have to use the average pressure since we are including the entire loop volume.

$$P_S = \frac{\langle P \rangle}{\langle RT \rangle} * \frac{d[IRGA]}{dt} * \frac{V_{loop}}{A_{leaf}} \quad (E.9)$$

To calculate average pressure, a pressure reading is taken at the start of the experiment when the pump is turned OFF. There should be no plant activity for absorption of CO₂, therefore having the lights off in the chamber or using another mechanism to inactivate the plant is necessary. A second pressure reading is recorded

after the pump is turned ON. The ratio of the two measurements provide the constant needed to calculate the average pressure at a given point in the closed loop.

$$\langle P \rangle = k(x) * P(x, t) \quad (E.10)$$

$P(x,t)$ is the pressure function and is given by monitoring pressure at any point in the loop. The constant $k(x)$ is determined at time equal zero. The expression for k is given in the following statement.

$$k(x) = \frac{\langle P(t = 0) \rangle}{P(x, 0)} \quad (E.11)$$

C. The MFC Method – Constant Slope

The expression for photosynthetic rate is given as the change in the molar concentration of carbon dioxide at a given area in the leaf.

$$P_S = \frac{dn_{CO_2}}{dt} * \frac{1}{A_{leaf}} \quad (E.12)$$

Where,

$$\frac{dn_{CO_2}}{dt} = \frac{d}{dt} [n_{air}] * c \quad (E.13)$$

If the rate of change of CO_2 in the labeling loop is constant, then the gas flow rate through the MFC is directly proportional to the CO_2 depletion rate, therefore the photosynthetic rate can be determined using the MFC flow rate. Where c is the ratio of carbon dioxide in the gas cylinder used for injection.

$$P_S = \frac{c}{A_{leaf}} * \frac{d}{dt} \left[\frac{P * V(t)}{RT} \right] \quad (E.14)$$

The MFC injects CO₂ mixed with air and has units of cubic centimeter per minute (cc/min).

$$P_S = \frac{c * P}{A_{leaf} RT} * [MFC(t)] \quad (E.15)$$

D. The MFC Method – Non Constant Slope

If rate of change of CO₂ in the labeling loop is not constant, photosynthetic rate calculations should account for the loss of CO₂ from the labeling loop and also the injection from the MFC as presented in the following equations.

$$P_S = \left[\frac{dn_{CO_2}^{MFC}}{dt} + \frac{dn_{CO_2}^{loop}}{dt} * V_{loop} \right] * \frac{1}{A_{leaf}} \quad (E.16)$$

The photosynthetic rate in this case would be a combination of equations E.10 and E.16.

$$P_S = \frac{c * P}{A_{leaf} RT} * [MFC(t)] + \frac{\langle P_{loop} \rangle}{\langle RT \rangle} * \left| \frac{d[IRGA]}{dt} \right| * \frac{V_{loop}}{A_{leaf}} \quad (E.17)$$

E. ¹¹C Pulse Loading Method

An alternative method of determining the photosynthetic rate involves monitoring radioactivity concentration in the circulation loop. The ratio of carbon-11 tagged CO₂ to carrier free CO₂ can assist in determining the loss of gas due to plant absorption.

$$PS = [J(t) * \frac{n_{CO_2}^{loop}}{n_{CO_2}}] \quad (E.18)$$

The variable $J(t)$ represents the diffusion of gas molecules through the plant membrane over a given area per time. One can solve for $J(t)$ by using the equation that predicts that the decrease in number of ¹¹C molecules is due to diffusion led absorption in the leaf and also radioactive decay.

$$\frac{dN_{11}(t)}{dt} = -\lambda N - J(t)A \quad (E.19)$$

$$J(t)A = -\lambda N - \frac{dN_{11}(t)}{dt} \quad (E.20)$$

Rearranging equation E.20 yields the expression for $J(t)$, which is directly proportional to the photosynthetic rate.

One can determine the change in the number of carbon-11 molecules by multiplying Avogadro's number by the molar concentration of ¹¹C in the labeling loop.

$$N_{11} = n_{11} * N_A \quad (E.21)$$

Determining the molar concentration of ^{11}C in the labeling loop is not as straight forward. Since it is not feasible to have detectors to measure the entire labeling loop, a reference point in line with circulation is usually chosen to sample the radioactivity circulating in the loop. We call this activity the Line Detector (L_R) rate as a function of time.

$$n_{11} = \frac{L_R(t)}{\lambda N_A} * \left(\frac{V_{Loop}}{V_{sample}} \right) * \frac{4\pi}{d\Omega\epsilon} \quad (\text{E.22})$$

Once the effective solid angle and efficiency of the line detector are accounted for in the measurement, we can scale the sample volume to the total volume of the labeling loop. Now we can find the next variable in equation E.19, the number of moles of CO_2 .

$$N_{CO_2} = c * n_{air} \quad (\text{E.23})$$

This value has already been shown to be the following as expressed in E.7.

$$n_{CO_2} = [\text{IRGA}] * \left(\frac{P_{Loop} V_{Loop}}{RT_{Loop}} \right) \quad (\text{restated E.7})$$

Combining E.7 and E.23 gives us the following expression:

$$\text{PR} = - \left(\frac{\lambda N_A}{A_{exposed}} * \frac{P_{Loop} V_{Loop}}{RT_{Loop}} \right) [\text{IRGA}] * \left[1 + \left(\frac{1}{\lambda L_R(t)} \right) \left(\frac{dL_R(t)}{dt} \right) \right] \quad (\text{E.24})$$

This method is recommended for relative photosynthetic rate measurements for comparing photosynthetic rates of different experimental runs.

$$\frac{PR_2}{PR_1} = - \left(\frac{\lambda N_A}{A_e} * \frac{P_2 T_1}{P_1 T_2} \right) \left[\frac{IRGA_2}{IRGA_1} \right] * \left[\frac{1 + \left(\frac{1}{\lambda L_{R2}(t)} \right) \left(\frac{dL_{R2}(t)}{dt} \right)}{1 + \left(\frac{1}{\lambda L_{R1}(t)} \right) \left(\frac{dL_{R1}(t)}{dt} \right)} \right] \quad (E.25)$$

Appendix F: Geant4 Simulation Procedures

A. PET Reconstruction

cd to source file in Linux environment:

```
$cd [project space]/pet_planar
```

Edit geometry in src directory

```
$gedit [detector file name]
```

Edit particle source variables

```
$gedit [macro filename, e.g., vis.mac]
```

Type in next line when ready to run

```
$make
```

```
./bin/Linux++/GdMain [macro filename] > [output text file]
```

To begin PET Analysis

```
$source filter2.awk
```

```
$python positron4.py
```

```
$source sort4.awk
```

Output files: pair1.txt, pair2.txt, p1_number, p2_number

Transfer output files to MATLAB and execute: Position_code.m

Matlab command prompt: save geant4sim

Copy geant4sim MATLAB output to recon folder and run PPS executable

B. Silicon Strip Positron Imaging

cd to source file in Linux environment:

```
$cd [project space]/spades2.0
```

Edit geometry in src directory

```
$gedit [detector file name]
```

Edit particle source variables

```
$gedit [macro filename, e.g., vis.mac]
```

Type in next line when ready to run

```
$make
```

```
./bin/Linux++/GdMain [macro filename] > [output text file]
```

To select relevant detector parameters:

```
$source filter.awk
```

```
$python positron.py
```

```
$source sort.awk
```

Output files: initial.txt, lyso.txt, silicon.txt

Transfer output files to MATLAB and execute: Bestcode.m

Matlab command prompt: save geant4sim

Copy geant4sim MATLAB output to recon folder and run PPS

Bibliography

- [Agb10] N.N. Agbeko, J. Cheng, A. Zakhnini, R. Laforest, and J.A. O'Sullivan. *Positron Range Correction in PET Using an Alternating EM Algorithm*. IEEE, (2010) 2875-2878.
- [Ago03] S. Agostinelli *et al.* *Geant4-A Simulation Toolkit*. Nuclear Instruments and Methods in Physics Research A., **506**(2003) 250-303.
- [Ale06] A. Alessio and P. Kinahan. *PET Image Reconstruction*. In: R.E. Henkin *et al.*, (Ed.) *Nuclear Medicine*, 2nd ed., Philadelphia, Elsevier (2006).
- [Ale11] D.L. Alexoff, S.L. Dewey, P. Vaska, S. Krishnamoorthy, R. Ferrieri, M. Schueller, D.J. Schlyer, and J.S. Fowler. *PET Imaging of Thin Objects: Measuring the Effects of Positron Range and Partial-Volume Averaging in the Leaf of *Nicotiana tabacum**. Nucl. Med. And Biol., **38**(2011) 191-200.
- [And91] P. Andreo *et al.* *Monte Carlo Techniques in Medical Radiation Physics*. Physics in Medicine and Biology, **36**(7) 861-920.
- [Aur10] G. Di Domenico *et al.* *An Ultra-High Resolution Design of a Small Animal PET Scanner Based on Stacks of Double-Sided Silicon Strip Detector*. Nuclear Instruments and Methods A., **571**(2007) 22-25.
- [Ayd05] A. Aydin. *Monte Carlo Calculations of Low Energy Positrons in Silicon*. Nukleonika. **50**(2005) 37-42.
- [Bai06] H.P. Bais, T.L. Weir, L.G. Perry, S. Gilroy, and J.M. Vivanco. *The Role of Root Exudates in Rhizosphere Interactions with Plants and Other Organisms*. **57**(2006) 233-266.
- [Bai13] M. Bai, C.R. Howell, A.S. Crowell, L.C. Cumberbatch, B.A. Fallin, C.D. Reid, A.G. Weisenberger, B. Kross, S. Lee, J. McKisson, J.E. McKisson. *Simulation of Sugars Allocation and Translocation in Grasses*. TUNL Progress Report, (2013) 110-111.
- [Ban02] P. Bancal and F. Soltani. *Source-Sink Partitioning. Do We Need Munch*. Journal of Experimental Botany, **53**(2002) 1919-1928.
- [Bar09] P. Barbeau. *Neutrino and Astroparticle Physics with P-type Point Contact High Purity Germanium Detectors*. PhD Thesis, (2009) 4-53.

- [Bat95] G. Batignani, L. Bosisio, E. Focardi, F. Forti, M. Giorgi, D. Marangoni, G. Rizzo, G. Tonelli, and G. Triggiani. *Double-Sided Silicon Strip Detectors in Pisa*. Nuclear Instruments and Methods in Physics Research, **360**(1995) 98-102.
- [Bel83] E. Belau, R. Klanner, G. Lutz, E. Neugebauer, H.J. Seebrunner and A. Wylie. *Charge Collection in Silicon Strip Detectors*. Nuclear Instruments and Methods, **214**(1983) 253-260.
- [Ber99] M.J. Berger, J.S. Coursey, and M.A. Zucker. ESTAR, PSTAR, and ASTAR: Computer Programs for Calculating Stopping-Power and Range Tables for Electrons, Protons, and Helium Ions (version 1.21), NIST (1999). URL:<http://physics.nist.gov/STAR>.
- [Ber12] R.L. Berendsen, C.M.J. Pieterse, and P.A.H.M. Bakker. *The Rhizosphere Microbiome and Plant Health*. Trends in Plant Science, **17**(2012) 478-486.
- [Bev92] P.R. Bevington and D.K. Robinson. *Data Reduction and Error Analysis for the Physical Sciences*. WCB/McGraw-Hill Boston, MA, 1992.
- [Bou16] Boundless (2016). Retrieved from <https://www.boundless.com>. *Boundless Biology*.
- [Bra14] D.M. Braun, L. Wang, and Y.L. Ruan. *Understanding and Manipulating Sucrose Phloem Loading, Unloading, Metabolism, and Signalling to Enhance Crop Yield and Food Security*, **65**(2014) 1713-1735.
- [Buc00] B.B. Buchanan, W. Gruissem, and R.L. Jones. Biochemistry and Molecular Biology of Plants, American Society of Plant Physiologists, Rockville, MD.
- [Cal09] J. Cal-Gonzalez, J.L. Herraiz, S. Espana, M. Desco, J.J. Vaquero, and J.M. Udias. *Positron Range Effects in High Resolution 3D PET Imaging*. IEEE, (2009) 2788-2791.
- [Can] Canberra. <http://www.canberra.com>. Canberra Industries.
- [Cha77] R. Chawla and S.L. Bhattacharya. *Determination of Absolute Tool Wear by Y-Y Coincidence Counting of Radiotracers*. WEAR, **43**(1977) 175-183.
- [Che03] S.R. Cherry, J.A. Sorenson, and M.E. Phelps. *Physics in Nuclear Medicine*. 3rd Edition, Saunders, (2003) Chapter 3.
- [Cho75] Z.H. Cho, J.K. Chan, L. Ericksson, M. Singh, S. Graham, N.S. MacDonald, and Y. Yano. *Positron Ranges from Biomedically Important Positron-emitting Radionuclides*. J. Nucl. Med., **16**(1975) 1174-1176.

- [Cle78] M.D. Clegg, C.Y. Sullivan, and J.D. Eastin. *A Sensitive Technique for the Rapid Measurement of Carbon Dioxide Concentrations*, **62**(1978) 924-926.
- [Cli12] N. Clinthorne et al. *A High-Resolution PET Demonstrator Using a Silicon "Magnifying" Glass*. *Physics Procedia*, **37**(2012) 1488-1496.
- [Cur12] J.D. Cure and B. Acock. *Crop Responses to Carbon Dioxide Doubling: A Literature Survey*. *Agricultural and Forest Meteorology*, **38**(1986) 127-145.
- [Dak02] F.D. Dakora and D.A. Phillips. *Root Exudates as Mediators of Mineral Acquisition in Low-nutrient Environments*. *Plant and Soil*, **245**(2002) 35-47.
- [Dap06] M. Dapor. *A Comparative Study of Electron and Positron Penetration in Silicon Dioxide*. *Journal of Electron Spectroscopy and Related Phenomena*, **151**(2006) 182-192.
- [Dau10] C. Masclaux-Daubresse, F. Daniel-Vedele, J. Dechorgnat, F. Chardon, L. Gaufichon and A. Suzuki. *Nitrogen Uptake, Assimilation and Remobilization in Plants: Challenges for Sustainable and Productive Agriculture*. *Annals of Botany*, **105**(2010) 1141-1157.
- [Dij13] F.A. Dijkstra, Y. Carillo, E. Pendall, and J.A. Morgan. *Rhizosphere Priming: A Nutrient Perspective*. *Frontiers in Microbiology*, **4**(2013) Article 216.
- [Din12] S. Dinant and P. Suarez. *Multitude of Long-Distance Signal Molecules Acting Via Phloem*. *Biocommunication of Plants*, Springer. Berlin (2012) Chapter 14.
- [Dir12] R.C. Dirks, M. Singh, G.S. Potter, L.G. Sobotka, and J. Schaefer. *Carbon Partitioning in Soybean (*Glycine max*) leaves combines ¹¹C and ¹³C Labeling*. *New Phytologist*, **196**(2012) 1109-1121.
- [Dra11] J.E. Drake et al. *Increases in the Flux of Carbon Belowground Stimulate Nitrogen Uptake and Sustain Long-term Enhancement of Forest Productivity Under Elevated CO₂*. *Ecology Letters*, **14**(2011) 349-357.
- [Dub96] T. Dubbs, S. Kashigin, M. Kratzer, W. Kroeger, T. Pulliam, H.F. Sadrozinski, M. Schwab, E. Spencer, R. Wichmann, M. Wilder, Y. Unno and T. Ohsugi. *Efficiency and Noise Measurements of Non-Uniformly Irradiated Double-Sided Silicon Strip Detectors*. *Nuclear Instruments and Methods in Physics Research A.*, **383**(1996) 174-178.
- [Eas13] H.M. Easlon and A.J. Bloom. *The Effects of Rising Atmospheric Carbon Dioxide on Shoot-Root Nitrogen and Water Signaling*. *Frontiers in Plant Sciences* , **4**(2013) Article 304.

- [Eco] EcoFlex® Gel.
http://www.sdplastics.com/norplexmicarta_property_comparison.html.
- [Eid04] S. Eidelmann *et.al.* Passage of Particles through Matter. In Phys. Lett. B, **592**(2004), Chapter 27. Particle Data Group, 2004.
- [For02] B.G. Forde. *Local and Long-Range Signaling Pathways Regulating Plant Responses to Nitrate*. Annu. Rev. Plant Biol., **53**(2003) 203-224.
- [Fre04] C. Freeman, S.Y. Kim, S.H. Lee, and H. Kang. *Effects of Elevated CO₂ Concentrations on Soil Microorganisms*. The Journal of Microbiology, **42**(2004) 267-277.
- [Fuk05] Y. Fukazawa, T. Nakamoto, N. Sawamoto, S. Uno, T. Ohsugi, H. Tajima, T. Takahashi, T. Mitani, T. Tanaka, and K. Nakazawa. *Low-Noise Double-Sided Silicon Strip Detector for Soft Gamma-Ray Compton Camera*. Submitted to High Energy Detectors in Astronomy, (2005).
- [Gia13] G. Giacomini, L. Bosisio, and I. Rashevskaya. *Measurement of Johnson Noise Induced by p-Stops in Silicon Microstrip Detectors*. IEEE, **60**(2013) 4022-4025.
- [Ger01] G. De Geronimo, P. O'Connor, V. Radeka, and B. Yu. *Front-End Electronics for Imaging Detectors*. Nuclear Instruments and Methods in Physics Research A, **471**(2001) 192-199.
- [Gif85] R.M. Gifford, H. Lambers, and J.I.L. Morison. *Respiration of Crop Species Under CO₂ Enrichment*. Physiologica Plantarum, **63**(1985) 351-356.
- [Gol68] V.I. Goldanski. *Physical Chemistry of the Positron and Positronium*. Atomic Energy Review, **6**(1968) 3-148.
- [Gou12] N. Gould, M.R. Thorpe, J. Pritchard, J.T. Christeller, L.E. Williams, G. Roeb, U. Schurr, and P.E.H. Minchin. *AtSUC2 has a Role for Sucrose Retrieval along the Phloem Pathway: Evidence from Carbon-11 Tracer Studies*. Plant Science, **188-189**(2012) 97-101.
- [Gps] General Particle Source.
<https://geant4.web.cern.ch/geant4/UserDocumentation/UsersGuides/ForApplicationDeveloper/html/ch02s07.html>. 2008
- [Hab90] S.F. Haber, S.E. Derenzo, and D. Uber. *Application of Mathematical Removal of Positron Range Blurring in Positron Emission Tomography*. IEEE, **37**(1990) 1293-1299.
- [Ham03] Hamamatsu Photonics. Hamamatsu H8500 PSPMT Technical Specifications

Sheet, June 2003.

- [Han14] J.L. Han, J.B. Ma, X.G. Cao, Q. Wang, J.S. Wang, Y.Y. Yang, M. Peng, M.R. Huang, S.L. Jin, X.J. Rong, Z. Bai, F. Fu, Q. Hu, R.F. Chen, S.W. Xu, J.B. Chen, L. Jin, Y. Li, M.H. Zhao, and H.S. Xu. *Performance of a Double Sided Silicon Strip Detector as a Transmission Detector for Heavy Ions*. Chinese Physics C, **38**(2014) 056202(1)-056202(7).
- [Har14] S. Harzmann, F. Braun, A. Zakhnini, W.A. Weber, and U. Pietrzyk. *Implementation of Cascade Gamma and Positron Range Corrections for I-124 Small Animal PET*. IEEE, **61**(2014) 142-153.
- [Hei15] M.G.A. van der Heijden, F.M. Martin, M.A. Selosse, and I.R. Sanders. *Mycorrhizal Ecology and Evolution: the Past, the Present, and the Future*. New Phytologist, **205**(2015) 1406-1423.
- [Hen86] D.L. Hendrix and S.C. Huber. *Diurnal Fluctuations in Cotton Leaf Carbon Export, Carbohydrate Content, and Sucrose Synthesizing Enzymes*. Plant Physiol., **81**(1986) 584-586.
- [Her05] J.L. Herraiz, S. Espana, J.M. Udias, J.J. Vaquero, M. Desco. *Statistical Reconstruction Methods in PET: Resolution Limit, Noise Artifacts and Considerations for the Design of Better Scanners*. IEEE, (2005) 1846-1850.
- [Hoa50] D.R. Hoagland and D.I. Arnon. *The Water-Culture Method for Growing Plants without Soil*. Circular, California Agricultural Experiment Station, **347** (1950) 32.
- [Hod96] A. Hodge, S.J. Grayston, and B.G. Ord. *A Novel Method for Characterization and Quantification of Plant Root Exudates*. Plant and Soil, **184**(1996) 97-104.
- [Hof69] G. Hofstra and C.D. Nelson. *The Translocation of Photosynthetically Assimilated ¹⁴C in Corn*. Can. J. Bot., **47**(1969) 1435-1442.
- [Hor58] L. Horwit. *Some Simplified Mathematical Treatments of Translocation in Plants*. Plant Physiology, **33**(1958) 81-93.
- [Huh07] S. Huh, W.L. Rogers, and N.H. Clinthorne. *An Investigation of an Intra Operative PET Imaging Probe*. IEEE, (2007) 552-555.
- [Hun03] S. Hunt. *Measurements of Photosynthesis and Respiration in Plants*. Physiologia Plantarum, **117**(2003) 314-325.
- [IAE14] IAEA Report. *Quantitative Nuclear Medicine Imaging: Concepts, Requirements and Methods*. International Atomic Energy Agency, (2014).

- [Jon98] D.L. Jones. *Organic Acids in the Rhizosphere – A Critical Review*. Plant and Soil, **205**(1998) 25-44.
- [Jon04] D.L. Jones, A. Hodge, and Y. Kuzyakov. *Plant and Mycorrhizal Regulation of Rhizodeposition*. New Phytologist, **163**(2004) 459-480.
- [Kat52] L. Katz and A.S. Penfold. *Range-energy Relations for Electrons and The Determination of Beta-ray End-Point Energies by Absorption*. Rev. Mod. Phys., **24**(1952) 28-44.
- [Ker85] P.S. Kerr, T.W. Rufty, and S.C. Huber. *Endogenous Rhythms in Photosynthesis, Sucrose Phosphate Synthase Activity, and Stomatal Resistance Leaves of Soybean (*Glycine max* [L.] Merr.)*. Plant Physiol., **77**(1985) 275-280.
- [Keu02] N. Keutgen *et al.* *Transfer Function Analysis of Positron-Emitting Tracer Imaging System (PETIS) data*. Applied Radiation and Isotopes, **57**(2002) 225-233.
- [Kis08] M.R. Kiser, *Development of a System for Real-time Measurements of Metabolite Transport in Plants Using Short-lived Positron-emitting Radiotracers*, Doctoral Dissertation, Duke University, 2008.
- [Kno89] G.F. Knoll. *Radiation Detection and Measurement, 4th Edition*, John Wiley and Sons, New York. (1989) Chapter 11.
- [Koi09] T. Koizumi and Y. Chihara. *Absolute Detection Efficiencies of an Ion-Counting System with a Channel-Electron Multiplier*. Journal of Physics, **163**(2009) 112-114.
- [Kra01] M. Krammer. *Silicon Detectors*. XI ICFA School on Instrumentation. (2001) <http://fisica.cab.cnea.gov.ar/particulas/html/icfa/wiki/images/a/a9/Krammer01.pdf>.
- [Kuh10] C. Kuhn and C.P. Grof. *Sucrose Transporters of Higher Plants*. Current Opinion in Plant Biology, **13**(2010) 288-298.
- [Kuz13] Y. Kuzyakov and X. Xu. *Competition between Roots and Microorganisms for Nitrogen: Mechanisms and Ecological Relevance*. New Phytologist, **198**(2013) 656-669.
- [Kwi94] P.G. Kwiat, A.M. Steinberg, R.Y. Chiao, P.H. Eberhard, and M.D. Petroff. *Absolute Efficiency and Time-Response of Single-Photon Detectors*. Applied Optics, **33**(1994) 1844-1853.

- [Lac00] A. Lacointe. *Carbon Allocation Among Tree Organs: A Review of Basic Processes and Representation in Functional-structural Tree Models*. Ann. Plant, Cell and Environment, **26**(2003) 37-56.
- [Lal03] S. Lalonde, M. Tegeder, M. Throne-Holst, W.B. Frommer, and J.W. Patrick. *Phloem Loading and Unloading of Sugars and Amino Acids*. Ann. For. Sci., **57**(2000) 521-533.
- [Lan84] K. Lange and R. Carson. *EM Reconstruction Algorithms for Emission and Transmission Tomography*. J. Comput. Assist. Tomogr., **8**(1984) 306-316.
- [Lea00] R.M. Leahy and J. Qi. *Statistical Approaches in Quantitative Positron Emission Tomography*. Statistics and Computing, **10**(2000) 147-165.
- [Lee10] J.M. Lee, P. Sathish, D.J. Donaghy, and J.R. Roche. *Plants Modify Biological Processes to Ensure Survival following Carbon Depletion: A Lolium perenne Model*. PloS One, **5**(8) (2010) e12306.
- [Leh11] W. Lehnert, M. Gregoire, A. Reilhac, and S.R. Meikle. *Analytical Positron Range Modelling in Heterogeneous Media for PET Monte Carlo Simulations*. Phys. Med. Biol., **56**(2011) 3313-3335.
- [Lem13] R. Lemoine *et al.* *Source-to-Sink Transport of Sugar and Regulation by Environmental Factors*. Frontiers in Plant Science, **4**(2013) 1-9.
- [Leo94] W.R. Leo. *Techniques for Nuclear and Particle Physics Experiments*, Chapter 10. 1994.
- [Lev99] C.S. Levin and E.J. Hoffman. *Calculation of Positron Range and its Effect on the Fundamental Limit of Positron Emission Tomography System Spatial Resolution*. Phys. Med. Biol., **44**(1999) 781-799.
- [Li96] LI-COR, Inc. *LI-6262 CO₂/H₂O Analyzer Instruction Manual*, March 1996.
- [Lil83] D. Liljequist. *A Simple Calculation of Inelastic Mean Free Path and Stopping Power for 50 eV-50 keV Electrons in Solids*. J. Phys. D: Appl. Phys., **16**(1983) 1567-1582.
- [Lon04] S.P. Lon, E.A. Ainsworth, A. Rogers, and D.R. Ort. *Rising Atmospheric Carbon Dioxide: Plants FACE the Future*. Annual Review of Plant Biology, **55**(2004) 591-628.
- [Mad13] M. Madhu and J.L. Hatfield. *Dynamics of Plant Root Growth under Increased Atmospheric Carbon Dioxide*. Agronomy Journal, **105**(2013) 657-669.

- [Mat05] S. Matsuhashi, S. Fujimaki, N. Kawachi, K. Sakamoto, N.S. Ishioka, and T. Kume. *Quantitative Modeling of Photoassimilate Flow in a Intact Plant using the Positron Emitting Tracer Imaging System (PETIS)*. *Soil Sci. Nutr.*, **51**(2005) 417-423.
- [McN83] G.S. McNaughton and M.R. Presland. *Whole Plant Studies using Radioactive ¹³-Nitrogen: I. Journal of Experimental Botany*, **34**(1983) 880-892.
- [Mel00] C.L. Melcher. *Scintillation Crystals for PET*. *Journal of Nuclear Medicine*, **41**(2000) 1051-1055.
- [Min78] P.E.H. Minchin. *Analysis of Tracer Profiles with Applications to Phloem Transport*. *Journal of Experimental Botany*, **29**(1978) 1441-1450.
- [Min80] P.E.H. Minchin and J.H. Troughton. *Quantitative Interpretation of Phloem Translocation Data*. *Annual Review of Plant Physiology*, **31**(1980) 191-215.
- [Min96] P.E.H. Minchin, M.J. Lees, M.R. Thorpe, and P.C. Young. *What Can Tracer Profiles Tell Us About the Mechanisms Giving Rise to Them?* *Journal of Experimental Botany*, **47**(1996) 275-284.
- [Min03] P.E.H. Minchin and M.R. Thorpe. *Using the Short-lived ¹¹C in Mechanistic Studies of Photosynthates Transport*. *Functional Plant Biology*, **30**(2003) 831-841.
- [Mon05] L.M. Montano. *Laboratory Course on Silicon Strip Detectors*. *Journal of Physics*, **18**(2005) 368-379.
- [Ber12] L. Musilova, J. Ridl, M. Polivkova, T. Macek and O. Uhlik. *Effects of Secondary Plant Metabolites on Microbial Populations: Changes in Community Structure and Metabolic Activity in Contaminated Environments*. *Int. J. Mol. Sci.*, **17**(2016) 1205.
- [Nea68] T.F. Neales and L.D. Incoll. *The Control of Leaf Photosynthesis Rate By The Level of Assimilate Concentration In The Leaf: A Review of the Hypothesis*. *The Botanical Review*, (2015) 107-125.
- [NOAA] National Oceanic & Atmospheric Administration.
URL: <https://esrl.noaa.gov/gmd/ccgg/trends/gr.html>
- [Pal04] M. R. Palmer and J.A. Parker. *High Resolution Imaging with Positron Emitters: Modeling Range Blurring Effects*. *IEEE* (2004) 2682-2685.
- [Pan04] R. Pani et al. *New Devices for Imaging in Nuclear Medicine*. *Cancer Biotherapy and Radiopharmaceuticals*, **19**(2004) 121-128.

- [Par06] H. Park, H.J. Hyun, D.H. Kah, H.D. Kang, H.J. Kim, Y.I. Kim, Y.J. Kim, and D.H. Shim. *Design and Fabrication of the Double-Sided Silicon Microstrip Sensor*. Journal of the Korean Physical Society, **49**(2006) 1401-1406.
- [Pid03] L. Pidol, A. Khan-Harari, B. Viana, B. Ferrand, P. Dorenbos, J.T.M. de Haas, C.W.E. van Eijk, and E. Virey. *Scintillation Properties of $\text{Lu}_2\text{Si}_2\text{O}_7:\text{Ce}^{3+}$, a Fast and Efficient Scintillator Crystal*. J. Phys.: Condens. Matter. **15**(2003) 2091-2102.
- [Pri00] S.G. Pritchard and H.H. Rogers. *Spatial and Temporal Deployment of Crop Roots in CO_2 -enriched Environments*. **147**(2000) 55-71.
- [Qi06] J. Qi and R.M. Leahy. *Iterative Reconstruction Techniques in Emission Computed Tomography*. Phys. Med. Biol., **51**(2006) R541-R578.
- [Ran16] H. Ranjbar, J. Wien, A.J. Mathews, S. Komarov, Q. Wang, K. Li, J.A. O'Sullivan, and Y.C. Tai. *A Simultaneous Beta and Coincidence-Gamma Imaging System for Plant Leaves*. Phys. Med. Biol., (2016) 3572-3595
- [Rea02] A.J. Reader, S. Ally, F. Bakatselos, R. Manavaki, G. Trigui, R. Walledge, A. P. Jeavons, P.J. Julyan, S. Zhao, D.L. Hastings, and J. Zweit. *Regularized One-Pass List-Mode EM Algorithm for High Resolution 3D PET Image Reconstruction into Large Arrays*. IEEE, (2002) 1853-1858
- [Reg10] N. Regier, S. Streb, S.C. Zeeman, and B. Frey. *Seasonal Changes in Starch and Sugar Content of Polar (*Populus deltoids x nigra* cv. Dorskamp) and the Impact of Stem Girdling on Carbohydrate Allocation to Roots*. Tree Physiology, **30**(2010) 979-987.
- [Rei94] C.D. Reid and B.R. Strain. *Effects of CO_2 Enrichment on Whole Plant Carbon Budget of Seedlings of *Fagus grandifolia* and *Acer saccharum* in Low Irradiance*. Oecologia, **98**(1994) 31-39.
- [Riv14] A. Rivetti. *Fast Front-End Electronics for Semiconductor Tracking Detectors: Trends and Perspectives*. Nuclear Instruments and Methods in Physics Research A., **765**(2014) 202-208.
- [Rob07] A.B. Robinson, N.E. Robinson, and W. Soon. *Environmental Effects of Increased Atmospheric Carbon Dioxide*. Journal of American Physicians and Surgeons, **12**(2007) 79-90.
- [Roh54] F. Rohrlich and B.C. Carlson. *Positron-electron Differences in Energy Loss and Multiple Scattering*. Phys. Rev., **93**(1954) 38-44.
- [Roh04] E.M. Rohren, T.G. Turkington, and R.E. Coleman. *Clinical Applications of PET in Oncology*. Radiology, **231**(2004) 305-332.

- [Rou15] D. Rousseau, Y. Chene, E. Belin, G. Semaan, G. Trigui, K. Boudehri, F. Franconi, and F. Chapeau-Blondeau. *Multiscale Imaging of Plants: Current Approaches and Challenges*. *Plant Methods*, **51**(2006) 11:6
- [Rub39] S. Ruben, W.Z. Hassid, and M.D. Kamen. *Radioactive Carbon in the Study of Photosynthesis*. *Journal of the American Chemical Society*, **61**(1939) 661-663.
- [Sai04] Saint-Gobain Crystals. PreLude®420 Scintillation Material Data Sheet. Accessible online at www.detectors.saint-gobain.com, (2004).
- [San11] S.P. Sane and A.K. Singh. *Water Movement in Vascular Plants: A Primer*. *Journal of the Indian Institute of Science* 91(3), (2011) 233-242.
- [Sar04] O. Sarrhini, M. Bentourkia. *Effect of Detector Scatter Restoration on Image Spatial Resolution and Partial Volume*. *IEEE*, (2004) 1385-1387
- [Sch06] U. Schurr, A. Walter, and U. Rascher. *Functional Dynamics of Plant Growth and Photosynthesis – from Steady-State to Dynamics – from Homogeneity to Heterogeneity*. *Plant, Cell and Environment*, **29**(2006) 340-352.
- [Seo11] H. Seo, J.H. Park, C.H. Kim, J.H. Lee, C.S. Lee, and J.S. Lee. *Compton-Edge-Based Energy Calibration of Double-Sided Silicon Strip Detectors in Compton Camera*. *Nuclear Instruments and Methods in Physics Research A.*, **633**(2011) S108-S110.
- [She82] L.A. Shepp, Y. Vardi. *Maximum Likelihood Reconstruction for Emission Tomography*. *IEEE*, (1982) 113-122.
- [Sie55] K. Siegbah. *Beta- and Gamma-ray Spectroscopy*. (New York: Interscience) Chapter 1.
- [Sle10] T.L. Slewinski and D.M. Braun. *Current Perspectives on the Regulation of Whole-Plant Carbohydrate Partitioning*. *Plant Science*, **178**(2010) 341-349.
- [Smi07] A.M. Smith and M. Stitt. *Coordination of Carbon Supply and Plant Growth*. *Plant, Cell, and Environment*. **30**(2007) 1126-1149.
- [Son08] D.H. Son, Y.I. Kim, H. Kang, H.J. Kim, H.O. Kim, H. Park, and S. Ryu. *Signal-to-Noise Ratio Measurement of a Double-Sided Silicon Strip Detector by using 45-MeV Proton Beam*. *Journal of Korean Physical Society*, **52**(2008) 949-953.
- [Spi99] H. Spieler. *Introduction to Radiation Detectors and Electronics*. Energy Deposition in the Detector and Spectrum Formation (1999).

- [Sto09] A.V. Stolin, A.G. Weisenberger, J.E. McKisson, and S. Majewski. *Feasibility Study of Using Detection of Direct Positrons in Plant Imaging Research*. IEEE, (2009) 2338-2341.
- [Tai02] L. Taiz and E. Zeiger. *Plant Physiology*, Sinauer Associate Inc., Sunderland, Mass., 3rd edition, 2002.
- [Tam81] K.C. Tam and V. Perez-Mendez. *Tomographical Imaging with Limited-Angle Input*. J. Opt. Soc. Am., **71**(1981) 582-592.
- [Tan08] P. Tans. *Trends in Atmospheric Carbon Dioxide – Mauna Loa*. NOAA/ESRL (www.esrl.noaa.gov/gmd/ccgg/trends/), 2008.
- [Tho91] M.R. Thorpe and P.E.H. Minchin. *Continuous Monitoring of Fluxes of Photoassimilate in Leaves and Whole Plants*. J. Exp. Botany, **42**(1991) 461-468.
- [Tho06] M.V. Thompson. *Phloem: the Long and the Short of It*. Trends in Plant Science, **11**(2006) 26–32.
- [Tho07] M.R. Thorpe, A.P. Ferrieri, M.M. Herth and R.A. Ferrieri. *¹¹C-imaging: Methyl Jasmonate moves in both Phloem and Xylem, Promotes Transport of Jasmonate, and of Photoassimilate even after Proton Transport is Decoupled*. Planta, **226**(2007) 541– 551.
- [Ton10] S. Tong, A.M. Alessio, and P.E. Kinahan. *Noise and Signal Properties in PSF-based fully 3D PET Image Reconstruction: An Experimental Evaluation*. Phys. Med. Biol., **55**(2010) 1453–1473.
- [Top13] A. Topkar, A. Singh, and B. Aggarwal, Am. Kumar, Ar. Kumar, C.K. Pithawa. *Development of Double-Sided Silicon Strip Detector*. Proceedings of the DAE Symp. on Nucl. Phys. **58**(2013) 856–857.
- [Tow80] D. Townsend, B. Schorr, A. Jeavons. *3-Dimensional Image Reconstruction for a Positron Camera with Limited Angular Acceptance*. IEEE Trans. Nucl. Sci., **27**(1980) 463–470.
- [Tro95] C. Troncon. *Measurement of Spatial Resolution and Charge Collection in Double-Sided Double Metal Silicon Microstrip Detectors*. Nuclear Physics B, **44** (1995) 287-291.
- [Tyr74] M.T. Tyree, A.L. Christy, and J.M. Ferrier. *A Simpler Iterative Steady State Solution of Munch Pressure-Flow Systems Applied to Long and Short Translocation Paths*. Plant Physiol., **54**(1974) 589–600.

- [Van01] S. Vandenberghe, Y. D'Asseler, R. Van de Walle, T. Kauppinen, M. Koole, L. Bouwens, K. Van Laere, I. Lemahieu, and R.A. Dierckx. *Iterative Reconstruction Algorithms in Nuclear Medicine*. *Comp. Med. Imag. Graphics*. **25**(2001) 105–111.
- [Van07] S. Vandenberghe, I. Lemahieu. *System Characteristics of Simulated Limited Angle TOF PET*. *Nucl. Instr. Meth. A*. **571**(2007) 480–483.
- [Wan16] L. Wang and Y.L. Ruan. *Shoot-Root Carbon Allocation, Sugar Signalling and Their Coupling with Nitrogen Uptake and Assimilation*. *Functional Plant Biology*, **43**(2016) 105–113.
- [Wei11] A.G. Weisenberger, H. Dong, B. Kross, S. Lee, J. McKisson, J.E. McKisson, W. Xi, C. Zorn, C.R. Howell, A.S. Crowell, L. Cumberbatch, C.D. Reid, M.F. Smith and A. Stolin. *Development of PhytoPET: A Plant Imaging PET System*. *IEEE*, (2011) 275-278.
- [Wei12] A.G. Weisenberger, B. Kross, S. Lee, J. McKisson, J.E. McKisson, W. Xi, C. Zorn, C.D. Reid, C.R. Howell, A.S. Crowell, L. Cumberbatch, B. Fallin, A. Stolin, and M.F. Smith. *PhytoBeta Imager: A Positron Imager for Plant Biology*. *Phys. Med. Biol.*, **57**(2012) 4195-4210.
- [Wei13] S. Lee, B. Kross, J. McKisson, J.E. McKisson, A.G. Weisenberger, W. Xi, C. Zorn, G. Bonito, C.R. Howell, C.D. Reid, A.S. Crowell, L. Cumberbatch, C. Topp, A. and M.F. Smith. *Imaging Corn Plants with PhytoPET, A Modular PET System for Plant Biology*. *IEEE*, (2013).
- [Whi10] P.J. White and P.H. Brown. *Plant Nutrition for Sustainable Development and Global Health*. *Annals of Botany*, **105**(2010) 1073-1080.
- [Wu11] H. Wu and Y.C. Tai. *A Novel Phoswich Imaging Detector for Simultaneous Beta and Coincidence-gamma Imaging of Plant Leaves*. *Physics in Medicine and Biology*, **56**(2011) 5583-5598.
- [Wul04] E.A. Wulf, B.F. Philips, W.N. Johnson, J.D. Kurfess, and E.I. Novikova. *Thick Silicon Strip Detector Compton Imager*. *IEEE* (2004) 1699-1703.
- [Yam06] S. Yamamoto, K. Matsumoto, and M. Senda. *Development of a GSO positron/single-photon imaging detector*. *Phys. Med. Biol.*, **51**(2006) 457-469.
- [Yan05] Z. Yang and D.J. Midmore. *Modelling Plant Resource Allocation and Growth Partitioning in Response to Environmental Heterogeneity*. *Ecologica Modelling*, **181**(2005) 59-77.

- [Yan08] Y. Yan and L. Zeng. *Scatter and Blurring Compensation in Inhomogenous Media Using a Postprocessing Method*. International Journal of Biomedical Imaging, (2008).
- [Yoo13] M. Yoo, S.J. Han, and J.H. Wee. *Carbon Dioxide Capture Capacity of Sodium Hydroxide Aqueous Solution*. Journal of Environmental Management, **114**(2013) 512-519.
- [You91] P. Young and P. Minchin. *Environmetric Time-Series Analysis: Modelling Natural Systems from Experimental Time-Series Data*. Int. J. Biol. Macromol., **13**(1991) 190-201.
- [Zha07] J. Zhang, P.D. Olcott, and C.S. Levin. *A New Positioning Algorithm for Position-Sensitive Avalanche Photodiodes*. IEEE, **54**(2007) 433–437.

Biography

Laurie Cumberbatch was born in St. Vincent and the Grenadines on October 25, 1977 and grew up in Brooklyn, NY, where he was accepted into the specialized high school, Brooklyn Technical H.S. After graduation, Laurie attended Penn State University where he majored in accounting and received his Bachelors of Science (B.S.) degree on May 2000. Laurie joined the Navy shortly after graduation and enlisted as a Data Specialist (renamed to Fire Controlman) where he attained the E-5 rank prior to an honorable discharge. His tours of duty included a long-term deployment to the Mediterranean and Persian Gulf. Upon discharge, Laurie completed his B.S. in Physics at the North Carolina Central University (NCCU) on May 2009. While at NCCU, he grew an interest nuclear physics and its applications to biology after conducting research with Dr. Benjamin Crowe and Dr. Diane Markoff. In August 2009, he began the graduate program in medical physics with a concentration in the nuclear medicine track at Duke University. While at Duke University, he received the following awards: Society of Duke Fellowship award, an Excellence in Teaching Assistantship Award in 2011, and an Excellence in Teaching Assistantship Award in 2012. His research interests include the use of novel detector designs to aid in the imaging of thin plant structures. One of his proposed imaging devices could also be applied to human subjects for diagnosing conditions near the surface of the skin or outer tissue layer in surgical applications. The following is a list of his most recent publications:

(1) Monte-Carlo Simulation of ${}^3\text{H}(\gamma, pn)n$ and ${}^3\text{He}(\gamma, pp)n$ Experiments at Hiys, Z. Han *et al.* (including L. Cumberbatch). EPJ Web of Conferences, 113, 08009 (2016), DOI: 10.1051/epjconf/201611308009

(2) Design of an Experiment to Measure a_{nn} Using ${}^3\text{H}(\gamma, pn)n$ at Hiys, F.Q.L. Friesen *et al.* (including L. Cumberbatch). EPJ Web of Conferences, 113, 08007 (2016), DOI: 10.1051/epjconf/201611308007

(3) Neutron-Neutron Quasifree Scattering in ND Breakup at 10 MeV, R.C. Malone *et al.* (including L. Cumberbatch). EPJ Web of Conferences, 113, 04010 (2016), DOI: 10.1051/epjconf/201611304010

(4) *Imaging Corn Plants with PhytoPET, A Modular PET System for Plant Biology*, Lee, S., *et al.* (including L. Cumberbatch). Nuclear Science Symposium and Medical Imaging Conference (NSS/MIC), 2013 IEEE. Doi: 10.1109/NSSMIC.2013.6829796.

(5) *Cross-Section Measurements of ${}^2\text{H}(n, n p)n$ in Symmetric Star Configurations*. Couture, A., *et al.* (including L. Cumberbatch). Phys. Rev. C., **85**(2013) 054004.

(6) *PhytoBeta imager: A Positron Imager for Plant Biology*, AG Weisenberger, *et al.* (including L. Cumberbatch). Physics in Medicine and Biology, **57**(2012), pp. 4195-4210.

(7) *Development of PhytoPET: A Plant Imaging PET System*, AG Weisenberger, *et al.* (including L. Cumberbatch). IEEE Nuclear Science Symposium Conference Record (2012), pp. 275-278.

Laurie's body of work examines the effect of positron range on thin objects and possible methods of compensation. Recent ongoing scholarly projects extend to the area of machine learning for image classification, image recovery in cases with limited projection data, and anomaly detection. He is interested in developing new imaging techniques or finding ways to improve upon existing imaging methods in the realm of nuclear medicine.